Turun yliopisto
University of Turku

HALOGEN HECTORITES: SMECTITES DESIGNED TO LUMINESCE

Hellen Silva Santos

TURUN YLIOPISTON JULKAISUJA – ANNALES UNIVERSITATIS TURKUENSIS
Sarja – ser. AI osa – tom. 571 | Astronomica – Chemica – Physica – Mathematica | Turku 2017

Turun yliopisto
University of Turku

HALOGEN HECTORITES: SMECTITES DESIGNED TO LUMINESCE

Hellen Silva Santos

TURUN YLIOPISTON JULKAISUJA – ANNALES UNIVERSITATIS TURKUENSIS
Sarja - ser. A I osa - tom. 571 | Astronomica - Chemica - Physica - Mathematica | Turku 2017

University of Turku

Faculty of Mathematics and Natural Sciences
Department of Chemistry
Laboratory of Materials Chemistry and Chemical Analysis
Doctoral Programme in Physical and Chemical Sciences

Supervised by

Docent Mika Lastusaari
Department of Chemistry
University of Turku
FI-20014 Turku, Finland

Custos

Docent Mika Lastusaari
Department of Chemistry
University of Turku
FI-20014 Turku, Finland

Reviewed by

Professor Felix Fernandez-Alonso
Rutherford Appleton Laboratory
Harwell Science and Innovation Campus
Didcot, Oxfordshire OX11 0QX, UK

Professor Philippe Smet
LumiLab, Department of Solid State Sciences
Ghent University
B-900 Gent, Belgium

Opponent

Dr. Vladimir Pankratov
MAX IV Laboratory
Lund University
P.O. Box 118, SE-22100 Lund, Sweden

The originality of this thesis has been checked in accordance with the University of Turku quality assurance system using the Turnitin OriginalityCheck service.

ISBN 978-951-29-7069-8 (PRINT)
ISBN 978-951-29-7070-4 (PDF)
ISSN 0082-7002 (PRINT)
ISSN 2343-3175 (PDF)
Painosalama Oy - Turku, Finland 2017

To my sister, Helma S. Castro, and

To my love, Dimitar I. Valev.

Preface

How strange are the roads where the life, without asking permission, decided to take me... Four years ago I could not imagine that I would be crossing the Atlantic to do my doctoral studies in Turku, Finland, and here I am. These past three years were not only challenging due to the fact that I have migrated my research field from analytical chemistry to inorganic materials chemistry, they were also the most difficult years I have lived: full of unexpected hindrances which were only possible to me to overcome them because of the amazing support I have received from many great people. Thus, here writes a heart full of gratitude!

The research presented in the current thesis was realized in the University of Turku, Turku, Finland, financed by the Brazilian funding agency CNPq, with a "ciência sem fronteiras" scholarship, associated to the Academy of Finland – CNPQ Finland – Brazil project (#490242/2012-0). My special acknowledgement to Flávio Velame (general coordinator of international cooperation of CNPq), whose availability and kindness allowed to solve every problem related to the grant. I also acknowledge Professor Hermi F. Brito, coordinator of the project and his wife Professor Cláudia Felinto.

My deep and sincere acknowledgment to adj. Professor Mika Lastusaari, who I like to call, kindly, "Pomo"! I am really thankful for Pomo's patience, guidance and support. I guess Pomo never ever had a student with so big extra-work problems, and he have been amazingly supportive! Moreover, I would guess that he could barely understand my bad English when I first arrived here, full of an odd Brazilian accent and not really meaning. Thank you very much for the patience, for understanding me, for all knowledge I have acquired during these years, for all detailed explanations, for being a really fast and effective Pomo, and for everything I possible forgot to mention…

My sincere gratitude to Professor Jorma Hölsä for giving me the opportunity of having this doctoral position, and for the guidance among the working project. I also would like to thank Professor Lucas C.V. Rodrigues for all help with the elaboration of the project, for the collaboration during the research project, and for solving several problems related with my grant, even not being his duty to do it.

Many thanks to all collaborators of my research. My special acknowledgement to Dr. Tero Laihinen who have taught me how to operate almost all the equipment that we have in the facilities of the department, playing also an important role on the revision of my articles, and helping me with several ideas and advises during this research. I thank Ermei Mäkilä for conducting all nitrogen sorption measurements in the physics department of the University of Turku. I acknowledge Professor Dunieskys G. Larrudé and Dr. Eric C. Romani for recording the STEM images of the materials in the Pontifical Catholic University of Rio de Janeiro, Rio de Janeiro-RJ Brazil. I thank Dr. Pekka Laukkanen and Marjukka Tuominen for conducting the XPS measurements in the Physics department of the University of Turku. I acknowledge Dr. Antti Viinikanoja and adj. Professor Pia Damlin for all help with the FTIR measurements, and further revision of the articles. I thank adj. Professor Jari Sinkkonen and Isabella Norrbo for all help with the ^{29}Si MAS NMR measurements, and all help with the revision of the manuscripts we have collaborated. I also thank Dr. José M. Carvalho and Dr. Liana Nakamura for all help given discussing the research.

I am extremely thankful to my sister, Helma, who insisted (kind of pushed me) I should come to do my doctoral studies here. She is not only my sister, but the foundation of my life. Without her, I would probably had stopped in the bachelor degree, and probably I would be now working as a mere analytical chemistry in some randomly Brazilian company. She have dedicated her life to me, being an available support at any time of the day, making enormous effort to keep on visiting me quite often; therefore, I humbly dedicate this thesis to her, who I am sure is really proud of this achievement!

I am deeply thankful to Dimitar, the love of my life, for walking this difficult road with me during these years. He had played a fundamental role on the improvement of my English, and I am really thankful for that! I am also really thankful for his every-day support, for sacrificing the comfort of his daily routine during several months in order to take care of his sick honey at home, for filling my life with love, for making my days bright, for being at my side during all these past years, for everything! I also would like to dedicate this thesis to him, since the written process of the thesis has affected his routine too.

My deep acknowledgements to my lovely parents (Edson and Dione) who had prayed constantly for me, helping in each step of this journey. Many thanks to all my family, especially to my brothers (Helisson and Mardel), my nephews (Lucas, Rhuan and Estela), my aunts (Eline, Elza, Élia and Flor de Nisse), my uncles (Élio and José), my cousins (Thiago, Paula and César), my godson (Hudson), my goddaughter (Bruna), and my family-in-law (Ivan, Tania, Kaloyan, Luíza and Fabiana) who are all really supportive, being an amazing family!

I am also extremelly thankful to Finland for the fascinating heath care system, which had hugged me when I needed: Kiitos Suomi! In this regard, my deepest and sincere acknowledgement to Dr. Mika Junnila for my new hips which are working amazingly fine due to his great work: kiitos paljon! I am also really thankful to the main nurse Hanna Metsämäki for all arrangements before and after the surgeries! My sincere acknowledgement to my physiotherapist, Jutta van der Woude, who have been helping me to recover during the postoperative period.

Many thanks to Antti (aka ystäväni), Bhushan (aka mera dost), Isabella (aka Bella), Maria (naapuri ja ystävä), Vanessa (aka nova gestão), Fabrício (aka chaveirinho) and Milla for being really supportive friends in all needed moments, always helpful with the research discussion, and advises for future plans! I thank them all for making my life brighter!

I would like to thank all my friends for all support in the difficult moments. My special and sincere acknowledgement to Dindo, Dinda, Gracy, Manuel, Vesa, Pasi, Salla, Aleksi, Sini, Miko, Hanna and Wilma. Also, my deep gratitude to my lovely neighbors and friends, especially Auli, Aleksi, Rico, Lena, Olivia, Laura and Tuomas. Many thanks to Alan Roberto and Fabrício for being the guardians of my sister during this period I have been away.

I would like to thank my first supervisor, Ariel Élder Zanini, for creating my interest for clay minerals and their beautiful features! He had planted the seed and I continue developing the research! Many thanks to him and his wife, Alba Zanini, who are amazing friends in my life!

I also would like to express my gratitude to professor Michael Bojdys for the friendship, for all productive discussion about future applications of the materials developed in the current thesis, and for all career advises.

Many thanks to all staff from my research group (Inorganic Materials Chemistry Group), and the Laboratory of Material Chemistry and Chemical Analysis of the University of Turku, especially Carita, Jukka, Ari, Minnea, Emilia, Esko, Jaakko and György! I am really thankful for the nice working environment I have found here! Also, my acknowledgment to Laura Pihlgren who had given to me an amazing reception at my arrival in the department, and Petri Ingman for the nice socializing evenings of the department!

Lastly, but not less important, many thanks to Neilikka! She does not know how to read and probably does not understand anything I say, but she makes my life happier!

Table of Contents

Abstract

UNIVERSITY OF TURKU
Faculty of Mathematics and Natural Sciences, Department of Chemistry, Laboratory of Materials Chemistry and Chemical analysis

SANTOS, HELLEN SILVA: Halogen Hectorites: Smectites Designed to Luminesce.
Doctoral Thesis, 180 p.
December 15, 2017

The smectites represent a versatile class of clay minerals, offering possibilities of applications in several industrial and scientific fields. The hectorite belongs to this class, but it has the advantage of production through low-cost and relatively fast methods, presenting a flexible and tailorable structure which allows modifications on its composition to better match the desirable application. The current thesis discusses the synthesis and characterization of hectorite-based materials designed to act as host lattices for optically active species. In view of that, since the common hectorite structure has OH^- ions in its composition, it is not the optimum material for luminescence applications because the hydroxyl ions may lead to luminescence quenching *via* multiphonon de-excitation. For this reason, the nanoclay materials discussed in the current thesis were synthesized based on the hectorite structure, but replacing its hydroxyl ions with halogens, generating the fluorohectorite (F-Hec), chlorohectorite (Cl-Hec), bromohectorite (Br-Hec) and iodohectorite (I-Hec) materials. Moreover, from the best of my knowledge, the current research is pioneering in the synthesis of the Cl-Hec, Br-Hec and I-Hec materials.

The halogen-hectorites (X-Hec) materials have been obtained with similar crystal structure to the nanocrystalline fluorohectorite, presenting a d_{001} spacing of 14.30 Å and nanoscale crystallite sizes. All X-Hec behave as mesoporous materials, having specific surface areas ranging from 240 to 540 m^2g^{-1}, showing also good thermal stability (up to 750 °C). Thus, the X-Hec materials show strong potential to act as host lattices for optically active species, generating luminescent materials. All X-Hec materials (without doping) show a blue-green emission under UV radiation and short persistent luminescence (ca. 5 s), having their luminescence features attributed to a titanium impurity which acts as the luminescent center in these materials. Furthermore, the X-Hec materials were proven to be suitable host lattices for rare earth ions (RE^{3+}) through the doping of Cl-Hec and F-Hec materials with Eu^{3+} and/Tb^{3+} (without the usage of “antennas” compounds), producing red- and green-emitting materials.

Tiivistelmä

TURUN YLIOPISTO
Matemaattis-luonnontieteellinen tiedekunta, Kemian laitos, Materiaalikemian ja kemiallisen analyysin laboratorio

SANTOS, HELLEN SILVA: Halogeenihektoriitit: Luminovaksi suunnitellut smektiitit
Väitöskirja, 180 s.
15.12.2017

Smektiitit ovat monipuolisia savimineraaleja, joilla on mahdollisia sovelluksia useilla teollisilla ja tieteellisillä aloilla. Hektoriitti kuuluu tähän luokkaan, ja sen etuja ovat edullinen tuotanto suhteellisen nopeilla menetelmillä. Joustavan ja räätälöitävän rakenteensa ansiosta sen koostumusta on mahdollista muuttaa vastaamaan haluttua sovellusta. Tämä väitöskirja käsittelee hektoriittipohjaisia materiaaleja, jotka on suunniteltu toimimaan isäntähilana optisesti aktiivisille ioneille. Koska tavallinen hektoriitti sisältää rakenteessaan OH^- ioneja, se ei ole optimaalinen materiaali luminesenssisovelluksiin, koska hydroksyyli-ioni voi johtaa luminesenssin sammumiseen monivärähdysprosessin kautta. Tästä syystä tässä väitöskirjassa käsitellyt nanokokoiset savimateriaalit syntetisoitiin käyttäen hektoriitin perusrakennetta, mutta sen hydroksyyli-ionit korvattiin halogeeneillä, jolloin muodostuu fluoro- (F-Hec)-, kloro- (Cl-Hec)-, bromo- (Br-Hec)- ja jodohektoriitti (I-Hec). Lisäksi tämä tutkimus on ensimmäinen laatuaan Cl-Hec-, Br-Hec- ja I-Hec-materiaalien synteesissä.

Halogeenihektoriittimateriaalien (X-Hec) kiderakenne on samankaltainen kuin nanokiteisen fluorohektoriitin, jossa d_{001}-etäisyys on 14,30 Å ja kiteiden koko on nanomittakaavassa. Kaikki X-Hec:t käyttäytyvät kuten mesohuokoiset materiaalit ja niiden ominaispinta-ala on 240 - 540 m^2g^{-1}. Ne osoittautuivat myös termisesti stabiileiksi jopa 750 °C asti. Kaikki tämän tutkimuksen X-Hec-materiaalit (seostamattomat) tuottavat sinivihreää emissiota virityksen tapahtuessa UV-säteilyllä ja lyhyen viivästyneen luminesenssin (noin 5 s). Nämä luminesenssipiirteet ovat peräisin pitoisuudeltaan ppm-luokan Ti^{3+}-epäpuhtaudesta, joka toimii luminesenssikeskuksena näissä materiaaleissa. Lisäksi X-Hec-materiaalit osoittautuivat sopiviksi isäntähiloiksi harvinaisille maametalli-ioneille (RE^{3+}) seostettaessa Cl-Hec- ja F-Hec-materiaaleja Eu^{3+}/ Tb^{3+}: lla, mikä tuotti punaisena ja vihreänä loistavaa materiaalia.

List of Original Publications

The results and discussion presented in this thesis are based on the following publications and a complementary part of unpublished results. All publications are displayed in the end of the book and are summarized in the thesis, being cited in the text according to their respective Roman numerals in the list below.

I. Santos, H.S., Lastusaari, M., Laihinen, T., Viinikanoja, A., Brito, H.F., Rodrigues, L.C.V., Swart, H.C., and Hölsä, J., Persistent Luminescent Non-Doped Layered Nanosilicate, *Materials Today Proceedings*, **3** (2016) 2822-2830.

II. Santos, H.S., Carvalho, J.M., Viinikanoja, A., Hyppänen, I., Laihinen, T., Romani, E.C., Larrudé, D.G., Tuominen, M., Laukkanen, P., Swart, H.C., Brito, H.F., Hölsä, J., and Lastusaari, M., Glowing Synthetic Chlorohectorite: the Luminescent Features of a Trioctahedral Clay Mineral, *Journal of Luminescence*, **192** (2017) 567-573.

III. Santos, H.S., Laihinen, T., Rodrigues, L.C.V., Sinkkonen, J., Mäkilä, E., Damlin, P., Nakamura, L.K.O., Hölsä, J., Brito, H.F., and Lastusaari, M., Red- and Green-Emitting Nano-Clays Materials Doped with Eu^{3+} and/or Tb^{3+}, *Journal of Luminescence*, **xx** (2017) xxx-xxx (submitted).

IV. Santos, H.S., Norrbo, I., Laihinen, T., Sinkkonen, J., Mäkilä, E., Carvalho, J.M., Damlin, P., Brito, H.F., Hölsä, J., and Lastusaari, M., Synthesis and Features of Luminescent Bromo- and Iodohectorite Nanoclay Materials, *Applied Sciences*, **7** (2017) 1243.

Abbreviations and Symbols

2D	two-dimensional
2θ	Bragg’s angle
A	non degenerated energy levels
BET	Brunauer-Emmett-Teller method
Br-Hec	bromohectorite
CCD	configurational coordinate diagram
Cl-Hec	chlorohectorite
CT	charge transfer
E	twofold degenerated energy levels
F^+	anionic vacancy (color center) with double positive charge
FED	field-emission displays
F-Hec	fluorohectorite
FTIR	Fourier transform infrared
FWHM	full width at half maximum
H_0	central field term
H_{e-e}	electron-electron repulsion interaction term
H_{SO}	spin-orbit coupling term
ICP-MS	inductively coupled plasma mass spectroscopy
I-Hec	iodohectorite
J	total orbital and spin angular momentum
L	orbital angular momentum quantum number
LEDs	light emitting diodes
LMCT	ligand-metal charge transfer
MAS NMR	magic angle spinning nuclear magnetic resonance
ppm	parts per million

RE	rare earth
RGB	additive color model based on red, green and blue
RT	room temperature
S	spin quantum number
SSA	specific surface area
STEM	scanning transmission electron microscope
T	threefold degenerated energy levels
T:O	tetrahedral:octahedral type of clay minerals’ layer structure
T:O:T	tetrahedral:octahedral:tetrahedral type of clay minerals’ layer structure
TGA-DSC	simultaneous thermogravimetry and differential scanning calorimetry
TL	thermoluminescence
TMS	tetramethylsilane
UV	ultraviolet
V_{CF}	non-spherical crystal field term
$V_O^{\bullet}$	oxygen vacancy occupied with one electron
$V_O^{\bullet\bullet}$	empty oxygen vacancy
X-Hec	halogen-hectorites
XPD	X-ray powder diffraction
XPS	X-ray photoelectron spectroscopy
XRF	X-ray fluorescence
Δ	crystal field strength
τ	luminescence lifetime

1. Introduction

The luminescence phenomena such as aurora borealis as atmospheric glow or in the bioluminescence of certain living organisms, for instance the firefly, glowworm, phosphorescent wood and flesh or “burning of the sea” have been a part of nature for a very long time. The first man-made luminescent material known as the Bolognian stone was discovered in the 1600s, but the term “luminescenz” was created later, in 1888, by Eilhardt Wiedemann who had described it as “all those phenomena of light which are not solely conditioned by the rise in temperature” [1]. Nowadays, luminescence phenomena play an important technological role for the humankind, since it is used in several applications such as light emitting diode (LED) materials and devices, television screens and plasma panels, fluorescent lamps, signalization, bioimaging etc. [2,3]. Therefore, luminescence is a continuous research subject in several fields, aiming at the development of new materials and devices.

A luminescent material is characterized by emission of electromagnetic radiation after energy absorption [3,4]. The luminescence excitation can be categorized according to the types of excitation source, e.g. UV and visible radiation (photoluminescence), beam of energetic electrons (cathodoluminescence), X-rays (X-ray excited luminescence), heating (thermoluminescence), etc. [2,4]. A luminescent system consists of at least a host lattice and a luminescent center (or activator) with both components having equal importance: even the best luminescent centers cannot show luminescence emission without a suitable electronic structure and/or lattice vibration energies of the host lattice [5]. New luminescent materials are created through the development of dopant species (activator ions) and/or appropriate host lattices, but because the host lattice is the majoritarian component of a luminescent system, it also normally represents most of the production cost. For this reason the research discussed in the current thesis has been focused on the development of new materials to act as host lattices for optically active species, generating novel and low-cost luminescent materials.

Clay minerals represent a broad groups of materials commonly used as host lattices for optically active species (either inorganic or organic species) due to their low cost, abundance and versatile structure [6,7]. Among this wide class of minerals, the synthetic hectorite is an attractive candidate for a host lattice because of its thermal, chemical and mechanical stability [8]. Moreover, high amounts of hectorite can be synthesized at low costs due to is formation at temperatures and pressures close to normal temperature and pressure (NTP) conditions [9]. However, when luminescence applications are intended, the hydroxyl groups present in the hectorite' structure may represent a barrier because the high energy phonons of the OH^- ions ($3500\ cm^{-1}$) may lead to luminescence quenching by multiphonon de-excitation [5].

Therefore, the current work has focused in developing synthetic clay materials based on the hectorite structure, but re-designing its structure by replacing its hydroxyl groups with halogens (F, Cl, Br, I) [I - IV]. These synthetic halogen-hectorites (X-Hec) have shown a strong blue/green emission without additional doping due to a Ti^{3+} impurity in their structure acting as luminescent center. This thesis discusses several advantageous physical and chemical features present in the X-Hec materials, as well as the effect of the strength of the π-donor ligands (the halogens) on the luminescence properties of the materials. Moreover, from the best of the author's knowledge, the research presented here is first of its kind regarding the synthesis of the chlorohectorite (Cl-Hec) [II], bromohectorite (Br-Hec) and iodohectorite (I-Hec) nano-clay materials [IV]. Furthermore, some of the materials were doped with Eu^{3+} and/or Tb^{3+} generating red- and green emitting nano-clay materials, thus confirming the capability of the X-Hec to host optically active species and demystifying the necessity of an “antenna” compound to produce luminescent materials from clay materials doped with rare earth (RE) ions [III].

1.1. Aims of the experimental work

The main aims of the research were the following:

- To synthesize new materials based on the hectorite structure but replacing its hydroxyl groups by halogens (Publications I-IV).
- To evaluate the potential of the new clay minerals synthesized to act as host lattices for optically active species (Publications I-IV).
- To dope some of the new matrices with RE^{3+} ions generating new luminescent materials (Publication III).
- To characterize the physical and chemical features of all synthesized materials by using different techniques (Publications I-IV).
- To study the luminescence properties of the materials and to elucidate the mechanisms of luminescence involved in the emissions (Publications I-IV).

2. Literature Review

2.1. Basic requirements for photoluminescence

The photoluminescence phenomenon can be defined as the emission of light by a certain material after it has absorbed a photon of higher energy [10]. A basic photoluminescent material must possess, at least, two components: the host lattice and the luminescent center (also called activator) [5]. When the electrons of the luminescent center are promoted to excited states, their radiative return to the ground state may emit light (Figure 1, left), i.e. luminescence, which can occur through different mechanisms. Even though all kinds of compounds can be promoted to the excited state by energy absorption, not all of them show luminescence, because the radiative emission competes with the nonradiative return to the ground state. Therefore, in order to obtain efficient luminescent materials this nonradiative process should be suppressed and the radiative returns should dominate [5]. The nonradiative process contributes to heat the host lattice by exciting its vibrations [4]. When the exciting radiation is not absorbed directly by the luminescent center, a more complex system is required: for instance, another ion (named sensitizer) may absorb the exciting radiation and transfer it to the activator (Figure 1, right) [5].

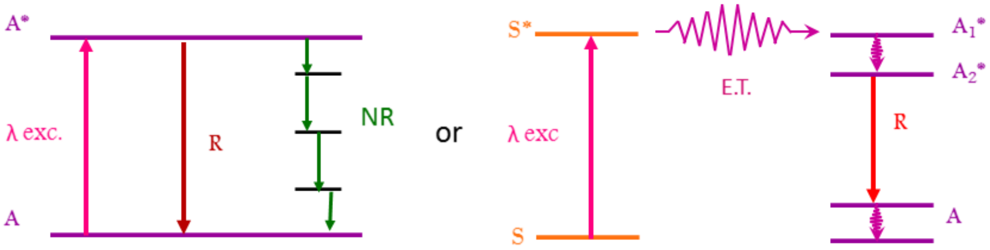

Figure 1. The energy level scheme of a general luminescent center (left), and the scheme of energy transfer from a sensitizer to the luminescent center (right). In the schemes, A is the luminescent center (activator), λ_{exc} is the excitation wavelength, S is the sensitizer, E.T. is energy transfer, R represent the radiative return and NR the nonradiative return to the ground state (adapted from [5]).

A given luminescent center usually has its optical properties influenced by the host lattice, since the surroundings of the activator are changed accordingly. Therefore, the spectral properties of a given ion in different host lattices can be attributed to some main factors [5]. Typically, the host lattice should have a wide enough band gap (not to absorb the emitted radiation) and a rigid structure. A rigid structure is required to avoid an easy excitation of the lattice vibrations, because they can lead to non-radiative relaxation, which decreases the efficiency of the luminescence. Besides, the host lattice cations and anions should not have energy levels which could interfere in the radiative emission [11]. The covalency degree of the bonds between the activator ion and the host lattice also affects the luminescence features of the material: the increase of covalency decreases the interactions between the electrons since they are shared among wider orbitals, shifting the energy of the electronic transitions to lower energy, which is called the nephelauxetic effect. The crystal field provided by the host lattice also influences the optical properties of the activator, since the strength of the crystal field determines the spectral positions of certain optical transitions. Moreover, if the host lattice offers an inhomogeneous symmetry to the surroundings of the activator, i.e. if the activator occupies different sites (with almost identical symmetry) in the host lattice, it will generate a broadening of the spectral bands due to lack of translational symmetry [5].

Some basic features are also desirable from the luminescent center: it needs to be optically active and capable of absorbing energy without dissipating it before the radiative emission [3]. When a solid luminescent material is obtained through the doping of the host lattice with the desirable activator, it is also necessary to consider the solubility, mobility and charge of the activator [11]. In order to obtain a homogeneous solid solution, the following criteria need to be met: (i) the difference between the radii of the doped ions and the replaced ones should not exceed 15 % (to avoid phase segregation), (ii) the doped and replaced ions should have similar charges (to avoid need for charge compensation), and (iii) the structures of the host lattice and a material where the intended dopant has a 100 % occupancy in its intended site should be similar [11,12]. Furthermore, the host must be carefully matched to the luminescent center due to the effect of crystal phonon energy branches on the localized modes of the activator [3].

2.2. Absorption of excitation energy

The radiative emission by a given material is conditioned to the appropriate absorption of the exciting energy. The electronic transitions from the ground to the excited state not always occur as an optical transition. The occurrence of the optical transitions is governed by selection rules, which the two main rules are: (i) transitions between levels with different spin levels are forbidden ($\Delta S \neq 0$), and (ii) transitions between levels with the same parity are forbidden [5].

Usually, there is a strong correlation between the absorption and excitation spectra of a luminescent material; in both measurements it is possible to get information about the absorption of the exciting energy, since it can occur through the host lattice, the sensitizer or the activator itself [13]. Several processes may promote the optical absorption of visible or ultraviolet radiation. However, since the current thesis is focused on materials based on clay minerals, only the electronic transitions fundamentally important for luminescent minerals [4] are listed below:

- <u>d–d or f–f electronic transitions of transition metals or RE ions</u>: Here, the energy levels of an ion with a partially filled d- or f-electron shell depend of the symmetry provided by the host lattice, which influences the splitting of the levels. The intensities of d-d and f-f absorption bands may vary according to the concentration of the absorbing ion, and by a combination of the symmetry at the surroundings of the activator with quantum mechanic selection rules.
- <u>Metal to metal charge-transfer (CT) between transition metal ions with different valence states</u>. It refers to the absorption by electronic transference via a photon as input of energy, which is typical of ions

capable of adopting multiple valence states, e.g. Fe^{2+} and Fe^{3+} or Ti^{3+} and Ti^{IV}.

- Ligand to metal CT (interband transition). It occurs when the ligand transfers electron density to the metal cation. This absorption mechanism is typically observed in oxides, due to oxygen (O_2^{-}) to metal CT which are, usually, related to electronic delocalization or photoexcitation of an electron into the conduction band.
- Radiation induced centers originated from natural sources, for example, the electron-hole centers induced by ionizing radiation of green diamonds.

Even though the absorption spectrum may display several pieces of information regarding the energy levels of a given material, the excitation spectrum is a more specific measurement to indicate the absorptions of exciting energy which produce luminescence, because it measures the transition from the specific electronic level allowing an effective study of the luminescence mechanism [4].

2.3. Luminescence emission: the radiative transitions

The luminescence emission is by definition the radiative return to the ground state. However, there are many other possibilities of returning to the ground state besides the radiative return. The competitive processes are mainly the nonradiative returns such as multiphonon relaxation or cross-relaxation. Besides, the radiative transfer to another ion also represents a competitive process [13]. The radiative return can occur either with the absorption and emission processes within the same luminescent center or influenced by the host lattice [14]. Therefore, luminescence in inorganic materials (including minerals) can occur through different types of absorption/emission mechanisms, affected by the energy level structure in such materials. These energy levels comprise those of the host lattice (band gap), dopants (activator, sensitizer), impurities (optical centers) and structural defects (energy traps) (Figure 2) [11].

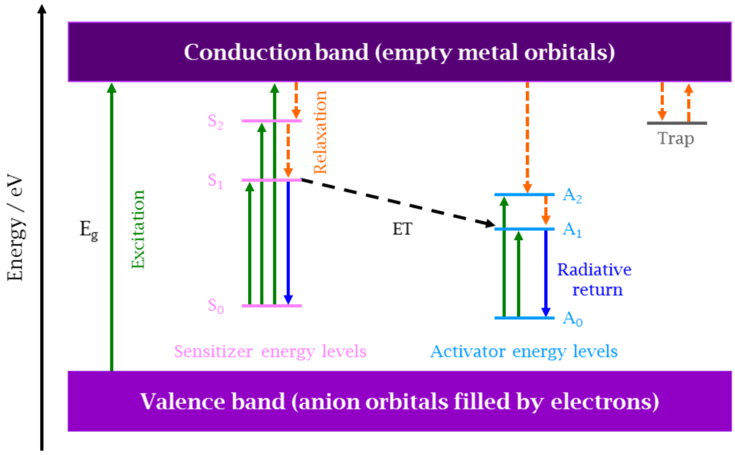

Figure 2. The overall representation of luminescence processes. S_n represents the n energy levels of the sensitizer, and A_n represents the activator (A) energy levels. ET: energy transfer.

The configurational coordinate diagram (CCD) is a useful graphical tool to help understanding the process of phonons emission followed by several radiative transitions and also the nonradiative processes. The CCD treats electronic energy levels as parabolic potentials with vibrational levels. The Figure 3 shows a CCD illustrating the mechanism of luminescence emission in a broad spectral band, taking the assumption that there exists an offset ΔR between the parabolas of the ground state (g) and the excited state (e). This shift is due to the metal-ligand distance R being different in the ground state than in the excited state. The exciting radiation reaches the luminescent center promoting its electrons from the ground energy state to the high vibrational level of the excited state. Thereafter, the center relaxes nonradiatively to the lowest vibrational level of the excited state by releasing excess of energy to the surroundings.

Subsequently, the electron returns to the ground state either by means of photon emission (radiative return), or through heat release (nonradiative return) [13]. The difference on the R scale between the minimum of the (lowest) excited state parabola and that of the ground state one affects both the width of the emission band as well as the Stokes shift, i.e. the energy difference between the absorption and emission maxima [5]. The radiative energy transfer process would compete with the radiative relaxation only if the emission band of the donor coincides with the absorption band of the acceptor [13].

Such type of broad band exemplified above is characteristic of several optical transitions such as (i) d→d transitions in the partly filled d-shell of transition metal ions, (ii) d→f transitions in RE ions, and (iii) s^2 type ions. Sharp emission bands are observed when the chemical bonding character is (almost) the same in the excited and ground states, or when the electronic transitions hardly participate in the chemical bonding (for example f→f transitions in RE ions). When the electronic states involved in the optical process participate in the chemical bonding, two main features play important role on the emission: the nature of the bonding (ionic, covalent) and the symmetry of the site where the luminescent center is localized. When these features have to be evaluated, the ligand field theory can be used to obtain a general description of the system [15].

The intensity of the emission can be evaluated through the lifetime of the excited state. Allowed transitions have short lifetimes ($10^{-7} – 10^{-8}$ s), while solids with strongly forbidden transitions have longer lifetimes (few 10^{-3} s). In a system with two energy levels (as the one illustrated in the Figure 3), the population of the excited state at a given time t($N_e(t)$) can be expressed through Eq. 1:

$$N_e(t) = N_e(0)e^{-t/\tau R} \tag{1}$$

Where, $N_e(0)$ is the initial number of ions in the excited state and τ_R is the radiative decay time (i.e. the time when the population has decreased to 1/e) [5].

A plot of the logarithm of the emission intensity versus time results in a linear curve when only one type of luminescent center is involved. In such cases the luminescence lifetime (τ) is obtained by plotting the experimental data as an exponential function ($l(t) = k\exp(-t/\tau)$). When more than one type of luminescent centers are involved or the same luminescent center is occupying different sites in the host lattice, this linear curve cannot be obtained and more components have to be considered in the exponential fitting [5,16]. The lifetime can be used as parameter to classify the photoluminescence phenomena into two different terminologies: fluorescence ($\tau = 10^{-9} – 10^{-3}$ s, i.e. allowed transitions) and phosphorescence ($\tau = 10^{-3} – 100$ s, i.e. forbidden transitions) [15]. However, this classification is commonly not used in the context of inorganic luminescent materials, because the definition of allowed and forbidden is often not straightforward.

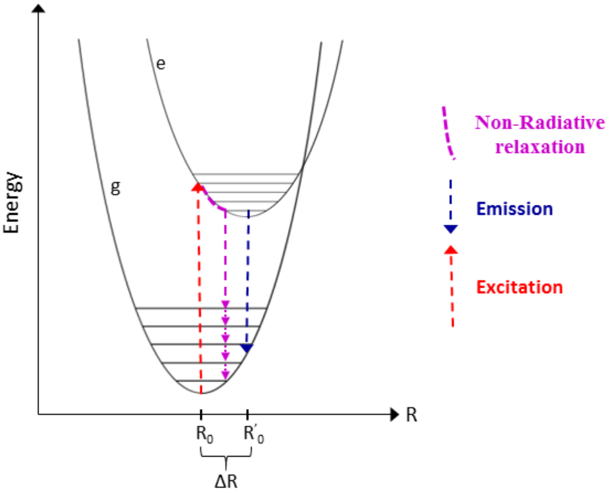

Figure 3. The configurational coordinate diagram in a broad emission band: g represents the ground state and e the excited state.

2.4. Nonradiative transitions

The energy absorbed by a certain material can be reemitted as radiation (luminescence) or dissipated to the crystal lattice (nonradiative processes). Efficient luminescence usually requires the suppression of the nonradiative routes, but some nonradiative processes can be used to enhance the luminescence efficiency [5,13].

Figure 4 shows CCDs representing the physical processes of nonradiative transitions in an isolated luminescence center. Figure 4a represents the cases with $\Delta R > 0$ between the excited state and the ground state. If the temperature is sufficiently high, the electrons from the excited state may reach the crossing of the parabolas, and through the crossing, the electrons return to the ground state in a nonradiative manner, releasing the energy as heat to the lattice [11,13,16].

Figure 4b exemplifies the case when $\Delta R = 0$, i.e., the parabola of the ground and excited state are parallel. In this case, there are usually no intersections between the ground and excited state parabolas, but nonradiative relaxation is still possible. That is, if the energy difference between the excited and ground states is equal or less than four to five times the higher vibrational frequency of the surrounding, multiple phonons may relax the excitation instead of a radiative emission. This process is called multiphonon de-excitation [13].

Figure 4c illustrates the case when radiative and nonradiative processes are, both, probable. There are two excited states: one with the same configuration of the ground state (parallel parabolas represented with solid lines) and other belonging from a different configuration (dashed line). The transition from the ground state to the lower excited state (solid line) is forbidden but allowed to the upper excited state (dashed line). Therefore, the absorption occurs in the upper excited state from where the energy is transferred nonradiatively to the lower excited state. Subsequently, the emission occurs radiatively [5,13]. This is an example of the possibility that nonradiative processes can generate luminescence indirectly [13].

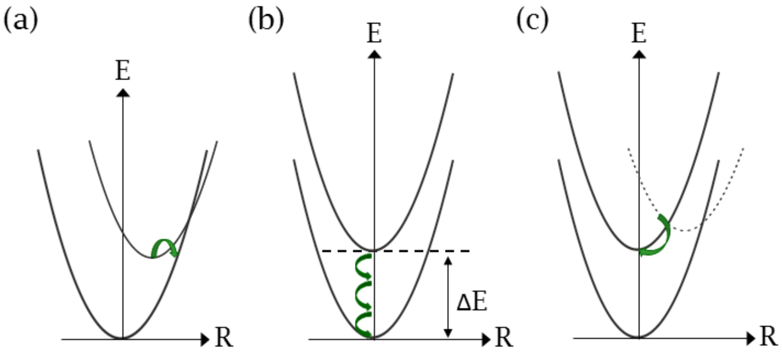

Figure 4. CCD representing nonradiative transitions.

2.5. Some examples of luminescent centers

2.5.1. Titanium (Ti^{3+} and Ti^{IV})

The first successful material with titanium as luminescent center was demonstrated by Peter F. Moulton in 1982 with the Ti^{3+}-doped sapphire (Al_2O_3:Ti^{3+}), used as tunable solid-state laser in the red-NIR range [17]. Since then, the necessity of wide-range tunable lasers has stimulated researches focused on new host lattices for Ti^{3+} [18]. Besides the usage for laser development, the role of titanium has been proven as luminescent center generating red or blue-green emission in some minerals such as titanite ($CaTiSiO_5$) [4,19], benitoite ($BaTiSi_3O_9$) [20] or other titanium bearing minerals [4]. Based on these features, several researches had developed luminescent materials with $Ti^{3+/IV}$ as activator ions to produce optical fibers [21] or other lighting/optical applications [22–31]. Also Ti^{2+} has been reported as a NIR emitter in some halides, but the emission is very easily thermally quenched below room temperature [4]. Therefore, it is not considered further in this thesis.

Titanium is a transition metal with an incompletely filled d shell, whose electronic configuration is [Ar] $3d^2$ $4s^2$. Therefore, its trivalent and tetravalent ions have a $3d^1$ and $3d^0$ electron configuration, respectively. The oxide materials doped with titanium have their optical features defined by the presence of Ti^{3+}, Ti^{IV} and Ti^{3+}-Ti^{4+} pairs [26,29]. The comprehension of the role of the $Ti^{3+/IV}$ ions as luminescent centers requires knowledge from the energy levels originating from their electronic configurations. Therefore, the next two sections explain the absorption and emission of radiation processes for $3d^1$ and $3d^0$ ions.

2.5.1.1. Luminescent centers with d^1 configuration

The energy levels arising from the d^n ($0 < n < 10$) configuration of transition metals have been calculated by Tanabe and Sugano considering the mutual interaction between the d electrons and the crystal field around them. Figure 5 shows the results for the d^1 configuration, which has the simplest energy level diagram of the ions with the d^n configuration. In the case of a free ion, the d^1 configuration is represented by the symbol ^2D. When the ligands are added around the d^1 ion (generating the octahedral geometry in this case), the energy levels are no longer degenerated and the crystal field strength is higher than 0. The ground energy level is considered to be at zero energy and thus it coincides with the x-axis. When the free ion is considered, the levels are marked ^{2S+1}L, where S is the total spin quantum number, and L the total orbital angular momentum. The degeneracy of these levels is 2L+1, which is affected by the crystal field. The energy levels originating from the crystal field are marked ^{2S+1}X, where X may be A, E and T if the levels have no degeneracy, twofold degeneracy and threefold degeneracy, respectively [5].

In the case of d^1 configuration ions (Figure 5), the free ion displays fivefold orbital degeneracy (^2D). When the six ligands are added generating the octahedral symmetry, these degenerated orbitals split into two energy levels (^2E and ^2T). Thus, in octahedral d^1 ions the optical absorption process occurs due to electronic transitions from $^2T_2$ to ^2E, and the crystal field value is obtained from the energy difference between these two levels. The energy of the $^2T_2 \rightarrow {}^2E$ transition is strongly affected by the strength of the crystal field (Δ). In general, trivalent metal ions have Δ values of about 20000 cm^{-1}, thus showing the respective optical transition in the visible spectral region, which causes materials with these ions to be colored [5].

Since the $^2T_2 \rightarrow {}^2E$ transition occurs between levels of the d shell, it is a forbidden transition because the parity does not change. As long as this type of transition is involved, the material does not show intense colors. However, the parity selection rule is relaxed through the coupling of the electronic transition with vibrations of suitable symmetry. Thus, the emission of d^1 ions in an octahedral symmetry will occur due to $^2E \rightarrow {}^2T_2$ radiative transitions. The titanium-sapphire laser is based on the broad emission band of Ti^{3+} in the near infrared due to this transition [5]. The d^1 ions most known as luminescent centers are Cr^{5+}, V^{4+}, Mn^{6+} and Ti^{3+} [4]. Due to the fact that the $^2E \rightarrow {}^2T_2$ transition is strongly affected by the crystal field strength, its emission color varies according to the environment surrounding the sites where the d^1 ions reside [4,5].

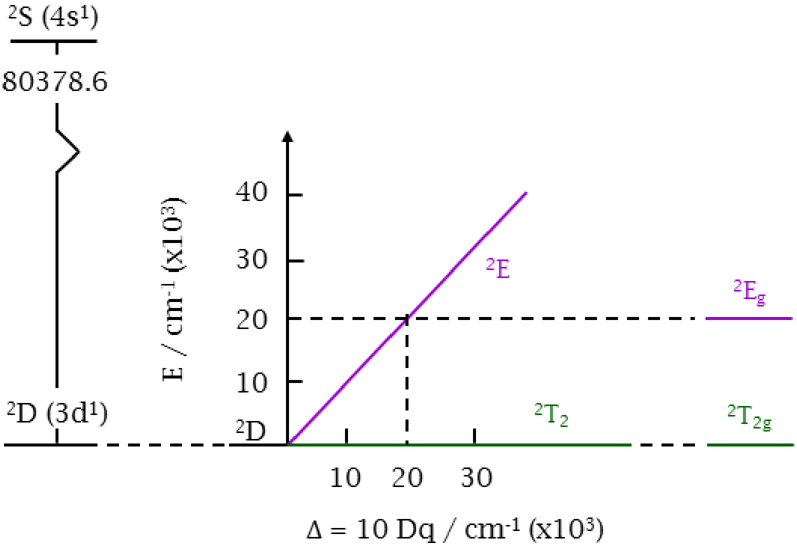

Figure 5. The Tanabe-Sugano diagram showing the energy levels of a d^1 configuration in function of the octahedral crystal field (Δ). ^2D represents the level of a free d^1 ion.

Another good example of a d^1 ion as a luminescent center is the blue phosphor ZrO_2:Ti [27,32–34]. In ZrO_2, the titanium centers were first identified as impurities [34], and after that several studies have been carried out investigating the doping of zirconia with different concentrations of titanium [27,32–34]. It was noticed that anion vacancies are produced from the replacement of one Zr^{IV} by two Ti^{3+} ions, increasing the intensity and lifetime of the blue photoluminescence. The ZrO_2:Ti materials present broad bands in their excitation and emission spectra with maxima at ca. 280 and 475 nm, respectively. This blue emission is attributed to the $e_g \rightarrow t_{2g}$ transition of Ti^{3+} in an octahedral site. This is also the model used to explain the blue emission of the halogen-hectorites materials discussed in the current thesis [I-IV]. The ZrO_2:Ti materials show also persistent luminescence due to the photoionization of Ti^{3+} centers and the trapping of energy to oxygen vacancies and its slow release (Figure 6) [27,32–34].

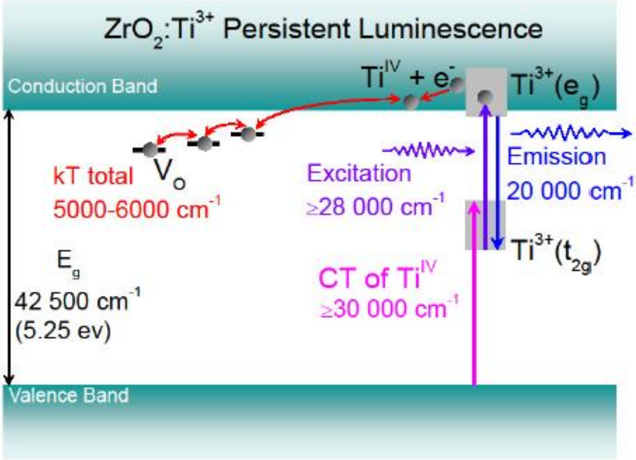

Figure 6. The proposed mechanism for the persistent luminescence of the zirconia doped with Ti^{3+} [27].

A similar blue emission involving Ti^{3+} has been observed also in silicate matrices such as hackmanite ($Na_8Al_6Si_6O_{24}(Cl,S)_2$) through broad excitation and emission bands peaking at ca. 310 and 460 nm, respectively. The blue emission of hackmanite has been explained by a model with Ti^{3+} in a tetrahedral site forming a pair with an oxygen vacancy. Hackmanite shows also persistent luminescence, which is explained to have a mechanism similar to that in ZrO_2:Ti. It has been proposed that an electron is transferred to the conduction band, and subsequently the electron is captured by a half-filled oxygen vacancy ($V_O^{\bullet}$) producing a completely filled oxygen vacancy ($V_O^{\bullet\bullet}$). The radiative return yields emission in the blue region [30,31]. The proposed mechanism for the persistent luminescence of Ti^{3+} impurities into synthetic hackmanites is shown in the Figure 7. The Ti^{3+} emissions in $BaTiO_3$ thin films [23], TiO_2 nanocrystals [22] and

TiO_2:Tb^{3+} nanophosphors (Figure 8) [22] have been explained by emission between Ti^{3+} and defect energy levels.

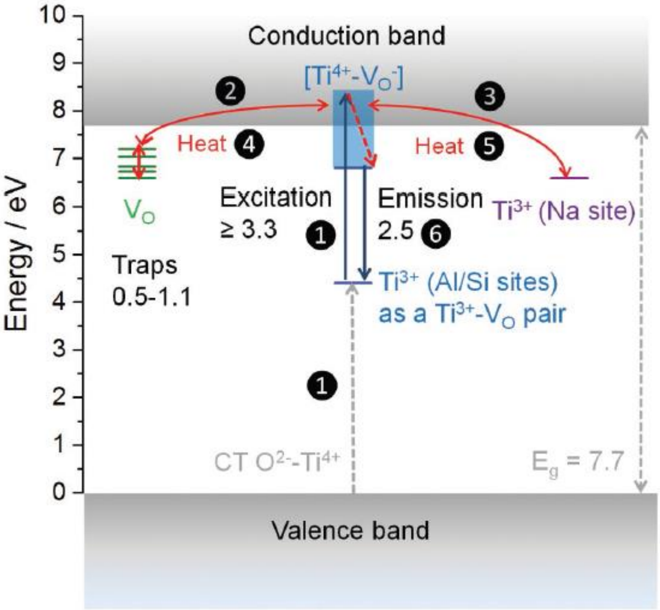

Figure 7. The schematic illustration of the persistent luminescence mechanism of Ti^{3+} impurities in synthetic hackmanites [31].

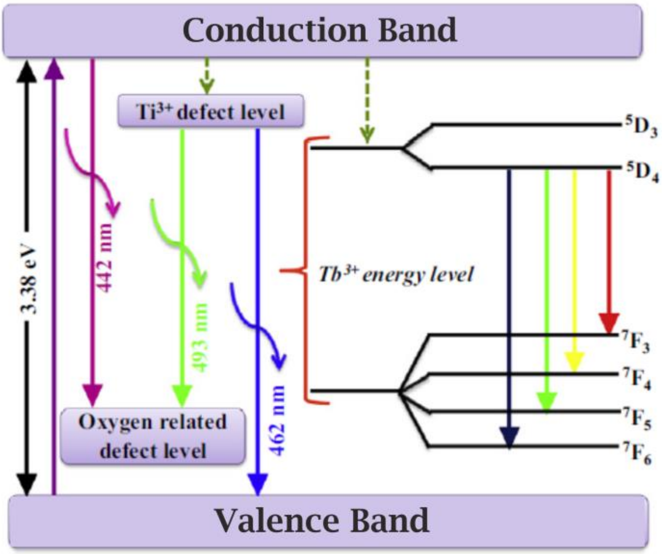

Figure 8. The energy level diagram of TiO_2:Tb^{3+} [22].

On the other hand, several other matrices doped with titanium present intense red or near infrared emissions assigned to the $^2E_g \rightarrow {}^2T_{2g}$ transitions of Ti^{3+} as it is seen for Ti-doped low-silica calcium aluminosilicate glass [28,29], Ti^{3+}-doped silicate, borate and phosphate glasses [26], and thin films of AIN doped with Ti^{3+} deposited on Si substrates and optical fibers [21].

2.5.1.2. Luminescent centers with d^0 configuration

Transition metals with the d^0 configuration, i.e. with a formally empty d shell, absorb the exciting radiation via charge transfer transitions from surrounding anions (i.e. oxygen in oxidic materials) to the d^0 ion. Thus, they show strong and broad excitation bands in the UV region. The spectral position of the generated excitation band depends on a few factors: (i) the nature and number of ligands, (ii) the ionization potential of the $d^1 \rightarrow d^0$ ionization, and (iii) the mutual interaction between ions in the lattice. The respective emission is commonly observed as an intense broad band with a large Stokes shift (1000 – 20000 cm^{-1}). The amount of charge being transferred is usually small, but a considerable amount of electronic reorganization occurs, when electrons are raised from the bonding orbitals of the ground state to the antibonding ones in the excited state. The lifetime of these emissions can be quite long (e.g., 100 – 33500 μs), being longer for lighter d^0 ions. It has been proposed by Van der Waals that the emission state of the d^0 ions are a spin triplet, and thus it is strongly distorted due to the Jahn-Teller effect. Octahedral complexes of d^0 ions have smaller Stokes shift than the tetrahedral ones. Besides, the structural configuration may be related with the luminescence efficiency: complexes of edge or face sharing octahedral or complexes with short metal-oxygen ligands tend to present higher emission efficiency [5].

For minerals, the most important examples of luminescent centers with the d^0 configuration are WO_4^{2-}, MoO_4^{2-}, VO_4^{3-} and TiO_6^{8-} [4]. In the case of the benitoite structure ($BaTiSi_3O_9$), it shows blue luminescence with a broad emission band at ca. 420 nm (half-width of ca. 80 nm) and a lifetime of 2.6 μs. This blue emission has been associated to TiO_6^{8-}, TiO_4^{4-} and TiO_5^{6-} species with the absorption bands being due to the ${}^1A_{1g}\rightarrow{}^1T_{1u}$ as well as ${}^1A_{1g}\rightarrow{}^1T_{2u}$ transitions and the emission band due to the ${}^3T_{1u}\rightarrow{}^1A_{1g}$ transition (Figure 9) [4,20]. Other luminescent materials that have their blue emission assigned to Ti^{IV} centers are, for example, silicate glasses [24], zinc spinel ($ZnAl_2O_4$:Ti) [25], silicate, borate and phosphate glasses [26], and low-silica calcium aluminosilicate glass [28,29].

The origin of the blue emission from titanium-based centers is not fully agreed on in the literature. As detailed above, either Ti^{IV} or Ti^{3+} may be involved [22,30]. Therefore, when a titanium doped material is studied, it is important to investigate the predominant valence of titanium in order to understand the luminescence mechanism involved in the emission process [30].

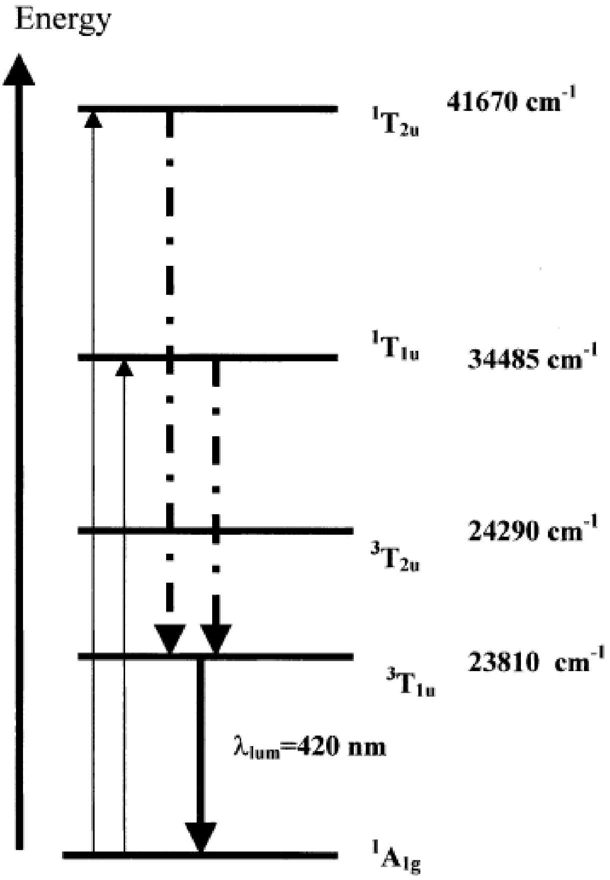

Figure 9. The energy levels of the TiO_6 luminescent center [20].

2.5.2. The rare earth ions ($4f^n$)

The general electron configuration of rare earths is $[Xe]4f^n5d^16s^2$, i.e. they comprise incompletely filled 4f shells. In this configuration, the 4f shells are shielded by outer filled 5s and 5p orbitals as well as electrons on the 5d and 6s orbitals. Because of the shielding, the host lattice has only a minor, yet important, influence on the optical transitions resulting from the $4f^n$ configuration [5]. The shield of the 5s and 5p orbitals gives a stable electronic configuration to the rare earths while the electrons on the 5d and 6s shells are easily removed. Thus, the rare earths tend to form trivalent ions with low reduction potential and electronegativity in order to keep this stable configuration. Besides, in the majority of RE ions, the fourth ionization energy is higher than the three first ionization energies, which culminates into high stability of RE^{3+} ions regarding to the oxidation state. This shielded configuration also leads to a low covalence for the formed chemical bonds. Thus the interaction between RE^{3+} with the ligands present mainly ionic and ionic-dipole character, with a behavior typical of hard acids (Person HSAB classification [35]). Therefore, high similarities are found in the chemical features of different RE^{3+} ions and their spectroscopic properties are also related to this shielding effect which causes the well-defined and characteristic energy levels for the RE^{3+} ions [36].

The energy levels of free RE^{3+} ions are first influenced by the central field (H_0), which can be taken as the hydrogenoid fraction of the level approximation. Since the H_0 term is defined by radial contributions, it represents a totally isotropic spherical symmetry where the 4f energy levels keep their degeneracy (Figure 10). When multielectronic systems are considered, the interelectronic repulsion interactions ($H_{e\text{-}e}$) remove the degeneracy of the 4f configuration, resulting into lower energies for low multiplicity $^{(2S+1)}L$ levels which are separated from higher energy levels by ca. 10^4 cm^{-1}. Then, these levels are affected by the spin-orbit coupling term (H_{SO}) causing the $^{(2S+1)}L$ levels to lose the degeneracy regarding their 2S+1 components of total angular momentum. This gives rise to an energy separation of 10^3 cm^{-1} within the $^{(2S+1)}L_J$ levels (Figure 10). Finally, when the symmetry decreases due to a non-spherical crystal field (V_{CF}), this promotes a degeneracy loss of the $^{(2S+1)}L_J$ levels. These are split into a maximum of 2J+1 Stark components associated with the crystal field symmetry, generating energy separations of ca. 10^2 cm^{-1} (Figure 10) [36].

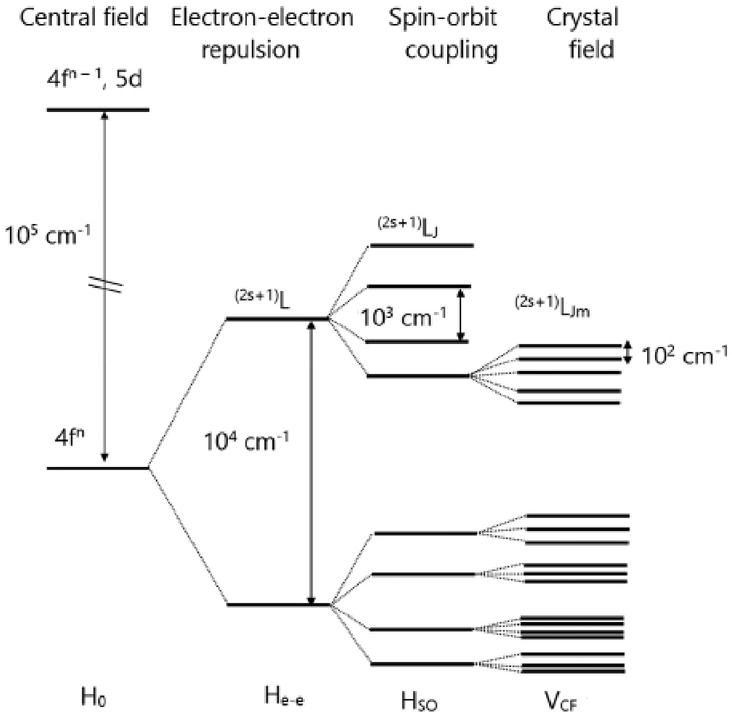

Figure 10. Scheme of the splitting of the energy levels in the $4f^n$ electronic configuration [36].

Because the strength or symmetry of the crystal field does not affect much the final energies of the $^{(2S+1)}L_J$ levels, the energy levels originating from the $4f^n$ configuration do not suffer strong variations even when different chemical environments are considered. These energy levels are shown as a function of number of f electrons for the RE^{3+} ions in the Dieke diagram (Figure 11) [5,36]. The Dieke diagram has an empirical extension up to ca. 70 000 cm^{-1}, however the theoretical calculations are able to determine these energy levels even up to ca. 200 000 cm^{-1} [36].

The optical transitions of RE^{3+} ions are strongly forbidden due to the parity selection rule, and thus most of the rare earth oxides (RE_2O_3) present a white body color. The relaxation of the parity selection rule occurs, if the RE^{3+}

ion occupies a site without inversion symmetry. In such case, uneven components of the crystal field mix a small amount of opposite-parity wave functions (e.g. 5d) into the 4f wave functions, which makes the intraconfigurational $4f^n$ transitions more allowed. This results into an intensity gain. Due to the shielding effect, the $4f^n$ levels appear as parallel parabolas ($\Delta R = 0$) in the CCD, and consequently the respective emissions appear as sharp lines in the spectra. The allowed optical transitions for rare earth ions are interconfigurational, consisting mainly of two different types: (i) CT transitions ($4f^nL \leftrightarrow 4f^{n+1}L^{-1}$, where L is the ligand), and (ii) $4f^n5d^0 \leftrightarrow 4f^{n-1}5d^1$ transitions. Both of them have $\Delta R \neq 0$, and thus they are observed as broad absorption (i and ii) and emission (ii) bands [5]. In general, RE^{n+} ions which are easily reduced have their absorption process attributed to CT transitions. Oppositely, easily oxidable RE^{n+} ions have their absorption processes assigned to 4f-5d transitions.

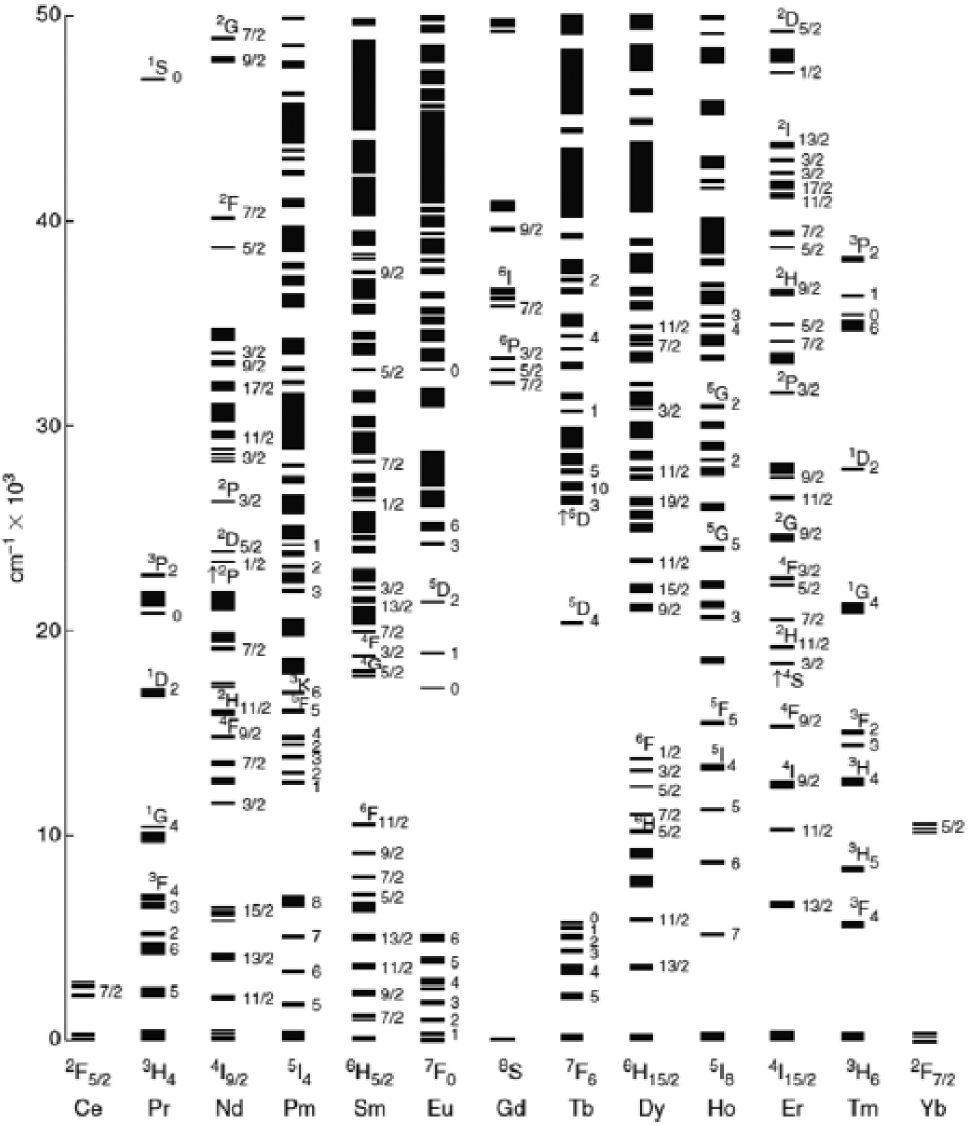

Figure 11. The Dieke diagram showing the energy levels of the $4f^n$ configurations of RE^{3+} [36].

2.5.2.1. Trivalent europium (Eu^{3+})

The electronic configuration of trivalent europium is $[Xe]4f^6$, and usually Eu^{3+} has its main emission in the red region of the spectrum. The emission lines originating from Eu^{3+} are assigned to transitions from the excited $^5D_0$ level to the

^7F_J (J = 0-6) levels. Since the $^5D_0$ level of Eu^{3+} has J= 0 (i.e. its energy level is determined by the central field) it will not be split by the crystal field. Thus, the splitting of the emission transitions originates from the crystal-field splitting of the ^7F_J levels. Additionally, emission lines belonging to higher ^5D levels (i.e. $^5D_1$, $^5D_2$ or $^5D_3$) are also frequently observed [5,36].

The $^5D_0 \rightarrow {}^7F_J$ electronic transitions are of fundamental importance in the operation of several optical devices. Furthermore, they play an important role in the body of investigations considering the spectral features of the 4f-4f transitions of RE^{3+} ions [36]. Since the $^5D_0$ emitting level is non-degenerate and the final J values are low (ranging from 0 to 6), they show peculiar unfolding features affected by the site symmetry. Moreover, the emission spectra are simple enough to allow the identification of the local symmetry around Eu^{3+} [36,37]. Regarding the use as a structural probe, the following characteristics can be associated to the $^5D_0 \rightarrow {}^7F_J$ transitions [5,36,37]:

- In general, the $^5D_0 \rightarrow {}^7F_0$ transition shows one signal related to each chemical environment occupied by the Eu^{3+} ions. However, the presence of this signal depends on both the site symmetry, which determines signal's activity, and the extent of J-mixing, which determines its intensity.
- The intensity of the $^5D_0 \rightarrow {}^7F_1$ transition is almost independent of the chemical environment, because it is due to a magnetic dipole mechanism. This transition can be used as an internal intensity reference for the other transitions of Eu^{3+}.
- The $^5D_0 \rightarrow {}^7F_2$ transition is hypersensitive to the site symmetry. Consequently, it is suppressed in in inversion symmetry. This transition is the main cause for the Eu^{3+} red emission.

- The symmetry of the occupied sites of Eu^{3+} can be compared through the ratio $I(^5D_0 \rightarrow {}^7F_2)/I(^5D_0 \rightarrow {}^7F_1)$, where I is the signal intensity.

There are several commercially important materials developed based on the emission of Eu^{3+}. For example $Y_2O_3:Eu^{3+}$, $Y_2O_2S:Eu^{3+}$ have been used as the red RGB component in fluorescent tubes and television screens [5]. Eu^{3+}-doped materials also play an important role in biomedical applications [38]: e.g. Eu^{3+} complexes based on functionalized triazacyclonane can be used for applications in bioassays and cellular optical imaging [39], Eu^{3+}-activated $NaGdF_4$:Tb/Tm@$NaGdF_4$:Eu@$NaEuF_4$ core-shell-shell nanoparticles can be used for *in vitro* tumor marker detection and tumor-targeted imaging [40], and hydroxyapatite co-doped with Eu^{3+}/Gd^{3+} can be applied for bioimaging *in vivo* [41]. Other interesting materials include $BaLa_2WO_7:Eu^{3+}$ and $BaLa_2WO_7:Eu^{3+},Bi^{3+}$ phosphors that can be used in the production of red LEDs and field-emission displays (FED), respectively [42]. Red LEDs can also obtained from $Y_2WO_6:Eu^{3+}$ nanophosphors [43].

2.5.2.2. Trivalent terbium (Tb^{3+})

The electric configuration of the trivalent terbium is $[Xe]4f^8$. The excitation spectra of Tb^{3+} commonly have a broad band from 220 to 300 nm due to the $4f^8$-$4f^75d^1$ transition, and its emission is observed mainly in the green region of the spectra. This green emission is associated to the $^5D_4 \rightarrow {}^7F_J$ transitions. Among these transitions originating from the $^5D_4$ level, the $^5D_4 \rightarrow {}^7F_5$ one has the highest probability among the electric-dipole and magnetic-dipole transitions. Consequently, it usually presents the strongest intensity (at ca. 550 nm) when the Tb^{3+} concentration is high. Moreover, blue emission can be observed due to the $^5D_3 \rightarrow {}^7F_J$ transitions. The increase of Tb^{3+} concentration decreases the intensity of the emission arising from the $^5D_3$ levels due to cross-relaxation. The ratio between the intensities of the emissions from $^5D_3$ to that from $^5D_4$ depends on the Tb concentration and the host lattice. Because of the high J values of the levels involved in the transitions, the crystal field splits the energy levels into many sublevels. Therefore, the emission spectrum of Tb^{3+} can have a complicated appearance [4,5].

The emission produced by Tb^{3+} ions is used or studied for use in materials with different purposes. For example, it is employed as the green RGB component in fluorescent tubes and television screens in host matrices such as $(Ce,Tb)MgAl_{11}O_{19}$, $Y_3Al_5O_{12}:Tb^{3+}$ and $LaOBr:Tb^{3+}$ [5]. Warm white LEDs can be obtained from the glass phosphor $PbGeO_3:PbF_2:CdF_2$ doped with Tb^{3+}/Sm^{3+} [44], upconversion nanoparticles with a mesoporous coating bonded with Tb^{3+} can be used for *in vitro* confocal imaging [45], and near-UV white LEDs can be produced from $Sr_3La(PO_4)_3:Tb^{3+}$ phosphors [46].

2.5.3. Twofold-coordinated silicon centers

Oxidic silicon materials have been reported to show a blue and UV luminescence due to defects originating from localized states in the SiO_2 structure. This defect has been suggested to be a twofold-coordinated silicon center, i.e. $(SiO_2)^{2-}$ (Figure 12 (a)). The localized states are a fundamental characteristic of materials with only short-range structural order. When disordered structures are considered, their localized states are traps (i.e., defects) for which there is no transport either by charge carriers or energy, even if the concentration of these traps is usually comparable with the concentration of the main atoms of the material [47].

Literature shows several studies where $(SiO_2)^{2-}$ centers have been attributed to be the origin of luminescence in silicates. These include amorphous silica (silicon dioxide glass) [47–49], bulk silica or thin films of SiO_2 [50]. For example, it has been observed that when oxygen-deficient SiO_2 materials are exposed to UV radiation at ca. 177 or 248 nm (7 or 5 eV), intrinsic luminescence is observed as broad emission bands in the UV region at ca. 282 nm (4.4 eV) and in the blue region of the spectra at ca. 460 nm (2.7 eV) [47,48,51–53]. Sometimes, the blue emission of clay minerals has been attributed to the $(SiO_2)^{2-}$ centers as is the case with halloysite ($Al_2Si_2O_5(OH)_4$ [54], a T:O type of clay minerals belonging to the kaolin-serpentine group [55]). Figure 12 (b) shows a typical emission spectrum (λ_{exc}: 248 nm) of oxygen-deficient silicon centers.

The twofold-coordinated silicon centers have been broadly studied by Skuja, who is considered the main reference in this subject [49,51,52,56–58]. Figure 12 (c) illustrates the luminescence mechanism proposed by Skuja for oxygen-deficient SiO_2 luminescent centers [58]. The blue emission band at ca. 460 nm (2.7 eV) arises from triplet-singlet ($T_1 \rightarrow S_0$) transitions, having the corresponding absorption band at ca. 394 nm (3.15 eV). However, this blue emission band also appears under excitation of ca. 248 nm (5 eV) due to conversion from the singlet to triplet ($S_1 \rightarrow T_2$) states (Figure 12 (b)). The broad UV emission band at ca. 282 nm (4.4 eV) is related to singlet-singlet (${}^1S_1 \rightarrow {}^1S_0$) transitions and it is also excited at ca. 248 nm (5 eV). The luminescence decay of both emission bands is well fitted by first order exponential functions, presenting a lifetime of 10.2 ms for the blue band, and 4.2 ns for the UV band [47].

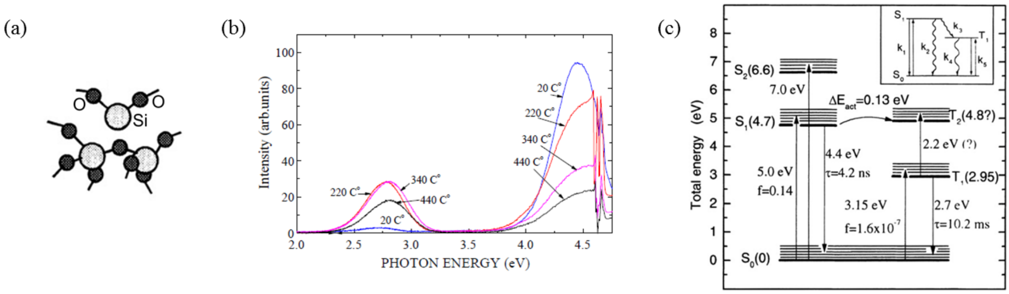

Figure 12. (a) Representation of a $(SiO_2)^{2-}$ center among intact $(SiO_4)^{4-}$ units [58]; (b) The photoluminescence emission spectra (λ_{exc}: 248 nm) of silica glass with extra Si, measured at different temperatures [47]; and (c) The energy levels and electronic transitions in $(SiO_2)^{2-}$ centers, where: f is the respective oscillator strengths, τ is the lifetime, S_n and T_n represent the singlets and triplets states, respectively [58].

2.6. Smectites: a special class of clay minerals

Clay-based materials have been developed and used by humans since Antiquity, and nowadays the clays still are an essential class of raw materials. They are used in many kinds of ceramics (e.g. porcelain, tile, sanitary ware and bricks), paints, plastics, paper, cosmetics, depolluting agents, building materials, rubber, oil drilling, pharmaceuticals, catalysts or catalyst supports etc. Clays are also known as an important component in the prebiotic synthesis of biomolecules since the very beginning of life on Earth. The use of clays in a broad range of applications is made possible by the diverse structures and properties of the clays. Therefore, clay-based materials are the focus of many research fields [59,60].

The clays and the clay minerals represent different classes of materials: clays are a broader class where clay minerals are included. The *Association Internationale pour l'Etude des Argiles* (AIPEA) has established definitions for both classes of materials. The term clay represents a “material composed primarily of fine-grained minerals, which is generally plastic at appropriate water contents and will harden when dried or fired”, whereas the term clay minerals is used for “phyllosilicate minerals which impart plasticity to clay and which harden upon drying or firing”. Phyllosilicates are defined as sheet silicates and, apart from the clay minerals, they also comprise micas, serpentine, chlorite and talc. Clay minerals are a special (and broad) class of materials with distinct features different from those seen for general clay materials [59,55].

The structure of all clay minerals is composed of two types of polymeric sheets. One type has tetrahedral (T) units as the building blocks, and the second one is formed from octahedral (O) units (Figure 13). In the tetrahedral sheets, each tetrahedron consists of a silicon atom coordinated to four oxygens and these tetrahedra are linked to the adjacent ones through three shared corners, i.e. the basal oxygen atoms of the tetrahedron. This arrangement forms interconnected six-membered rings in an infinite hexagonal 2D pattern in the crystallographic ab plane. Some types of clay minerals present isomorphic substitutions in the tetrahedral sheets, where the cation Si^{IV} is replaced by other cations such Al^{3+} or Fe^{3+} thus resulting in negatively charged tetrahedral sheets. The octahedral building blocks comprise a cation M^{n+} (n= 1-3) coordinated to six anions (O^{2-}, OH^- or F^-). These octahedral units are connected to each other by sharing edges, and this results in sheets of hexagonal or pseudo-hexagonal symmetry. The link between the tetrahedral sheet with the octahedral sheet is made through the apical oxygens of the tetrahedra which form a common plane with the octahedral anions [59,55].

The different types of clay minerals are classified to two groups based on the way that these sheets connect to each other, i.e. T:O and T:O:T. The T:O (or 1:1) type is composed of one tetrahedral sheet linked to one octahedral sheet, and the unit cell consists of six octahedral and four tetrahedral cation sites. The T:O:T (or 2:1) type (Figure 14) is formed by one octahedral sheet linked between two tetrahedral sheets, thus presenting a unit cell composed of six octahedral sites and eight tetrahedral sites. The clay minerals are called trioctahedral when all six octahedral sites are occupied, or dioctahedral when only four of the six octahedral cation sites are occupied [59,55].

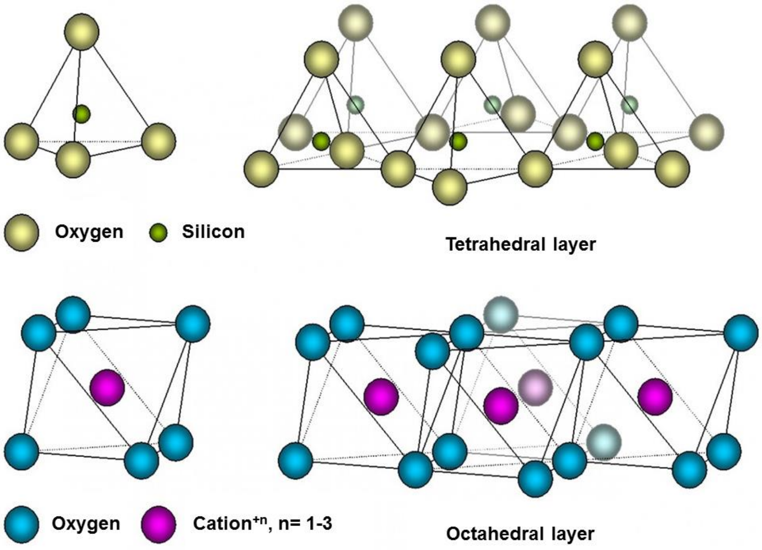

Figure 13. Representation of the tetrahedral and octahedral layers of clay minerals (adapted from [61]).

The T:O type clay minerals have rigid structures with the layers sequentially stacked to each other with a very small interlayer space between them. These clay minerals are thus suitable for e.g. the production of ceramic materials. On the other hand, the T:O:T type materials have a much more flexible structure, because the layers are connected to each other through an interlayer space filled with hydrated cations (Figure 14) in order to compensate the negative charges originating from the aliovalent substitutions. Such negatively charged layers are regarded as one of the most important characteristics of the T:O:T type clay minerals due to the easy cation exchange and high absorption potential of interlayer space. In fact, it is in the interlayer space where the most important technological functionalities of the T:O:T type clay minerals originate from [59].

The T:O:T type clay minerals have several subgroups, e.g., pyrophyllite-talc, smectite, vermiculite, illite, mica, palygorskite-sepiolite, and chlorite [55]. Within these subgroups, the smectites (Figure 14) are the materials with the largest interlayer space among all clay minerals. Smectites have an easily tunable structure which confers several special features such as the following:

- High specific surface area,
- Colloidal sized particles,
- Moderate layer charge ,
- High disorder degree of layer stacking,
- Capacity of anion exchange,
- Capability of intercalating several guest species in the interlayer space,
- Large capacity of cation exchange,
- Variable interlayer space, and
- Ability of having an extensive interlayer swelling in water, which can result into the delamination of the layers under optimum conditions [59].

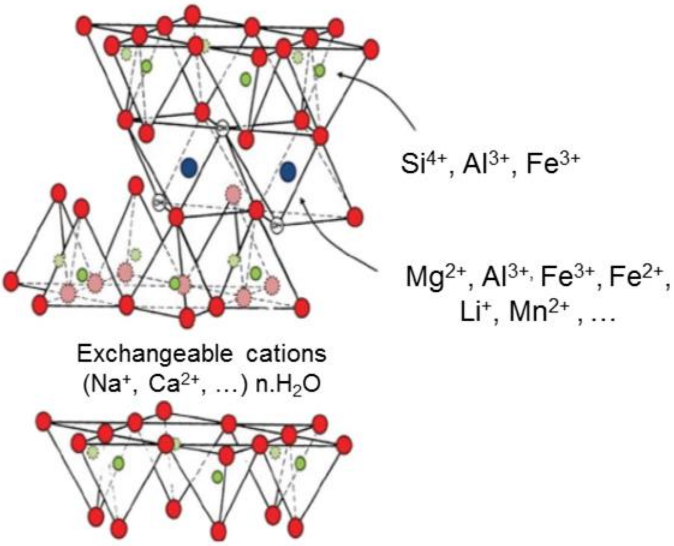

Figure 14. The ideal T:O.T crystal structure of smectites (adapted from [62]).

The smectites are abundant in nature, but their composition varies and several impurities will always be present. When the aimed application does not require a homogeneous composition, purification processes can be used to remove the impurities. However, if the homogeneity of the composition matters for the further application, the pure phase can only be produced through a controllable synthesis, allowing to control the substitutions [60]. All types of smectites (Table 1) can be synthesized, but most of them have slow crystallization kinetics and thus they require a long time for synthesis (ca. 72 h). However, hectorites form rather easily at low temperatures and pressures (ca. 24h at around 100 °C and 100 kPa) [9]. Therefore, hectorites, together with saponites, are also the most common authigenic clay minerals. Because of the easy synthesis, the materials discussed in the current thesis were synthesized based on the hectorite structure.

Table 1. The most important smectite type clay minerals [59].

Smectite species:	**Nature of the octahedral sheet:**	**General composition:**
Montmorillonite	dioctahedral	$(M_y^+ . nH_2O)(Al_{2-y}^{3} Mg_y^{2+}) Si_4^{4+} O_{10}(OH)_2$
Beidellite		$(M_x^+ . nH_2O) Al_2^{3+} (Si_{4-x}^{4+} Al_x^{3+}) O_{10}(OH)_2$
Nontronite		$(M_x^+ . nH_2O) Fe_2^{3+} (Si_{4-x}^{4+} Al_x^{3+}) O_{10}(OH)_2$
Volkonskoite		$(M_x^+ . nH_2O) Cr_2^{3+} (Si_{4-x}^{4+} Al_x^{3+}) O_{10}(OH)_2$
Hectorite	trioctahedral	$(M_y^+ . nH_2O)(Mg_{3-y}^{2+} Li_y^+) Si_4^{4+} O_{10}(OH)_2$
Saponite		$(M_x^+ . nH_2O) Mg_3^{2+} (Si_{4-x}^{4+} Al_x^{3+}) O_{10}(OH)_2$
Sauconite		$(M_x^+ . nH_2O) Zn_3^{2+} (Si_{4-x}^{4+} Al_x^{3+}) O_{10}(OH)_2$

2.6.1. Structure, features and applications of synthetic hectorites

Hectorite with the common chemical formula $Na_{0.3}(Mg,Li)_3Si_4O_{10}(OH)_2$ has its name derived from Hector, California, USA, which is the location of the first finding of this clay mineral. It presents a perfect {001} cleavage, uneven fracture and hardness of ca. 1-2, as well as a body color ranging from white to brown [63]. The crystal structure is monoclinic with space group C2/m (No. 12). For hydrated sodium fluorohectorite with two water layers, the unit cell parameters have been reported as a = 5.2432(10), b = 9.0870(18), c = 15.064(3) Å and $\beta = 96.42(3)^o$ with Z = 2 based on single-crystal X-ray diffraction [64]. The basic structure comprises distorted SiO_4 tetrahedra and distorted $(Mg,Li)O_4F_2$ octahedra. The interlayer space contains distorted $Na(O_w)_6$ octahedra (O_w: oxygen from water molecule). The structural details are shown in Table 2.

As a characteristic feature of smectites, the hectorites have a large interlayer space which can be extended through the insertion of large guest groups. Thus, typical interlayer spaces vary from 10 to 20 Å, but it is possible to extend up to 40 Å [9,55]. Moreover, hectorite suspensions show high transparency and viscosity as well as other attractive rheological features which enable the usage of these materials in several applications, mainly as a host or matrix in different systems [9]. The first synthetic method of hectorites at low temperatures was presented in the 1940s [65], and after that several other methods have been presented in the literature. These include hydrothermal crystallization, electrolytic attack, co-precipitation, sol-gel aging and microwave-hydrothermal treatment [9,66]. Among the methods, the hydrothermal crystallization is one of the most feasible methods, requiring only such equipment (a reflux system) and precursors (e.g. LiF, $Mg(OH)_2$, SiO_2 and NH_4OH) that are commonly found in chemical laboratories [9,67]. Synthetic hectorites are also produced in large industrial scale, and sold under the commercial patented name of Laponite® [68].

Table 2. Structural data for sodium fluorohectorite [64].

Atom	**Site**	**Symmetry**	**x**	**y**	**z**	**Occupancy**
Na	4h	C$_2$	1/2	0.3318(12)	1/2	0.35
Mg1	2a	C$_{2h}$	0	0	0	0.703(3)
Li1	2a	C$_{2h}$	0	0	0	0.297(3)
Mg2	4g	C$_2$	0	0.33361(14)	0	0.767(2)
Li2	4g	C$_2$	0	0.33361(14)	0	0.233(3)
Si	8j	C$_1$	0.10636(15)	0.16707(7)	0.81766(6)	1
O1	8j	C$_1$	0.1413(3)	0.16780(17)	0.92345(13)	1
O5	8j	C$_1$	0.3413(3)	0.24843(18)	0.77487(13)	1
F	4i	C$_s$	-0.3542(4)	0	0.93276(15)	1
O3	4i	C$_s$	0.0852(5)	0	0.77472(18)	1
O$_w$1	4i	C$_s$	-0.210(4)	0	0.5880(9)	1
O$_w$2	8j	C$_1$	-0.134(3)	0.353(2)	0.5917(7)	0.50
Bond		**Length / Å**	**Bond**	**Length / Å**	**Bond**	**Length / Å**
Na-O$_w$2 x2		2.244	Mg1/Li1-F x2	2.014	Si-O1	1.584
Na-O$_w$2 x2		2.332	Mg1/Li1-O1 x4	2.096	Si-O5	1.630
Na-O$_w$1 x2		2.373	Mg2/Li2-F x2	2.017	Si-O3	1.649
			Mg2/Li2-O1 x2	2.083	Si-O5	1.654
			Mg2/Li2-O1 x2	2.093		

The synthetic hectorites are the subject of many studies not only because of its easy synthesis, but also because they represent a complex colloidal system with a rich phase diagram comprising fluid, gel and glassy states [68,69]. The nanomaterials obtained from synthetic hectorites have been proven to be more advantageous than the respective materials derived from natural hectorites, since the synthetic materials can be obtained with much less structural defects. Furthermore, the easy synthesis of hectorite allows the design of its structure according to the aimed application [66,68]. That is why hectorites are also attractive materials to act as host matrices for optically active species [70,71].

There are several variations of the hectorite composition. Among these variations, the most common one is $Na_{0.7}(Si_8Mg_{5.5}Li_{0.3})O_{20}(OH)_4$ [69,72]. However, when luminescence applications are aimed, the rather high energy phonons of the hydroxyl groups (3500 cm^{-1}) may lead to luminescence quenching due to multiphonon de-excitation [5]. Since the X-Hec materials presented in the current thesis were produced aiming their use as hosts lattices for optically active species (generating luminescent materials), they were synthesized based on the hectorite structure, but by replacing the OH^- ions by halogens (X= F, Cl, Br, and I) obtaining the F-Hec [I, III], Cl-Hec [II, III], Br-Hec [IV], and I-Hec [IV] materials (Figure 19). Before the present work, Cl-Hec, Br-Hec and I-Hec had not been reported in the literature.

Regarding to the popularity of clay minerals materials with luminescence properties, the literature reports luminescence for non-doped clay minerals. For instance, kaolinite ($Al_2Si_2O_5(OH)_4$) which is a T:O type of clay mineral [73–80], or montmorillonite (T:O:T type, belonging to the smectite group) ($(Na,Ca)_{0.33}(Al,Mg)_2(Si_4O_{10})(OH)_2.nH_2O$) [81–84] have been explored in luminescence studies as such (i.e. without doping). For these materials, red and blue emission bands have been reported. The Figure 15 shows examples of these emissions in the photoluminescence spectra (λ_{exc}: 400 nm, T = 4.2 K) of pure montmorillonite and one modified with cetyltrimethylammonium bromide (CTAB) (Figure 15 (a) [84]), as well as in the cathodoluminescence spectra of two kaolinites with different origins (Figure 15 (b) [80]). However, in these cases the origin of the emission was left unresolved. Sometimes, as mentioned above (Section 2.5.3), for halloysite the two-fold coordinated silicon centers have been suggested as the cause of emission [54]. Broader discussion about this topic is presented in section 5.4 of the current thesis.

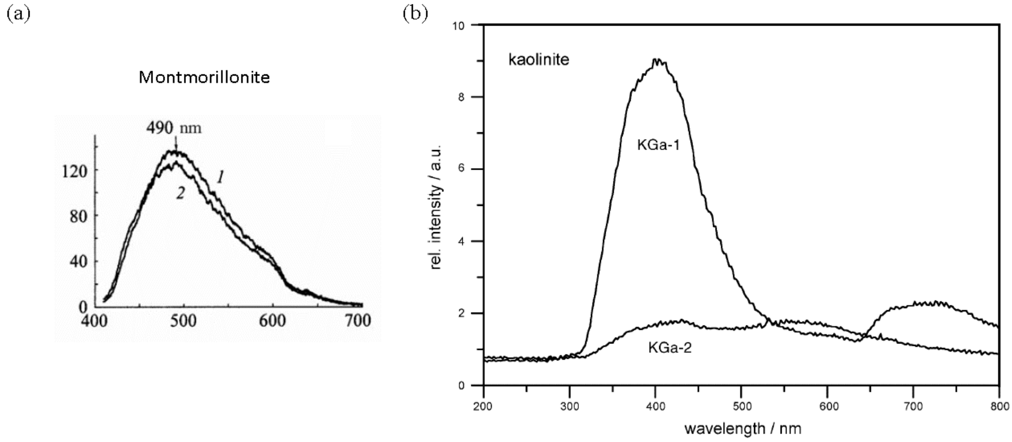

Figure 15. (a) The photoluminescence spectra (λ_{exc}: 400 nm, T = 4.2 K) of montmorillonite pure (1) and modified with CTAB (2) [84]; and (b) The cathodoluminescence spectra of two different samples of kaolinite: KGa-1 extracted at Washington, USA; and KGa-2 extracted from Warren, USA [80].

The literature reports the construction of luminescent materials by doping synthetic hectorites with organic complexes of Eu^{3+} [6,85,86], Tb^{3+} [86], or $PbF_2:Yb^{3+},Er^{3+}$ [87]. Some examples of luminescence spectra of successful materials obtained from the doping of synthetic hectorites with Eu^{3+} or Tb^{3+} complexes are shown in the Figure 16. Figure 16 (a and b) shows the excitation and emission spectra of a complex of Tb^{3+} and an aromatic carboxyl-functionalized organic salt (Bu-IL-ACC-Tb), and the hybrid material resulting from the intercalation of laponite (synthetic hectorite) with the Bu-IL-ACC-Tb complex [86]. Figure 16 (c) shows the excitation and emission spectra of hybrid materials obtained though the intercalation of hectorite and montmorillonite with an europium (III) complex ($[EuCl_2(Phen)_2(H_2O)_2]Cl.H_2O$) [6]. These luminescent materials have been employed in different applications, such as the production of highly photo- and thermo-stable nanocomposites [85,86], photon up-conversion [87], and enhanced latent fingerprint detection [6]. However, only one work has reported luminescent materials obtained by doping a synthetic hectorite through exchange reaction, but then the mineral structure of the hectorite was collapsed into enstatite ($MgSiO_3$) to yield the luminescent material [8]. In all other reports of this nature, the RE^{3+} ions were incorporated into the hectorite structure as intercalated metal-organic complexes, using the organic molecules as “antennas” to enhance the radiation absorption, and thus, also the luminescence emission. In the present thesis work, the direct doping of hectorites with Eu^{3+} and Tb^{3+} ions was reported for the first time. The results are discussed in section 5.6.

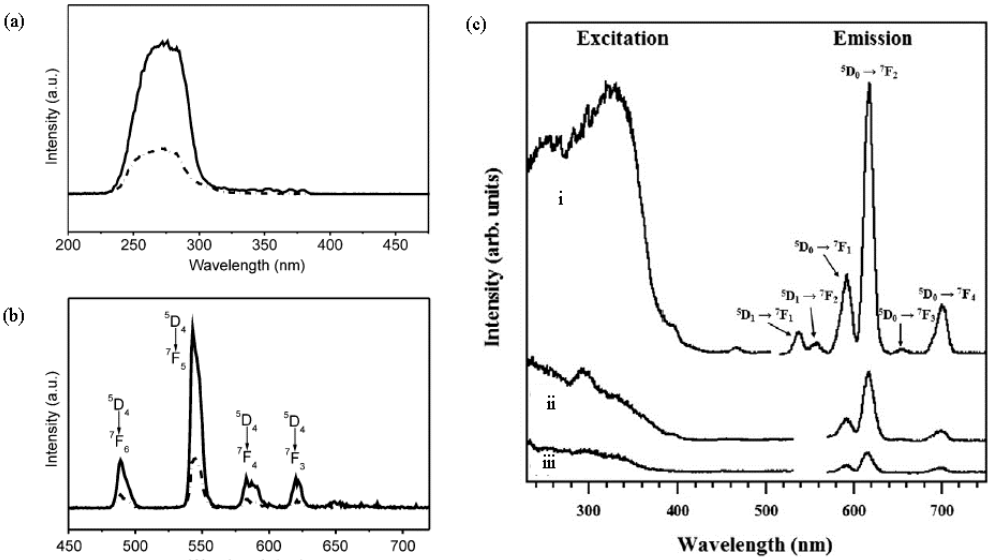

Figure 16. (a) The excitation (λ_{em}: 544 nm), and (b) the emission spectra (λ_{exc}: 280 nm) of the Tb^{3+} complex Bu-IL-ACC-Tb (solid line) and laponite-Tb (dotted line) [86]. (c) The emission (λ_{exc}: 328 nm) and excitation (λ_{em}: 617 nm) spectra of (i) Eu(III) complex, (ii) $[Eu(Phen)_2]^{3+}$-laponite hybrid, and (iii) $[Eu(Phen)_2]^{3+}$-montmorillonite hybrid [6].

3. Materials and Methods

3.1. Synthesis of the halogen-hectorites (X-Hec)

The X-Hec were synthesized using a hydrothermal crystallization method [67] with stoichiometric amounts of the reagents (except for a threefold excess of the respective sodium halogenate salt used in each synthesis) in a reflux system at 100 °C. The precursors used in the synthesis of each X-Hec are listed in the Table 3. The respective colloidal mixtures were kept in the reflux system for 24 h. After ceasing the reflux, all materials were vacuum filtered and washed with deionized water several times, until total extinction of the excess of halogen ions in the filtrate liquid was reached (checked with the silver nitrate test). Subsequently, all X-Hec materials were dried for 12 h at 200 °C [I-IV]. Samples of the F-Hec and Cl-Hec materials were also dried for 30 min at 600 °C for characterization.

Table 3. Precursors used in the synthesis of each X-Hec material [I-IV].

X-Hec	Precursors:	Medium:
F-Hec [I-III]	LiF (≥ 99.98 %, Sigma-Aldrich, USA), NaF (≥ 99 %, J.T. Baker, USA), MgO (≥ 97 %, Merck, DE) and SiO_2 (≥ 99.8 %, Sigma-Aldrich, USA).	Deionized water (neutral) or 0.01 mmoldm^{-3} solution of NaOH (basic, pH= 12)
Cl-Hec [II-III]	$LiClO_4$ (≥ 99.99 %, Sigma-Aldrich, USA), NaCl (≥ 99.5 %, J.T. Baker, USA), MgO (≥ 97 %, Merck, DE) and SiO_2 (≥ 99.8 %, Sigma-Aldrich, USA)	Deionized water (neutral) or 0.01 mmoldm^{-3} solution of NaOH (basic, pH= 12)
Br-Hec [IV]	LiBr (≥ 99 %, Sigma-Aldrich, USA), NaBr (≥ 99 %, J.T. Baker, USA), MgO (≥ 97 %, Merck, DE) and SiO_2 (≥ 99.8 %, Sigma-Aldrich, USA).	Deionized water (neutral)
I-Hec [IV]	LiI (≥ 99.9 %, Fluka AG, CH), NaI (≥ 99.5 %, Merck, DE), MgO (≥ 97 %, Merck, DE) and SiO_2 (≥ 99.8 %, Sigma-Aldrich, USA).	Deionized water (neutral)

3.1.1. Doping of the neutral Cl-Hec with Ti^{3+}

The neutral Cl-Hec material was doped with Ti^{3+} in three steps. First, five homogeneous colloidal suspensions were generated by adding 0.1 g of neutral Cl-Hec into deionized water (10 cm^3), while continuously stirring and heating (30 min @ 50 °C). Then, stoichiometric amounts of a 0.1 $moldm^{-3}$ aqueous solution of $TiCl_3$ (solution about 15% of $TiCl_3$ in about 10 % of hydrochloric acid, Merck, DE) was added to these suspensions to obtain 0.1, 0.5, 1.0, 1.5 and 2.0 mol-% of Ti^{3+} (relative to the Na^+ amount in the interlayer space). The suspensions were stirred and heated (3 h @ 200 °C) and then vacuum filtered and dried (12 h @ 200 °C) [II].

3.1.2. Doping of the F-Hec and Cl-Hec with Eu^{3+} and/or Tb^{3+}

The neutral and basic F-Hec and Cl-Hec materials were doped with Eu^{3+} and/or Tb^{3+} to obtain the X-Hec:Eu^{3+}, X-Hec:Tb^{3+} and X-Hec:Eu^{3+},Tb^{3+} materials in both neutral and basic conditions. The sol-gel method of cation-exchange was used to achieve the doping in the X-Hec structure. The same three steps described previously for the Ti^{3+} doping were followed for all Eu^{3+} and/or Tb^{3+} doped materials: i) the homogeneous colloidal suspensions were generated by adding 0.1 g of X-Hec into deionized water (10 cm^3), while continuously stirring and heating (30 min @ 50 °C); ii) stoichiometric amounts of 0.01 $moldm^{-3}$ aqueous solution of $EuCl_3.6H_2O$ (≥ 99.9%, Sigma-Aldrich, USA) and/or $TbCl_3.6H_2O$ (≥ 99.9%, Sigma-Aldrich, USA) were added to the suspensions to obtain 0.02 mol-% of Eu^{3+} and/or Tb^{3+} (relative to the Na^+ amount in the interlayer space); and iii) the suspensions were stirred and heated (3 h @ 200 °C) and then vacuum filtrated and dried (12 h @ 200 °C) [III].

3.2. Reference Material

The purified natural hectorite sample was obtained from Newberry Hectorite Mine (San Bernardino, California, USA) [II].

3.3. Characterization

3.3.1. Studies of phase purity

The crystal structure and phase purity of the doped and non-doped X-Hec were verified with routine room temperature (RT) X-ray powder diffraction (XPD) measurements using a Huber G670 Guinier camera with an image plate detector and $CuK_{\alpha 1}$ radiation (λ = 1.54060 Å). The crystallite size was calculated using the Scherrer formula (Eqs. 2 and 3):

$$D = 0.9\lambda/\beta cos\theta \tag{2}$$

$$\beta^2 = \beta_s^2 - \beta_r^2 \tag{3}$$

Where D (nm) is the average size of the crystallites, λ (Å) the X-ray wavelength, β (rad) the full width at half maximum (FWHM) of the (001) reflection and θ (°) half of the Bragg's angle (2θ) [88]. The reflection broadening (β_r) due to the diffractometer set-up was eliminated from the β_s–value by using a microcrystalline Si (NIST SRM 640d) reference [I-IV].

3.3.2. Chemical studies

The chemical bonds formed at the molecular level of all non-doped X-Hec materials were studied with Fourier Transform Infrared Spectroscopy (FTIR) measurements. The spectra were determined at RT in the range of 400 – 4000 cm^{-1} by using a Bruker Vertex 70 spectrometer, equipped with a RT-DLaTGS detector, and a VideoMVP^{TM} Diamond accessory. Each spectrum was measured co-adding a total of 320 interferograms, with a resolution of 4 cm^{-1}. The usage of the diamond as an internal reflection element in the ATR method (attenuated total reflection) has as limitation the occurrence of an intrinsic absorption in the spectral range of 2300 to 1800 cm^{-1}, which limits its usefulness in this region (presenting only 5% of transmission in this range) [I - IV].

The chemical composition and impurities of the non-doped X-Hec and Cl-Hec:Ti^{3+} materials were investigated with the X-ray fluorescence (XRF) measurements. The XRF spectra were obtained with a Panalytical Epsilon 1 apparatus using AgK_{α} radiation (E = 22.16 keV) and a high-resolution Si drift detector (with a typical energy resolution of 135 eV @ 5.9 keV / 1000 cps) [I, II and IV]. The determination of the Ti, Fe, Mn and Cr concentrations was made for the neutral Cl-Hec, with an Inductively Coupled Plasma Mass Spectroscopy (ICP-MS) instrument, PerkinElmer 6100 DRC Plus (Toronto, Canada), in quantitative mode [II].

The chemical environment around the Si^{IV} cations of the non-doped X-Hec materials was studied with solid-state ^{29}Si MAS NMR spectroscopy. The spectra were recorded for 24 h at RT with a Bruker AV400 spectrometer using a 10000 Hz spinning rate and a 60 s relaxation time. The parts per million scale was calibrated against tetramethylsilane (TMS) at 0.00 ppm, designated by the equipment [III, IV].

The valence of titanium was probed with X-ray photoelectron spectroscopy (XPS) measurements carried out using a Perkin-Elmer PHI 5400 spectrometer with a MgK_{α} X-ray source (E = 1.25 keV) and a hemispherical electron energy analyser. The Cl-Hec:Ti^{3+} (2 mol-%) was analysed with a scanning step of 0.1 eV and pass-energy of 17.9 eV, by using 14.0 kV as the accelerating voltage in the Mg-anode. The curve fitting was carried out using Origin 2015 software (OriginLab, Northampton, USA) [II].

3.3.3. Studies of the physical properties

The morphology of the non-doped F-Hec and Cl-Hec materials was analyzed from the images obtained by a JEOL JSM-6701 F field emission scanning transmission electron microscope (STEM) operating at low voltage (30 kV). The samples were diluted in acetone for the analyses [II].

The specific surface area and porosity of the non-doped X-Hec materials were determined by nitrogen sorption at 77 K, recorded in triplicate with a TriStar 3000 apparatus (Micromeritics Inc., USA). The surface area was calculated with the Brunauer-Emmett-Teller (BET) method [89]. The volume of the mesopores was estimated by using the total adsorbed amount at a relative pressure $p/p^0 = 0.97$ [90] [III, IV].

The thermal stability of the host lattices was investigated with a TA Instruments SDT Q600 simultaneous TGA-DSC apparatus by heating ca. 20 mg of each material from 25 to 1000 °C in flowing N_2 (rate flow: 100 cm^3min^{-1}, heating rate: 10 $°Cmin^{-1}$). An empty aluminum oxide sample cup was used as the reference material and similar cups were used as sample pans [III, IV].

3.3.4. Studies of optical properties

The photoluminescence emission and excitation spectra as well as the luminescence decay curves of all doped and non-doped X-Hec materials were measured at RT with a Varian Cary Eclipse Spectrophotometer having a 150 W Xe lamp as the excitation source [I-IV]. The visual appearance of the non-doped and Eu^{3+} and/or Tb^{3+} doped X-Hec materials was registered with photos obtained by using a Canon EOS 60 D camera (18 Megapixel resolution and 5.3 fps shooting speed) [I-IV]. The reflectance spectra of all X-Hec materials were measured under white light (a commercial 60 W incandescent lamp) using a CCD detector (Avantes SensLine, Model AvaSpec-HS-Tec).

The thermoluminescence (TL) measurements were made for the non-doped X-Hec materials with a MikroLab Thermoluminescent Materials Laboratory Reader RA'04 using a heating rate of 10 °Cs^{-1}. Before the measurements, the samples were irradiated for 5 min at RT with a 4 W UVGL-25 UV lamp at 254 nm. After turning off the irradiation, there was a delay of 5 s before the start of the measurement. The TL glow curves were measured in a range of 40 to 400 °C. Estimations of the trap energies were obtained with the initial rise method: $lnI = C - E_t/kT$, where I is the TL intensity, C is a constant including the frequency factor, E_t is the trap depth (activation energy), k Boltzmann constant and T temperature (in K) [91] [II].

4. Results and Discussion

4.1. Structure and purity

4.1.1. Phase purity of the non-doped X-Hec materials

According to the XPD measurements of the non-doped X-Hec materials (Figure 17), all of them have the hexagonal fluorohectorite structure at nanodimensions. The patterns indicate that no crystalline impurities are present. The reflections in the XPD patterns are regularly so broad that it is impossible to determine the reflection FWHMs accurately due to their extensive overlap. However, the reflection at ca. 6.2° (in 2θ) is the isolated (001) one which allows carrying out the Scherrer calculations for determining the diffracting domain size. The size along that 001 direction was estimated to be ca. 3 nm for all X-Hec materials [I-IV]. The (00l) reflections are wider than the others meaning that the crystallites are larger in the other directions as an indication of plate-like morphology, which is expected due to the layered structure of hectorite-type of clay minerals. In the XPD patterns, each material displays the d_{001} value of ca. 14.3 Å, which falls in the center of the range typical of basal spacings in smectites, *i.e.* 10 – 20 Å [55]. This basal spacing indicates that the interlayer spacing along the unit cell c axis is ca. 6.3 Å. Such a large spacing offers good host features for these X-Hec materials ensuring their high potential for cation exchange and adsorption [I-IV].

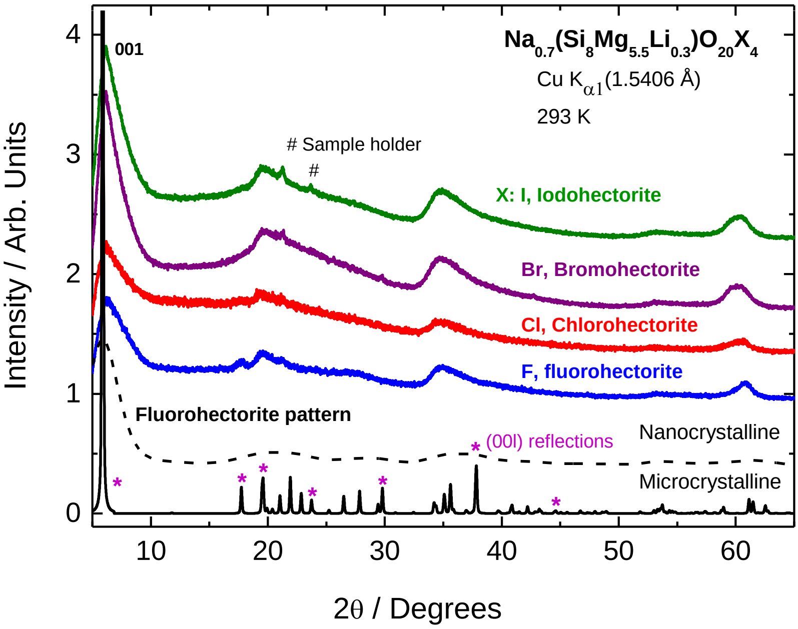

Figure 17. The XPD patterns of the neutral non-doped X-Hec materials. The reference patterns for nano- and microcrystalline fluorohectorite were calculated with the PowderCell v 2.4 program (W. Kraus and G. Nolze, BAM, Berlin, Germany, 2000) using structural data from[64] [I-IV].

The synthesis of F-Hec and Cl-Hec in basic medium did not alter the formation of the hectorite-like structure for the materials. The XPD patterns indicated that the basic F-Hec and Cl-Hec (Figure 18) kept the analogous crystal structure of the respective materials synthesized in neutral medium, with similar domain size along the 00l direction (ca. 3 nm) and no variation in the position of the peak associated with the 001 reflection. Figure 19 shows a view of the X-Hec structure which contains two continuous T:O:T sheets linked by an interlayer space (composed by hydrated Na^+) in each unit cell. In the X-Hec materials, the octahedral cations may be Li^+ or Mg^{2+} coordinated to four O^{2-} and two X^- (X: F, Cl, Br or I), where two different topologies can be related to the halogen position, i.e. the cis- or trans-orientation [59].

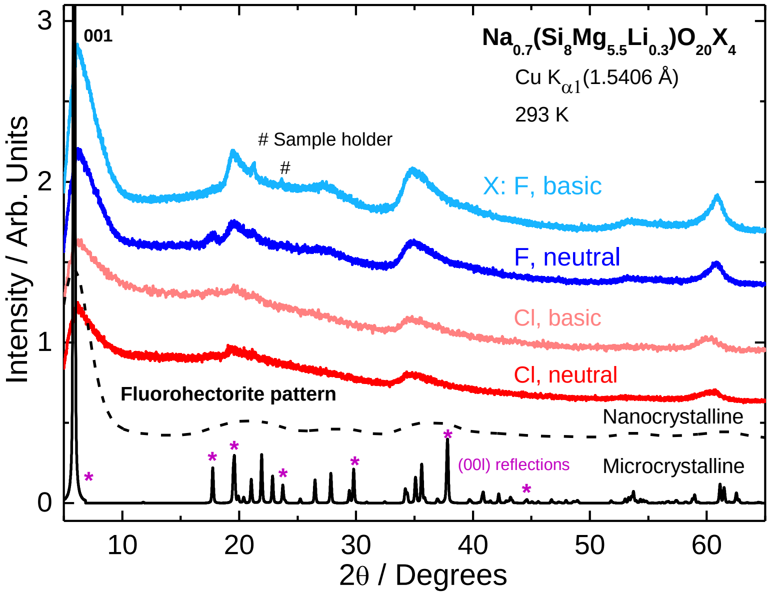

Figure 18. The XPD patterns of the neutral and basic F-Hec and Cl-Hec materials. The reference patterns for nano- and microcrystalline fluorohectorite were calculated with the PowderCell v 2.4 program (W. Kraus and G. Nolze, BAM, Berlin, Germany, 2000) using structural data from[64][I-III].

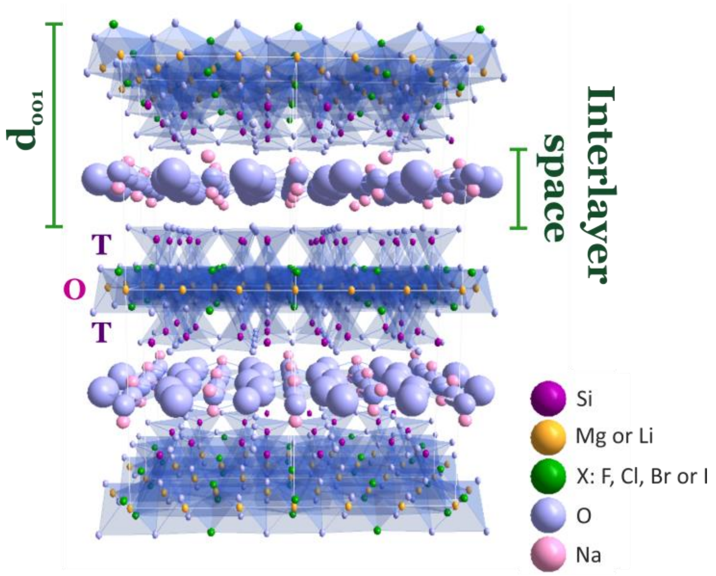

Figure 19. A Diamond 3.2 (Crystal Impact, Bonn, Germany) view of the T:O:T clay structure (based on fluorohectorite structural data from [64]). Adapted from [II].

4.1.2. Phase purity of the X-Hec materials doped with Ti^{3+}, Eu^{3+} and/or Tb^{3+}

Doping the neutral Cl-Hec material with Ti^{3+} at different concentrations (x_{Ti} mol-%: 0.1 to 2.0) did not induce significant changes either in its crystal structure or the formation of crystalline impurities (Figure S1 [II]). However, the XPD patterns indicate that the cation exchange have induced an additional reflection at 17.7°. The origin of this signal is unknown, but it may indicate small distortions along the 020 (or 110) crystal direction. Regardless of this unknown signal, the XPD patterns of the Cl-Hec:Ti^{3+} materials indicate the hexagonal crystal structure of fluorohectorite at nanodimensions.

The XPD patterns of the F-Hec and Cl-Hec materials doped with Eu^{3+} and/or Tb^{3+} (Figure 20) also indicate a successful cation exchange reaction promoted by the doping, without the crystallization of impurities or changes in the crystal structure of the host matrices. Here, the additional reflection is observed only for the doped Cl-Hec materials. Still, all doped materials had maintained the initial crystal structure even after doping.

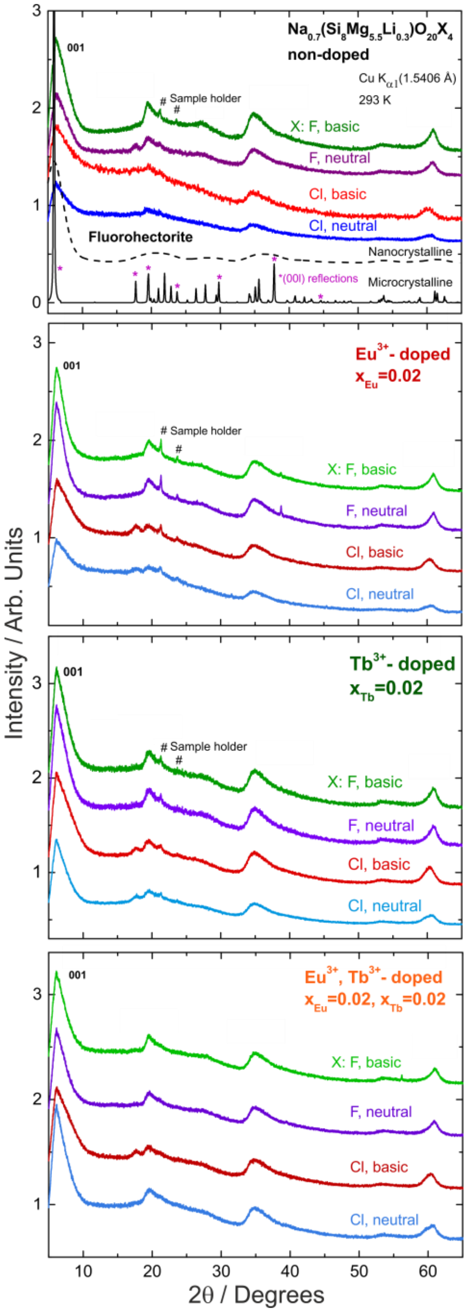

Figure 20. The XPD patterns of the F-Hec and Cl-Hec materials doped with Eu^{3+} and/or Tb^{3+}. The reference patterns for nano- and microcrystalline fluorohectorite were calculated with the PowderCell v 2.4 program (W. Kraus and G. Nolze, BAM, Berlin, Germany, 2000) using structural data from [64] [III].

4.2. Chemical environment

4.2.1. FTIR measurements

The FTIR measurements (Figure 21) indicate that there are no structural hydroxyl groups in the octahedral layers of all non-doped X-Hec materials. This is evidenced by the absence of strong and sharp bands in the region of 3600 to 3700 cm^{-1}, related to the stretching mode of hydroxyl groups coordinated to octahedral Li or Mg [92,93]. This indicates the total formation of the octahedral units with the respective halogens ligands, instead of the common hydroxyl groups. A low content of hydrated water in the interlayer space of the clays is evidenced by the broad band in the region of 3200 to 3400 cm^{-1} and a weak band at ca. 1625 cm^{-1}, which are due to H-O-H stretching and deformation of the hydration water molecule, respectively [92]. These bands related with the H-O-H vibrational modes are more prominent for the F-Hec and Cl-Hec materials indicating higher contents of hydrated water for these two materials. In the fingerprint region of the spectra, vibrational bands were observed at 1010-1090, 800 and 660 cm^{-1}. They are assigned to asymmetric stretching, symmetric stretching and bending modes of Si-O-Si, respectively, as reported for the tetrahedral and octahedral layers of ordered hectorite clay minerals [66,93]. Moreover, the absence of a weak band at 1200 cm^{-1} indicates the absence or low concentration of amorphous silica [66] in all neutral X-Hec materials. Finally, the FTIR spectra of all X-Hec show the band at 460 cm^{-1} associated with the asymmetric stretching of Mg-O in the octahedral units of the clay materials normally identified for hectorites [93] [I-IV].

The F-Hec and Cl-Hec synthesized in basic medium have analogous FTIR spectra to the respective neutral materials (Figure 21) indicating that the basicity of the medium does not promote significant changes in the reaction process and that the same expected final product is obtained. The FTIR spectra of the basic Cl-Hec material show more pronouncedly the bands related to the H-O-H stretching (3200 to 3400 cm^{-1}) [92] than the F-Hec materials, which may be due to higher water contents in this material. Moreover, a moderate heating treatment (30 min @ 600 °C) induces the loss of these weak bands related to H-O-H bending and stretching modes (Figure 22), which reappear in the spectra with increasing exposure time to atmospheric air (Figures S8 to S11 [III]), showing that these bands are due to the high hydrophilic character of the X-Hec materials. All in all, each one of the X-Hec materials synthesized possessed the expected chemical structure [III].

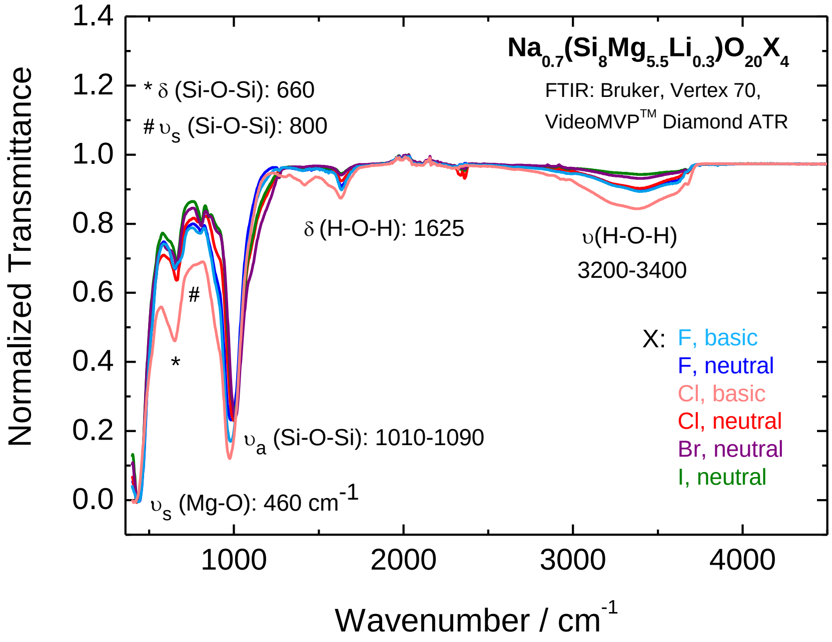

Figure 21. FTIR spectra of the non-doped X-Hec materials [I-IV].

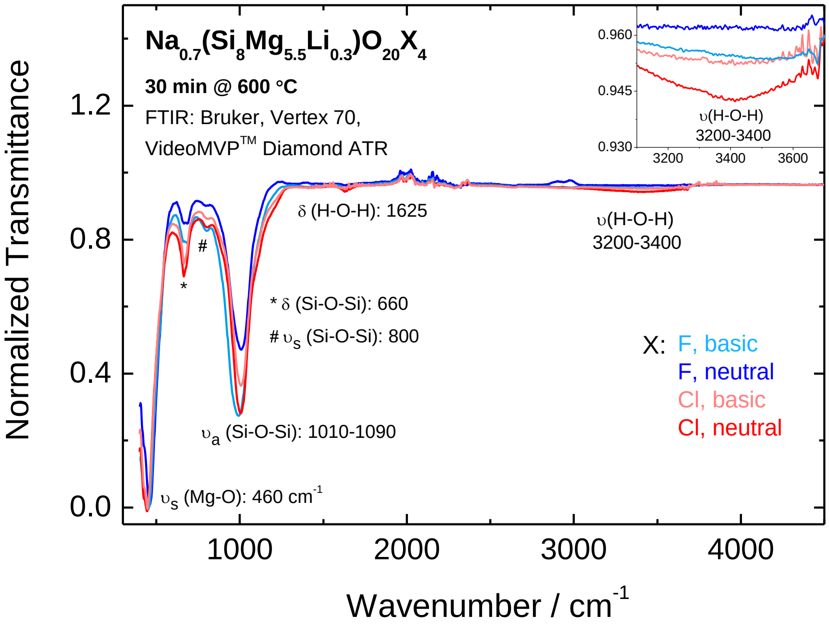

Figure 22. FTIR spectra of the F-Hec and Cl-Hec materials synthesized in neutral and basic medium, after heating treatment (30 min @ 600 °C). The insert shows the loss of the hydrated water signal after heating [III].

4.2.2. ^{29}Si MAS NMR measurements

The chemical environment provided by a host lattice has a crucial importance for the performance of a luminescent material. Since the X-Hec materials are nanocrystalline, the XPD cannot give detailed information of the host lattice structure. Thus, the ^{29}Si MAS NMR spectra were recorded to examine the polymerization of the orthosilicate ions present in the tetrahedral sheets of the X-Hec materials. The usual nomenclature expresses the degree of polymerization as Q^n, representing the silicate tetrahedron having n shared oxygen atoms ($0 \leq n \leq 4$) [94,95]. The chemical shifts of silicate tetrahedra are normally identified from -60 to -140 ppm. However, the increase of polymerization of the Q^n building units generates a characteristic up-field shift to lower frequency, thus Q^4 must have lower chemical shifts than Q^{4-i} $\{i \in Z/[1,4]\}$ [95]. For silicon frameworks, it is expected that mainly two peaks can be identified in the ^{29}Si MAS NMR spectra: those associated with the Q^2 ($Si(OSi)_2(OH)_2$) and Q^3 ($Si(OSi)_3OH$) signals (in higher intensity than Q^2 peak) and observed from -74 to -92 ppm, and -93 to -101 ppm, respectively [95–99]. For synthetic hectorites, an additional peak corresponding to Q^4 ($Si(OSi)_4$) signal has been observed around -103 to -120 ppm. This represents the centers in the developing silica framework, *i.e.* some silica excess present in the material [96–99] [III].

The ^{29}Si NMR spectra of all X-Hec materials (Figure 3 [III] and Figure 4 [IV]) show that the built silicon frameworks have the same chemical environment predicted for the tetrahedral layers of synthetic hectorites. Table 2 shows the ^{29}Si chemical shifts identified for each X-Hec material. The most intense resonance signal is assigned to the Q^3 sites of the $Si(OMg)(OSi)_3$ type which is identified at -95 ppm for synthetic hectorite [100]. However it is observed at lower chemical shifts for the X-Hec materials (-113 to -96 ppm) due to the differences in electronegativity caused by the halogen ions in the surroundings of the Si sites [101]. The spectra of all X-Hec materials also show the signal related to Q^2 which is found at -85 ppm for synthetic hectorites [100] and it is observed at lower chemical shifts for the X-Hec materials (-98 to -87 ppm) because of the electronegativity effect [101]. Moreover, the X-Hec materials (except for the F-Hec) have a weak signal associated to Q^4 which is normally identified at -107 ppm for synthetic hectorites [100]. Also this signal is shifted to lower ppm values in the X-Hec materials (-129 to -111 ppm). All three Q^n signals identified for the X-Hec materials follow a general trend of decreasing the chemical shift with increasing of electronegativity as expected [101]. However the Q^3 signals of the F-Hec materials do not follow the trend, but the reason for this is still unclear.

The polymerization degree of the X-Hec materials was qualitatively evaluated through the ratios between the intensities of the Q^2 and Q^3 signals (Q^2/Q^3), which is a common tool to determine the extension of branching relative to the extension of the orthosilicate chains [95]. According to the obtained ratios (Table 4) the degree of branching in the tetrahedral sheets of the X-Hec materials increases in the following order: F-Hec, basic < F-Hec, neutral < Cl-Hec, basic < Br-Hec < I-Hec < Cl-Hec, neutral. Therefore, there is a trend of increasing the degree of branching with the increase of the ionic radius of the halogens, except for the neutral Cl-Hec materials which does not follow this trend.

Table 4. The ^{29}Si chemical shifts identified in NMR spectra of the X-Hec materials [III, IV].

X-Hec, X:	^{29}Si chemical shifts (ppm)			Ratio Q^2/Q^3
	Q^2	Q^3	Q^4	
F, neutral	-98	-107	-	0.24
F, basic	-98	-107	-	0.23
Cl, neutral	-98	-109	-125	0.43
Cl, basic	-102	-113	-129	0.36
Br, neutral	-87	-98	-111	0.37
I, neutral	-87	-96	-111	0.41

4.2.3. Elemental composition: XRF and ICP-MS measurements

The total XRF spectra of the X-Hec materials confirmed the presence of the expected elements of the synthesized materials (Figure 3 [I], Figure S4 [II] and Figure 2 [IV]. All spectra show the lines assigned to the Mg $K_{\alpha 1}$, Si $K_{\alpha 1}$ and Ca $K_{\alpha 2}$ emissions at 1.25, 1.74 and 3.69 keV, respectively [102], where the presence of calcium may be associated to its common presence as impurity in the sodium halide precursors used in the synthesis. Thus, the presence of hydrated Ca^{2+} and Na^+ cations is expected in the interlayer space of the X-Hec materials with sodium being the expected majority. Moreover, the respective halogens of the X-Hec materials were also identified in the XRF spectra (except from fluorine, which is out of the detection range of the equipment), confirming the halogen contents in the composition of the materials. The spectra of the Cl-Hec materials have the line of $ClK_{\alpha1}$ emission at 2.62 keV [102] (Figure S4 [II]). The spectrum of the Br-Hec presents the line of Br $L_{\alpha1,2}$ emission at 1.48 keV [102] (Figure 2 [IV]). Finally, the iodine contents on the composition of the I-Hec is confirmed by the emission lines of I $L_{\alpha1}$, $L_{\beta1}$ and $L_{\beta2}$ at 3.94, 4.22 and 4.51 keV, respectively [102] (Figure 2 [IV]) [I, II, IV].

The XRF spectra of all X-Hec materials show the Ti emission lines confirming its presence as impurity in the X-Hec compositions (Figure 23). The Ti was identified through three signals at 4.50, 4.51 and 4.9 keV, assigned to its respective $K_{\alpha1}$, $K_{\alpha2}$, $K_{\beta1}$ emissions [102]. All materials present these three signals with weak intensity [I, II, IV].

To estimate the concentration of titanium as an impurity in the X-Hec materials, the neutral Cl-Hec was doped with known Ti contents and the XRF spectra were recorded for Ti-doped materials. The signals associated with the $TiK_{\alpha1}$, $K_{\alpha2}$ and $K_{\beta1}$ emissions were identified for all Ti-doped samples. As expected, these signals strengthen with increasing Ti doping content (Figure 5 [II]). The intensities observed for the $TiK_{\alpha1}$ emission of all Cl-Hec:Ti^{3+} materials were then used to obtain a standard addition calibration curve (Figure S3 [II]) which, by extrapolation, gave a semi-quantitative value of the Ti concentration present in the neutral Cl-Hec material. It was found that the neutral Cl-Hec has a Ti content of 58 ppm. This value agrees well with the result obtained through an ICP-MS measurement, which showed a Ti concentration of 71.00±15.91 ppm in the neutral Cl-Hec. Thus, the agreement between the two different methods validated the XRF method as a semi-quantitative means for the determination of Ti in the X-Hec materials [II]. The calibration curve discussed above was used to qualitatively estimate the titanium concentration in each X-Hec material, and the results are shown in Table 5. These results confirm the presence of Ti as impurity in the non-doped X-Hec materials with a concentration of a few tens of ppm. Moreover, other impurities (Fe, Mn and Cr) have been identified in the neutral Cl-Hec materials, through quantitative analysis of ICP-MS (Table 5).

The presence of iron may represent an issue to the luminescence efficiency of the X-Hec materials: Because especially Fe^{3+} is a known luminescence quencher and the Fe concentration is fairly high for an impurity (81 ppm), it may induce luminescence quenching. Indeed, when Fe species are found in the structure of clay minerals, they usually occupy the octahedral units as trivalent cations. Unfortunately, the presence of the impurities could not be controlled in the current work.

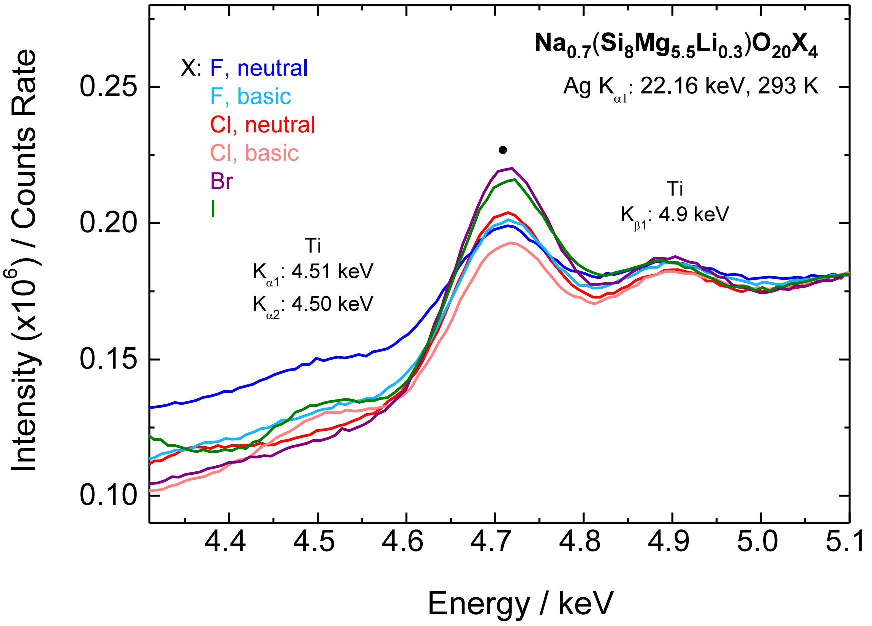

Figure 23. The presence of titanium impurities identified in the XRF spectra of all X-Hec materials (•: instrumental signal).

Table 5. The qualitative concentrations of Ti in the X-Hec materials estimated from the respective XRF spectrum of each material. ICP-MS results concerning Ti and other possible luminescent impurities are presented for neutral Cl-Hec as well.

X-Hec, X:	**F, neutral**	**F, basic**	**Cl, neutral**	**Cl, basic**	**Br, neutral**	**I, neutral**
XRF measurements						
Ti concentration (ppm)	61	51	58	67	58	59
x_{Ti} (mol-%)	0.0061	0.0051	0.0058	0.0067	0.0058	0.0059
ICP-MS analysis						
			Cl, neutral			
Ti concentration (ppm)			71.00 ± 15.91			
Fe concentration (ppm)			81.05 ± 6.05			
Mn concentration (ppm)			0.49 ± 0.33			
Cr concentration (ppm)			3.90 ± 1.07			

4.3. Physical properties

4.3.1. Nitrogen sorption isotherms and microscopy images

The porosity and packing features of the X-Hec materials were evaluated through the respective nitrogen sorption isotherms. Figure 24 shows the isotherms of the non-doped neutral X-Hec materials, whereas those of the basic materials are presented in [III]. The isotherms of all non-doped X-Hec materials have the characteristic shape of type V isotherms, according to the IUPAC classification [103], which is typical of mesoporous materials. Since the non-doped X-Hec materials behave as mesoporous materials, the hysteresis loop of their sorption isotherms can be correlated with the respective textures [103]. However, the shape of the hysteresis loop varies for the different X-Hec materials (Table 6). The F-Hec materials (both, basic and neutral) have a type H_4 hysteresis indicating a texture with narrow slit pores [III]. The Cl-Hec materials (both, basic and neutral) present a H_2 type hysteresis loop associated to a non-uniform distribution of pore size and shape indicating bottleneck constrictions in these materials [III]. The Br-Hec and I-Hec materials show the H_3 type of hysteresis loop due to slit-shaped pores. This indicates that there are no limitations for adsorption at high P/P_0, meaning that it has the typical texture of non-rigid aggregates of plate-like particles [IV]. The previous literature reports about the mesoporous features of synthetic hectorites [104,105] agree with the isotherms recorded here for the X-Hec materials.

The physisorption phenomena were analyzed through two data reduction methods to calculate the surface area and pore volume of each material (Table 6). The specific surface areas (SSA) were calculated with the BET method [89] considering the model of a multilayer coverage. The SSA values obtained for the X-Hec materials vary from 249 to 514 m^2g^{-1} with the lowest and highest values calculated for the basic F-Hec and neutral Cl-Hec, respectively. The literature reports different SSA values for hectorites: natural fluorohectorites have SSA ranging from 7 to 75 m^2g^{-1} (depending on the particle size) [106] and natural hectorites usually show low SSA (35.6 m^2g^{-1}) [107]. Synthetic hectorites have SSA between 5 and 300 m^2g^{-1} [108] and the commercial Laponite® shows SSA values from 279 to 375 m^2g^{-1} [104,108,109]. Thus, the Cl-Hec materials have higher SSA values than expected for non-treated hectorite types of clay minerals, while all other X-Hec materials show similar SSA values to the ones reported in the literature.

The volume of the mesopores was calculated using the method described by Rouquerol et al. [90] and it indicated pore volumes between 0.17 to 0.54 cm^3g^{-1} for the X-Hec materials (Table 6). The pore volumes were constant in the adsorption and desorption curves indicating that the X-Hec materials have the reversible adsorption process expected for mesoporous materials, and desirable for catalysts. In general, it seems that there is a trend of increase of pore volume with the increase of the ionic radius as intuitively expected. The neutral Cl-Hec is an exception, however.

The STEM images of the F-Hec and Cl-Hec materials (Figure 25) show the expected morphology for the synthetic hectorites, i.e. the presence of thin plates typical of smectite clays [66,110]. Both materials contain aggregated platelike quasi-circular particles with diameters in the order of nanometers. The TEM images of the F-Hec and Cl-Hec materials (Figure 2 [III]) also indicate that the crystallites have agglomerated to nanosized clusters, with the distance perpendicular to the sample holder surface being much less (a few nanometers) than that along the surface (a few hundred nanometers) [III]. Therefore, these observations are in agreement with the respective XPD patterns of the X-Hec materials. However, the size distribution could not be calculated due to the high agglomeration of the particles. At higher orders of magnification, the images of the Cl-Hec materials seem to reveal higher agglomeration than those of the F-Hec materials. However, all materials have strong cluster formation as it can be seen in the image of the neutral F-Hec at lower magnification (Figure 25, upper). Unfortunately, the STEM images of the Br-Hec and I-Hec materials could not be obtained, since the facilities used are no longer available.

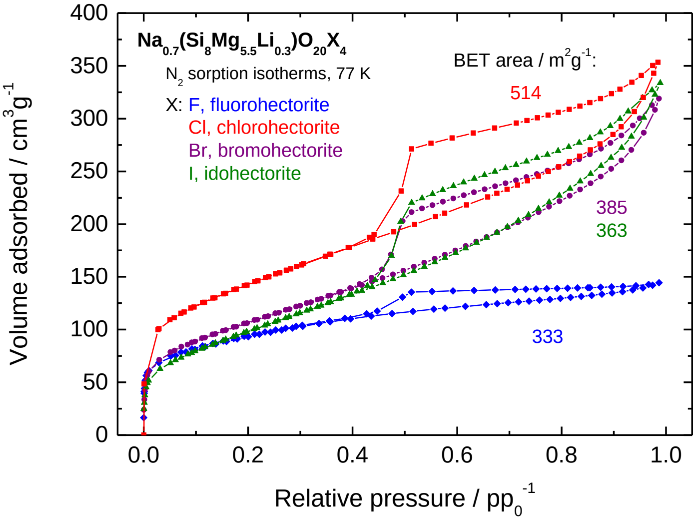

Figure 24. Nitrogen adsorption and desorption isotherms of the non-doped neutral X-Hec materials [III, IV].

Table 6. Evaluation of the collected surface area and pore volume of the non-doped X-Hec materials [III, IV].

X-Hec, X:	**F, neutral**	**F, basic**	**Cl, neutral**	**Cl, basic**	**Br, neutral**	**I, neutral**
SSA (BET) (m^2g^{-1})	333 ± 1	249 ± 1	514 ± 2	434 ± 2	385 ± 5	363 ± 4
Pore volume* (cm^3g^{-1})	0.22 ± 0.01	0.17 ± 0.01	0.54 ± 0.01	0.40 ± 0.01	0.48 ± 0.01	0.50 ± 0.01
Type of hysteresis loop (IUPAC [103]**)**	H_4 (narrow slit pores)	H_4 (narrow slit pores)	H_2 (bottleneck constrictions)	H_2 (bottleneck constrictions)	H_3 (slit-shaped pores)	H_3 (slit-shaped pores)

*Pore volume adsorbed and desorbed

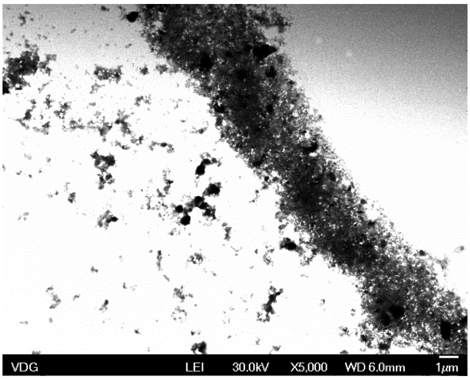

neutral, F-Hec

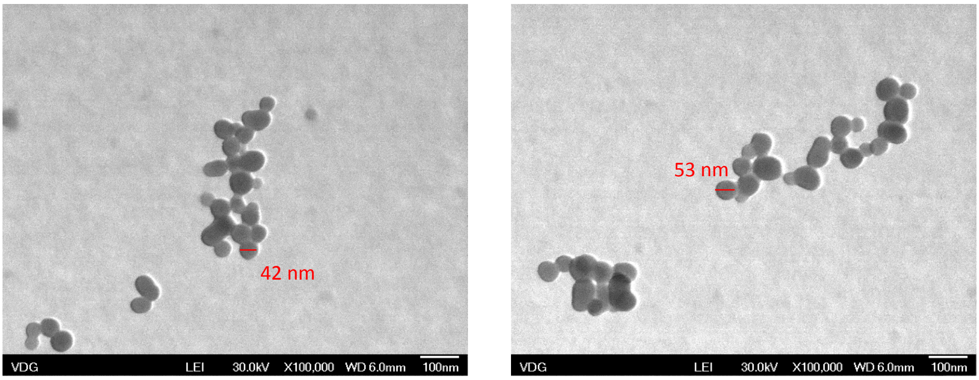

neutral, F-Hec

basic, F-Hec

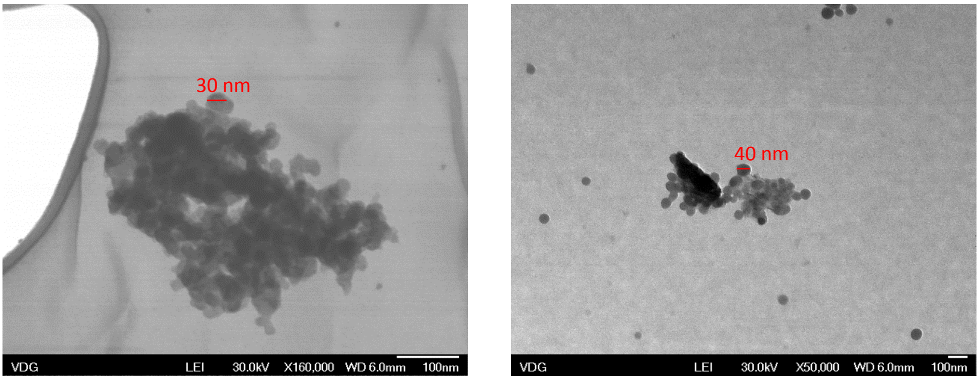

neutral, Cl-Hec

basic, Cl-Hec

Figure 25. STEM images of the F-Hec and Cl-Hec materials.

4.3.2. Thermoanalysis

The TGA-DSC analyses of the X-Hec materials (Figure 5 [III] and Figure 6 [IV]) show the three main weight loss events expected for hectorite type of clay minerals that lead to the breakdown of the structure. The Table 7 summarizes the temperature and mass losses associated with the events for each material. The first endothermic DSC signal identified from 89 to 114 °C is assigned to the loss of adsorbed water [96,111] and the loss varies according to the humidity contents of each material [III, IV]. The second event represents the loss of the coordinated water from the interlayer space (in the inner hydration shell of Na^+), and locked water inside the possible cavities in the clays' structure [96,111]. Due to the broad features of this event (between ca. 340 and 625 °C), the TGA and DSC curves do not show these changes clearly. However, it can be well identified from the first derivative of the TGA curves (Figure S2 [III], Figure S1 [IV]) which also allows the calculation of the mass loss related to this event (Table 7). The total mass loss of water varies from 7.4 to 17.8 % in the X-Hec materials depending on the adsorption capacity of each material in agreement with the SSA values found for these materials (Table 8).

The interpretation of this second occurrence differs from the usual observation reported for hectorite clay minerals, where the release of the coordinated water occurs concomitantly with the dehydroxylation (loss of structural OH^- ions) in a temperature range between 300 and 800 °C [96,111]. Since the X-Hec materials were designed based on the hectorite structure, but replacing its OH^- ions with halogen ions, they do not present the dehydroxylation event, shortening the temperature range of the weight loss which here is related just with the loss of coordinated water. The relation between this occurrence and the loss of coordinated water is further confirmed with the ex situ XPD (Figure S7 [III]) and FTIR analyses (Figure 22 and Figures S8 to S11 [III]) of the F-Hec and Cl-Hec materials: After heating the non-doped F-Hec and Cl-Hec materials at 600 °C for 30 min, the respective ex situ XPD patterns (Figure S7 [III]) still show the crystal structure similar to that of nanocrystalline fluorohectorite. Only small shifts or broadening of the 001 reflection is observed, which is associated with the loss of the coordinated water in the interlayer space. Moreover, the respective ex situ FTIR spectra (Figure 22) do not show remarkable changes when compared with those of the materials dried at 200 °C (Figure 21), losing just the weak bands related to H–O–H bending and stretching modes, which reappear in the spectra with increasing the time of exposition to the atmospheric air (Figures S8 to S11 [III]), due to the high hydrophilic character of the X-Hec materials. Therefore, all these observations connect the nature of this second occurrence with the loss of coordinated water in the interlayer space of the X-Hec materials.

The third and last exothermic signals in the DSC curves represent the collapse of the mineral structure releasing the corresponding halogen gas (F_2 (g), Cl_2 (g), Br_2 (g) or I_2 (g)). The breakdown results in the formation of the respective stable oxides: magnesium oxide (MgO), lithium oxide (Li_2O), sodium oxide (Na_2O), enstatite ($MgSiO_3$) and SiO_2. The ex situ XPD measurements of the Br-Hec and I-Hec materials after heating the materials up to 1000 °C (Figure S2 [IV]), show mainly the collapse of the mineral structure into enstatite and cristobalite (SiO_2), and the presence of other crystalline phases that could not be identified. On the other hand, the ex situ XPD patterns recorded for F-Hec and Cl-Hec materials after heating at 1000 °C (Figures S12 to S15 [III]), indicate the formation of all the expected stable oxides. This event also indicates that the thermal stability of the X-Hec materials extends up to 800 °C (except from the F-Hec materials which have the collapse of the mineral structure at ca. 770 °C). In addition, the higher mass loss observed for the neutral Cl-Hec material may indicate an excess of oxygen in the layers of this clay material inducing a release of O_2(g) with the collapse of its structure [III, IV]. The neutral Cl-Hec also shows two weak endothermic signals in the DSC curves at 609 and 639 °C, which may indicate some conformational changes in the layers before the collapse of the mineral structure. This signal is not observed for the other X-Hec materials [III].

Table 7. Temperatures and mass losses of the three main events identified in the TGA-DSC analyses of the X-Hec materials [III, IV].

X, Hec, X:	*Loss of adsorbed water*		*Loss of coordinated water*		*Collapse of mineral structure*	
	T (°C)	*Mass loss (%)*	*T (°C)*	*Mass loss (%)*	*T (°C)*	*Mass loss (%)*
F, neutral	104	3.9	340 – 625	4.6	775	2.7
F, basic	114	3.2	340 – 625	4.2	772	2.3
Cl, neutral	93	3.4	340 – 625	6.9	818	6.3
Cl, basic	94	7.8	340 – 625	10.0	807	2.7
Br, neutral	89	3.0	380 – 640	7.2	828	2.5
I, neutral	114	1.8	340 – 625	6.5	813	2.5

Table 8. Correlation between the total water loss (humidity) and surface area of the X-Hec materials

X-Hec, X:	**F, neutral**	**F, basic**	**Cl, neutral**	**Cl, basic**	**Br, neutral**	**I, neutral**
Humidity (%)	8.5	7.4	10.3	17.8	10.2	8.3
SSA (BET) (m^2g^{-1})	333 ± 1	249 ± 1	514 ± 2	434 ± 2	385 ± 5	363 ± 4

4.4. Ti^{3+} as luminescent center of the non-doped X-Hec materials

The X-Hec materials have a yellowish body color under white light and a blue luminescence under UV radiation (Figure 26, top). The respective reflectance spectra (Figure 26, bottom) further agree with the body color appearance of the X-Hec materials, showing a main broad band of absorption in the blue region (ca. 450 nm), which results in the yellowish color of the powders. The origin of the absorption band needs further studies. The emission spectra (λ_{exc}: 255 nm) of the X-Hec materials (Figure 27, top and Figure 28, top) display a main broad blue-green emission band with the barycenter at ca. 460, 465, 470 and 490 nm for the F-Hec (neutral and basic), Cl-Hec (neutral and basic), Br-Hec and I-Hec, respectively. A similar blue-green emission has been observed previously for other silicates such as montmorillonite [84], kaolinite [75], pyrophyllite [80], topaz ($Al_2SiO_4(F,OH)_2$) [4], synthetic hackmanite ($Na_8Al_6Si_6O_{24}(Cl,S)_2$) [30,31], benitoite ($BaTiSi_3O_9$) [20] and SiO_2 [50,51]. Moreover, all the X-Hec materials present a weak red emission at ca. 710 nm and it is most prominent for the basic Cl-Hec and Br-Hec materials. When the materials are excited at 365 nm this main emission is observed as a broad green-yellow emission band (Figure 27, bottom and Figure 28, bottom), with the barycenter at ca. 480, 505, 530 and 562 for the F-Hec (neutral and basic), Cl-Hec (neutral and basic), Br-Hec and I-Hec, respectively. The weak red emission still remains at ca. 710 nm [I-IV]. The main emission band is broad and asymmetric for all X-Hec materials, presenting a shift in the barycenter with the variation of the excitation wavelength. This indicates that the activator center is occupying multiple sites in the host lattice [29].

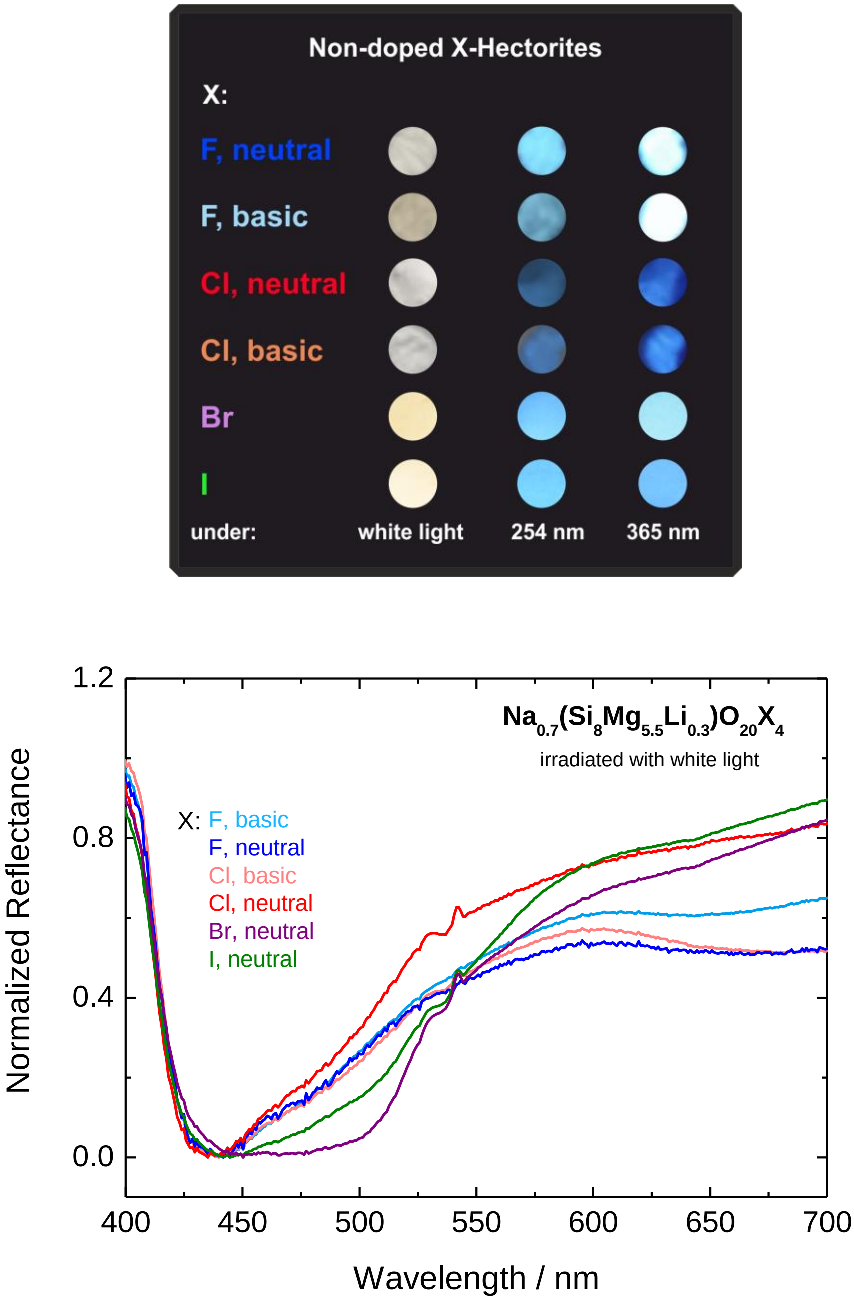

Figure 26. Visual appearance of the X-Hec materials under white light and UV radiation (top) [I-IV], and the reflectance spectra of the X-Hec materials under white light (bottom).

The X-Hec materials have their luminescence emission best explained through the existence of Ti^{3+} impurities in the octahedral layers of these materials. To confirm Ti^{3+} as luminescent center of the X-Hec materials, the neutral Cl-Hec material was doped with Ti^{3+} (with concentrations from 0.1 to 2.0 mol-%). The emission spectra (λ_{exc}: 255 nm) of the Ti^{3+}-doped materials (Figure 6 [II]) show that the main blue/green emission is stronger for all Ti^{3+}-doped materials when compared with the non-doped Cl-Hec. This suggests that Ti^{3+} impurity is the origin of luminescence in the non-doped materials instead of the possible oxygen-deficient SiO_2^{2-} centers.

In order to make explicit the difference between the emission bands generated by the Ti^{3+} impurities in the X-Hec materials and those commonly observed in silicate materials, the luminescence spectrum of a natural hectorite sample was also recorded keeping the same measurement parameters. The emission spectrum (λ_{exc}: 255 nm) of the natural hectorite (Figure S5, left [II]) presents a broad blue emission (490 nm) and a more prominent red emission (710 nm), in agreement with previous studies of luminescence in SiO_2 [50,51]. These bands also seem similar to those observed for the X-Hec materials in the present work. In the case of possible SiO_2^{2-} center emission, the red emission is expected to be quenched, when the basicity is increased by adding NaOH. This has been suggested to be due to the presence of alkali ions close to the non-bridging oxygen with trapped hole [49]. However, the F-Hec and Cl-Hec materials have the opposite behavior, showing an increase of red emission in basic medium (Figure 28). Besides, when the natural hectorite was excited at 365nm, the blue emission band vanishes from its spectrum (Figure S5, right [II]), and the red emission becomes almost unnoticeable. These observations presented above confirm that Ti^{3+} is the emitter in the X-Hec materials [II].

The main emission band is slightly red-shifted (to 490 nm) for the Ti^{3+}-doped samples and the breadth of the band decreases from *ca.* 6500 to 6100 cm^{-1} between the non-doped and 2 % doped material. Because the emission band is broad, one can assume that the emission results from multiple Ti sites. In comparison with the impurity Ti species, the doped Ti species seem to favor sites that have a lower crystal field strength, which causes the maximum of the band to shift to lower energy and to decrease in width. The emission intensity increases with the Ti content until 1.5 mol-%. The reason for the decrease in higher concentrations may be that the solid solubility of titanium to the Cl-Hec lattice extends only to 1.5 mol-%. On the other hand, it may also be that in the higher concentrations the Ti species aggregate, which results in concentration quenching of the emission [II].

It was possible to determine the valence of titanium with XPS from the Cl-Hec material doped with 2 mol-% of Ti. The results indicate that both Ti^{3+} and Ti^{IV} are present (Figure 8 [II]) based on the $2p_{3/2}$ signals at 457.8 and 458.9 eV [112]. Even if the low ppm Ti concentration prevents the determination of the Ti valence in the non-doped materials, it can be assumed that both Ti^{3+} and Ti^{IV} will be present, because of the similar synthesis conditions. The XPS results thus confirm the assignment of the bands in the excitation spectrum [II]. Moreover, the materials studied in the current work have low contents of Ti as confirmed from their respective XRF spectra (Figure 23).

The luminescence properties of oxide materials that have titanium as an impurity have been commonly defined by the presence of Ti^{3+} and

Ti^{IV} [29]. Also, previous reports have shown that Ti can occur as an impurity in oxides, generating similar emission features as reported for silicate glasses [24] and hafnates [113]. In the non-doped X-Hec materials the titanium impurities originate from the SiO_2 used as precursor to synthesize the materials, where Si^{IV} has been replaced by Ti^{IV}. Since the octahedral coordination has preferential geometry for titanium complexes [4], the initial impurities migrate to the octahedral layers substituting either Mg^{2+} or Li^{+}. Moreover, four-coordinated Ti has been reported only within highly disperse Ti-silicate structures [114]. In the octahedral sites, titanium is driven to the trivalent form to better match the size and charge in that site. The presence of Ti^{IV} is also possible due to the low reduction potential between the two species, about *ca.* –0.56 and –0.09 eV in solid and aqueous solution, respectively (Eqs. 3 and 4) [115]. Furthermore, the brownish body color of the X-Hec materials is a common feature expected due to the presence of Ti^{3+} formed in non-oxidizing host matrices [28][I-IV].

$$2\,TiO_2(s) + 2\,H^+ + 2e^- \rightarrow Ti_2O_3(s) + H_2O \qquad E^0 = -0.556\,eV \qquad (3)$$

$$2\,TiO_2(h,s) + 2\,H^+ + 2e^- \rightarrow Ti_2O_3(h,s) + H_2O \quad E^0 = -0.091\,eV \qquad (4)$$

The main blue-green emission presents a trend of red shift as a function of the atomic number of the halogen (Figures 27 and 28). This observed emission red shift can be easily explained with the ligand-field theory: the halogens are strong π-donor ligands ($F^- < Cl^- < Br^- < I^-$) which have full π orbitals lower in energy than the $3d^1$ orbitals of Ti^{3+}. When they form molecular orbitals with the t_{2g} orbitals of Ti^{3+} these nonbonding t_{2g} orbitals become antibonding. This increases the energy of the t_{2g} which thus gets closer in energy to the antibonding e_g orbitals [116]. The magnitude of this effect follows the order of the π-donor strength of the ligands generating the observed red shift. Similar observations have been reported for example in $CH_3NH_3PbX_3$ perovskites showing the red shift when bromine was replaced by iodine in the PbX_6 octahedra [117] [IV].

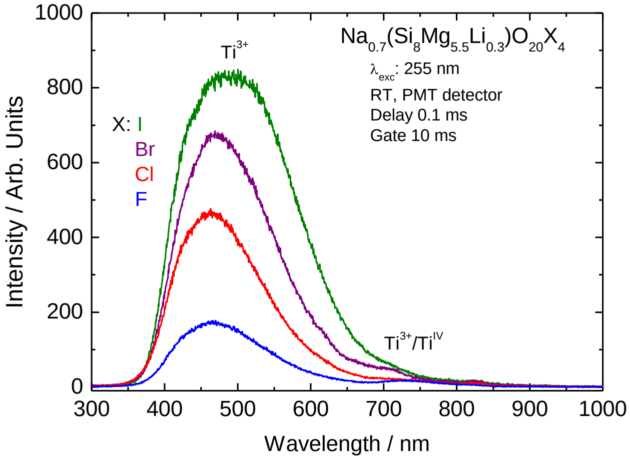

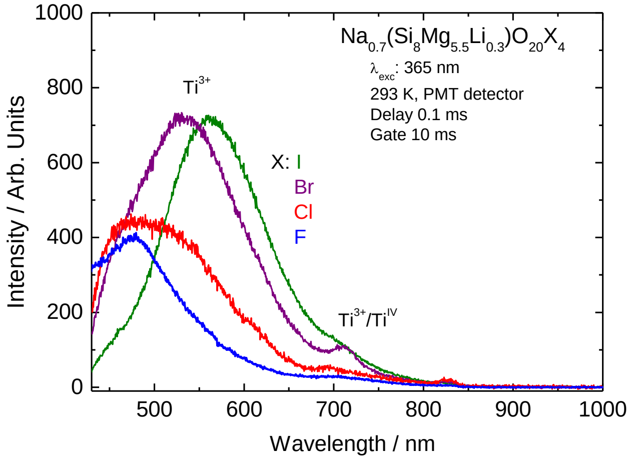

Figure 27. The emission spectra of the neutral X-Hec materials under 255 nm (top) and 365 nm (bottom) excitation [I-IV].

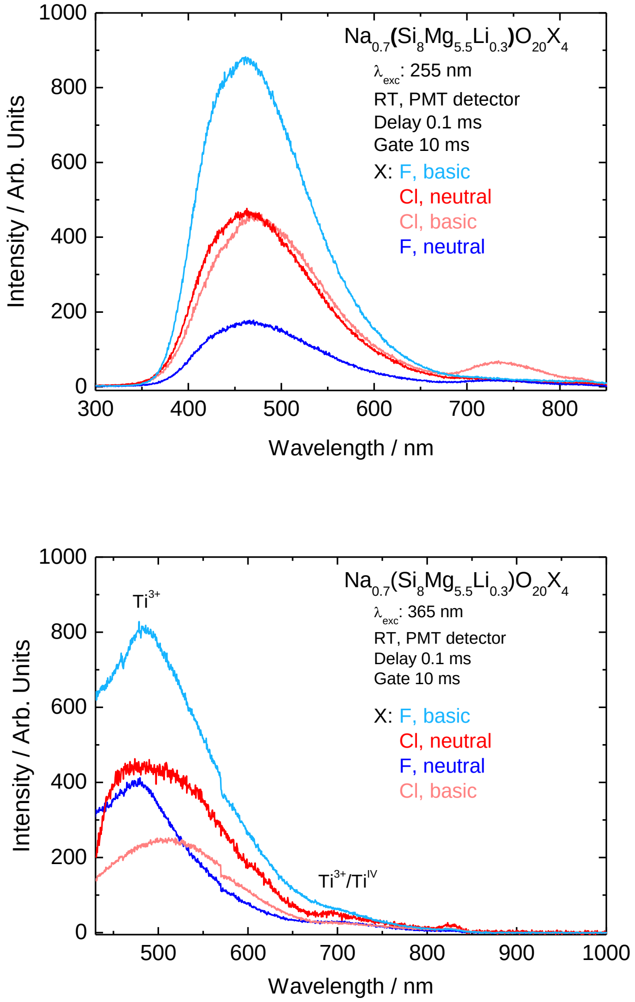

Figure 28. The emission spectra of the F-Hec and Cl-Hec materials (neutral and basic) under 255 nm (top) and 365 nm (bottom) excitation [I-IV].

The excitation spectra of the X-Hec materials (Figure 29) further confirm the role of Ti^{3+} as activator center in these materials: The broad bands seen at ca. 370 - 410 nm are assigned to electronic transitions from the t_{2g} to e_g energy levels of Ti^{3+}, which agrees with previous reports for Ti^{3+} in monoclinic ZrO_2 (314 nm) [27] considering that d-d transitions are sensitive to the crystal field strength. The wide bands at ca. 287-300 nm are related to the e$^-$(O^{2-}(2p))→Ti^{IV} charge transfer, which is typically observed at ca. 280 nm [29,31,118]. Finally, the gap energy between the valence and the conduction band is identified at ca. 250 nm which agrees with the characteristic band gap energy of hectorites (260 nm) [119], confirming that titanium is in the hectorite structure and not present as isolated impurity phase [I-IV].

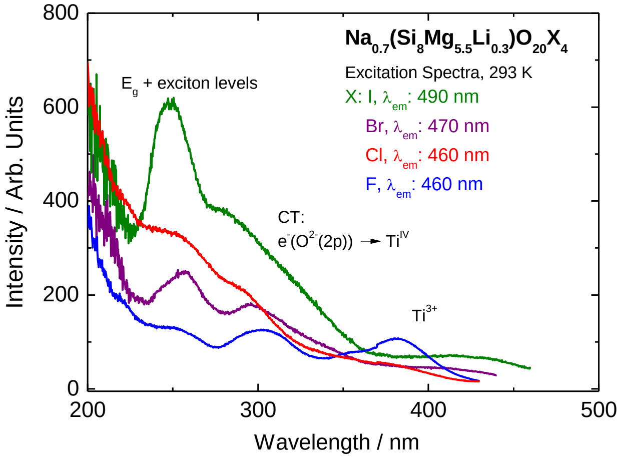

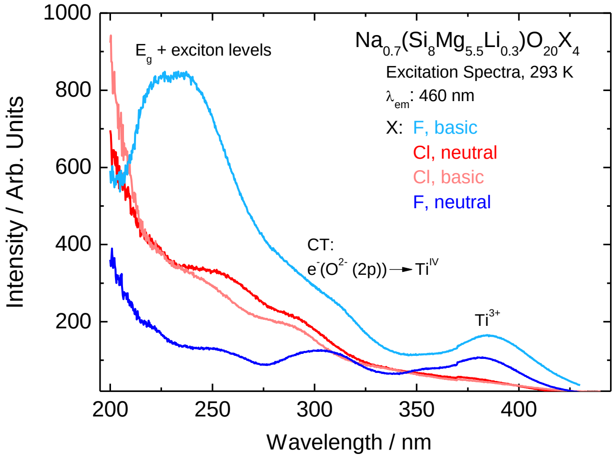

Figure 29. The excitation spectra of the neutral X-Hec materials (top) and the F-Hec and Cl-Hec materials at neutral and basic medium (bottom) [I-IV].

4.5. Persistent luminescence of the non-doped X-Hec materials

The luminescence decay curves of the X-Hec materials (Figure 30) indicate that all non-doped materials present short persistent luminescence, i.e. thermally stimulated luminescence at room temperature, lasting ca. 5 s. The typical emission lifetime of Ti^{3+} is in the order of microseconds [28], but the fits to the decay curves of the X-Hec materials show that the decay consists of components with lifetimes ranging from some hundred milliseconds to seconds (Table 9). Each material presents at least three lifetimes as calculated with a multiexponential fitting function. However, even with three lifetime components, only a part of each decay curve can be fitted reasonably (Figure 30, top and middle). This indicates that the overall decay is very complex with several contributing processes.

This short persistent luminescence is explained through the existence of defects in the layered structure of these materials. The traps act as electron traps storing energy for a short time. From all materials, the neutral Cl-Hec presents the longest emission lifetime which may be due to the highest defect concentration in its structure. Even though the X-Hec materials can store optical energy, they possess too shallow traps which do not allow any significant persistent luminescence at room temperature [I-IV]. This short persistent luminescence was also observed for the neutral Cl-Hec materials doped with Ti^{3+} (Cl-Hec:Ti^{3+}, x_{Ti}: 0.1 – 2.0 mol-%), but the lifetimes decrease with increasing Ti content (Figure 9 and Table 1 [II]) indicating that doping decreases the amount of defects capable of storing electrons [II].

The persistent luminescence excitation spectrum (Figure 30, bottom) was determined only for the basic Cl-Hec because it shows the longest persistent emission of the X-Hec materials. This was done by recording the decay curve for the 460 nm emission with varying the excitation wavelength from 255 to 395 nm and taking the intensity value at 0.2 s (i.e. at a point beyond any regular photoluminescence lifetime). It was observed that the short persistent luminescence can be observed with excitation below 325 nm. This confirms that the persistent luminescence is excited similarly as is the regular photoluminescence (see Figure 29), i.e. via the $e^{-}(O^{2-}(2p))\rightarrow Ti^{IV}$ charge transfer or through the conduction band.

Table 9. Emission lifetimes calculated for bromohectorite and iodohectorite by fitting the luminescence intensity (I) to the function: $I = I_0 + A_1e^{-t/\tau 1} + A_2e^{-t/\tau 2} + A_3e^{-t/\tau 3}$. Here, A: amplitude, t: time and, τ: lifetime. The values in parentheses show the calculated esd's.

X-Hec, X:	**τ1 /s**	**A1 / %**	**τ2 /s**	**A2 / %**	**τ3 /s**	**A3 / %**
F, neutral	0.32(12)	74	0.78(18)	24	2.93(85)	2
F, Basic	0.32(3)	76	0.70(7)	22	1.85(33)	2
Cl, neutral	1.14(17)	29	0.31(6)	40	0.06(2)	31
Cl, basic	0.45(8)	52	0.99(18)	40	2.34(53)	7
Br, neutral	0.04(6)	61	0.20(4)	29	0.87(11)	10
I, neutral	0.06(6)	53	0.30(3)	35	1.07(8)	12

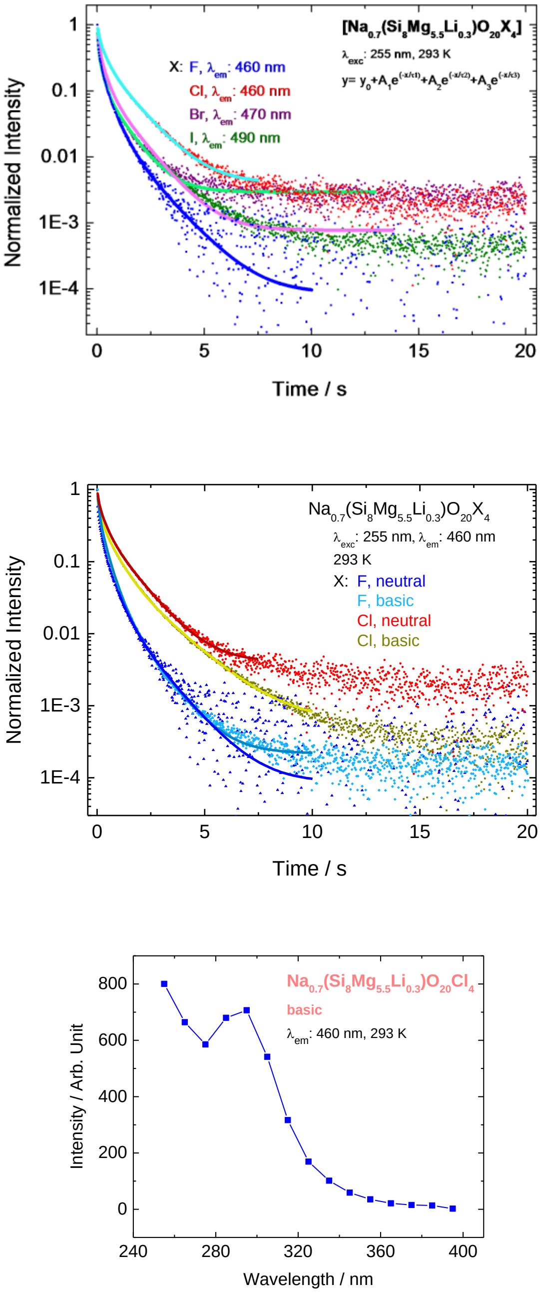

Figure 30. Normalized persistent luminescence decay curves of the neutral X-Hec materials (top) and the decay curves of the F-Hec and Cl-Hec materials in neutral and basic medium (middle). The bottom curve shows the persistent luminescence excitation spectrum of Cl-Hec obtained from decay curves.

The thermoluminescence (TL) glow curves of the X-Hec materials (Figure 31, top) further confirm the prolonged emission lifetimes of the X-Hec materials as a short persistent luminescence. All X-Hec materials have weak TL bands which confirm the presence of traps emptying spontaneously below/close to RT. The intensity of the TL bands varies for each material being highest for the neutral Cl-Hec and lowest for the I-Hec. This indicates higher concentration of traps with suitable depths for room temperature TL for the former. Following the variation in intensity of the TL bands, it can be deduced that the amount of suitable traps in the X-Hec materials increases in this order: I-Hec < Br-Hec < basic Cl-Hec < neutral F-Hec < basic F-Hec < neutral Cl-Hec. This agrees with the lifetimes calculated from the luminescence decay curves (Table 9).

The energies related to these traps were calculated by using the model-free initial rise method (Figure 31, bottom) [91]. The trap energies vary from 0.038 to 0.195 eV, meaning that the traps are too shallow, getting empty fast at room temperature. The basic Cl-Hec material shows a decline instead of an initial rise. Thus, its trap energy could not be calculated. The generation of efficient persistent luminescence requires trap energies between ca. 0.5 and 1.0 eV [120]. Therefore, the TL glow curves of the X-Hec materials show that all of them are capable of storing optical energy, but the traps are much too shallow to generate significant persistent luminescence at RT [II].

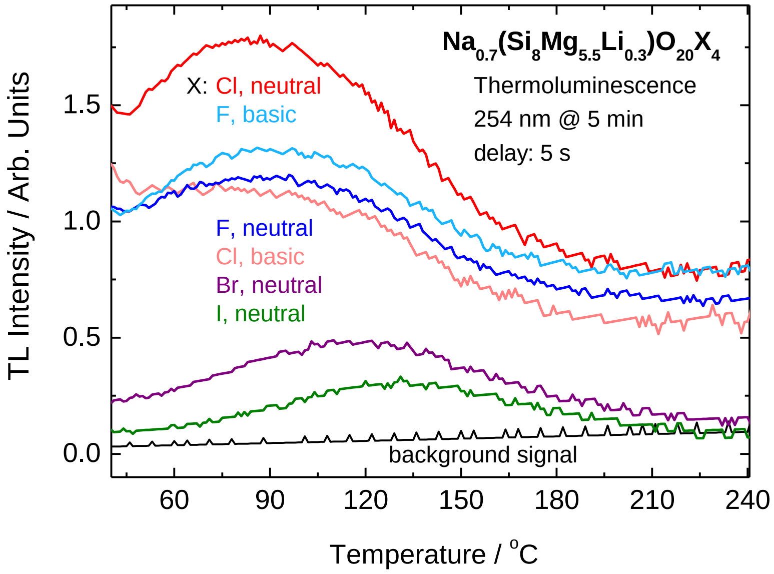

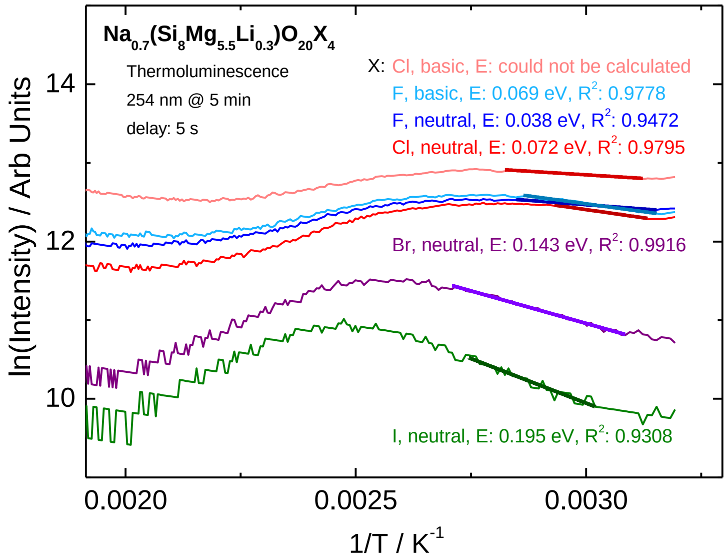

Figure 31. TL glow curves of the non-doped X-Hec materials (top) and the respective initial rise TL curves (bottom).

The mechanism of Ti^{3+} persistent luminescence in the X-Hec materials can be explained based on the model proposed for $ZrO_2:Ti^{3+}$ [121]. Figure 32 illustrates the general mechanism, using the data obtained for the neutral Cl-Hec material, which can be explained as follows: the excited 3d levels of Ti^{3+} overlap with the conduction band, but at least the lowest levels must be located below the conduction band or else no emission could be observed. When the Ti^{3+} is excited, a part of the excited electrons may escape to the conduction band. The electrons move freely in the conduction band until they are trapped to a defect with an energy level close to the bottom of the conduction band. The electrons are freed from the trap with the aid of the thermal energy available at room temperature. Subsequently, the electrons are raised back to the conduction band with this thermal energy. They move in the conduction band until they reach the excited levels of Ti^{3+}. Finally, the excited Ti^{3+} relaxes emitting at 460 – 490 nm, according to the luminescence emission observed for each X-Hec material [II].

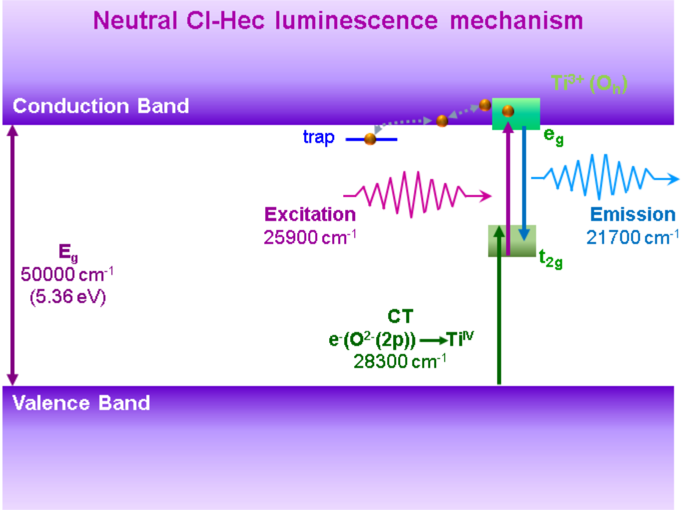

Figure 32. Luminescence mechanism of the X-Hec materials based on the data of the neutral Cl-Hec material.

4.6. Fluorohectorite and chlorohectorite doped with Eu^{3+} and/or Tb^{3+}

The characterization of the X-Hec materials detailed above shows a combination of features which points the X-Hec materials as potential candidates to act as host lattices for several guest species (optically active or not). The following desirable features for host lattices are present in the X-Hec materials: (i) the crystal structure of smectite clay minerals with a wide interlayer space making it able to accommodate extraneous guest species (ii) the chemical environment characteristic of the layered hectorites’ structure, (iii) high surface area and, (iv) thermal stability up to 700 - 800 °C, depending on the type of X-Hec material. To test if these features would also allow the doping with lanthanides which commonly require higher coordination numbers (10 to 12) than those available in hectorite (6 to 8), the F-Hec and Cl-Hec materials (neutral and basic) were doped with Eu^{3+} and/or Tb^{3+} [III]. The easy cation exchange in the interlayer space of clay minerals, especially the smectite types, is a well-known feature of these materials [122,123]. Thus, the doping was carried out by a cation exchange of one mol of Eu^{3+} and/or Tb^{3+} by three mols of Na^+ [III].

Visually, the F-Hec and Cl-Hec materials had their yellowish-brownish body color under white light accentuated after the doping with Eu^{3+} and/or Tb^{3+} species (Figure 6 [III]). When the doped materials are under UV radiation, they present: (i) a violet/red appearance for the Eu^{3+}-doped (Figure 6, upper right [III]), (ii) a green for the Tb^{3+}-doped (Figure 6, lower left [III]) and, (iii) variations between blue, green and red appearance for the Eu^{3+} and Tb^{3+} co-doped materials (Figure 6, lower right [III]). The following sections discuss the luminescence phenomena in the Eu^{3+} and/or Tb^{3+}-doped F-Hec and Cl-Hec materials by comparing the luminescence spectra of the studied doped materials with the results seen in other matrices.

4.6.1. Photoluminescence of X-Hec:Eu^{3+} materials

The emission spectra (λ_{exc}: 255 nm) of X-Hec:Eu^{3+} materials (Figure 33, top) show five main lines with the barycenter at 580, 592, 613, 653 and 700 nm assigned to the transitions from $^5D_0$ to ^7F_J (J=0,1,2,3,4) energy levels of Eu^{3+} [124,125]. The line centered at 613 nm appears as the strongest emission for all X-Hec:Eu^{3+} materials, generating a red appearance emission for these materials, which is also deducted from the CIE color coordinate diagram (Figure 9 [III]). The stronger intensity of the band related to $^5D_0 \rightarrow {}^7F_2$ transition (613 nm) in comparison with the band associated to $^5D_0 \rightarrow {}^7F_1$ transitions (592 nm), indicates that Eu^{3+} does not occupy a site with inversion symmetry, since the former transition is very sensitive to the crystal field around Eu^{3+} [126]. In addition, the neutral Cl-Hec:Eu^{3+} shows also a line centered at 536 nm due to the electronic transition $^5D_1 \rightarrow {}^7F_1$ of Eu^{3+} which indicates the low phonon energy of the neutral Cl-Hec host lattice [125]. The same transition is weakly noticed with the other Eu^{3+}-doped X-Hec materials [III].

All the X-Hec:Eu^{3+} materials have similar excitation spectra (λ_{em}: 613 nm, Figure 33, bottom). The band at ca. 260 nm is associated to the band gap energy (E_g) of the X-Hec materials. The broad band at ca. 280 nm is due to the $(O^{2-}(2p)) \rightarrow Eu^{3+}$ LMCT that might be overlapped with the $(O^{2-}(2p)) \rightarrow Ti^{IV}$ LMCT and the following peaks ranging from 390 to 540 nm are associated to the $^7F_{0,1} \rightarrow {}^5D_J$ (J=3, 2, 1) [127]. Moreover, the absence of the Ti^{3+} (d-d) bands indicates that there is no energy transfer from Ti^{3+} to Eu^{3+} in this host [III].

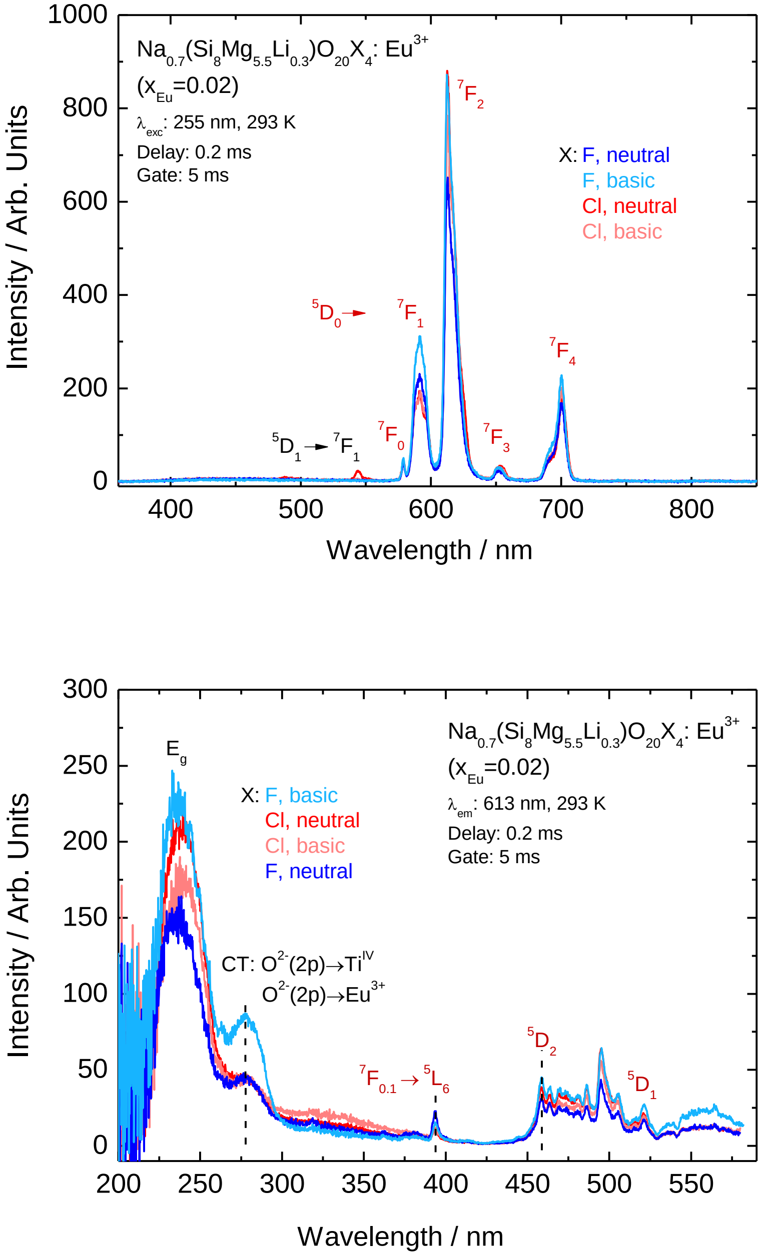

Figure 33. Emission spectra with 255 nm excitation (top) and excitation spectra for the 613 nm emission (bottom) of the F-Hec:Eu^{3+} and Cl-Hec:Eu^{3+} materials [III].

4.6.2. Photoluminescence of X-Hec:Tb^{3+} materials

The emission spectra (λ_{exc}: 255 nm) of the X-Hec:Tb^{3+} materials show the typical emission lines of trivalent terbium due to 4f-4f transitions (Figure 34, top), presenting four main bands with the barycenter at ca. 489, 543, 586 and 622 nm assigned to the $^5D_4 \rightarrow {}^7F_6$ (weak blue), $^5D_4 \rightarrow {}^7F_5$ (strong, green), $^5D_4 \rightarrow {}^7F_4$ (weak, yellow) and, $^5D_4 \rightarrow {}^7F_3$ (weak, red) transitions of Tb^{3+}, respectively [22,128,129]. The band centered at ca. 543 nm shows the highest intensity for all Tb^{3+}-doped materials, resulting in a predominantly green emission under UV radiation. The color coordinate diagram further shows the overall green emission of the X-Hec:Tb^{3+} materials (Figure 9 [III]) [III].

The excitation spectra (λ_{em}: 543 nm) of the X-Hec:Tb^{3+} materials (Figure 34, bottom) show features typical of a Tb^{3+} luminescent center. The peak associated to $^7F_6 \rightarrow {}^5D_4$ transition of Tb^{3+} is at ca. 465 nm [22,129]. The broad band at ca. 285 nm is related to the $(O^{2-}(2p)) \rightarrow Ti^{IV}$ LMCT, and the broad band at ca. 260 nm is related to the band gap energy of the X-Hec materials [119]. As noticed for the Eu^{3+}-doped materials, the Ti^{3+} (d-d) band is also absent, indicating that no $Ti^{3+} \rightarrow Tb^{3+}$ energy transfer occurs [III].

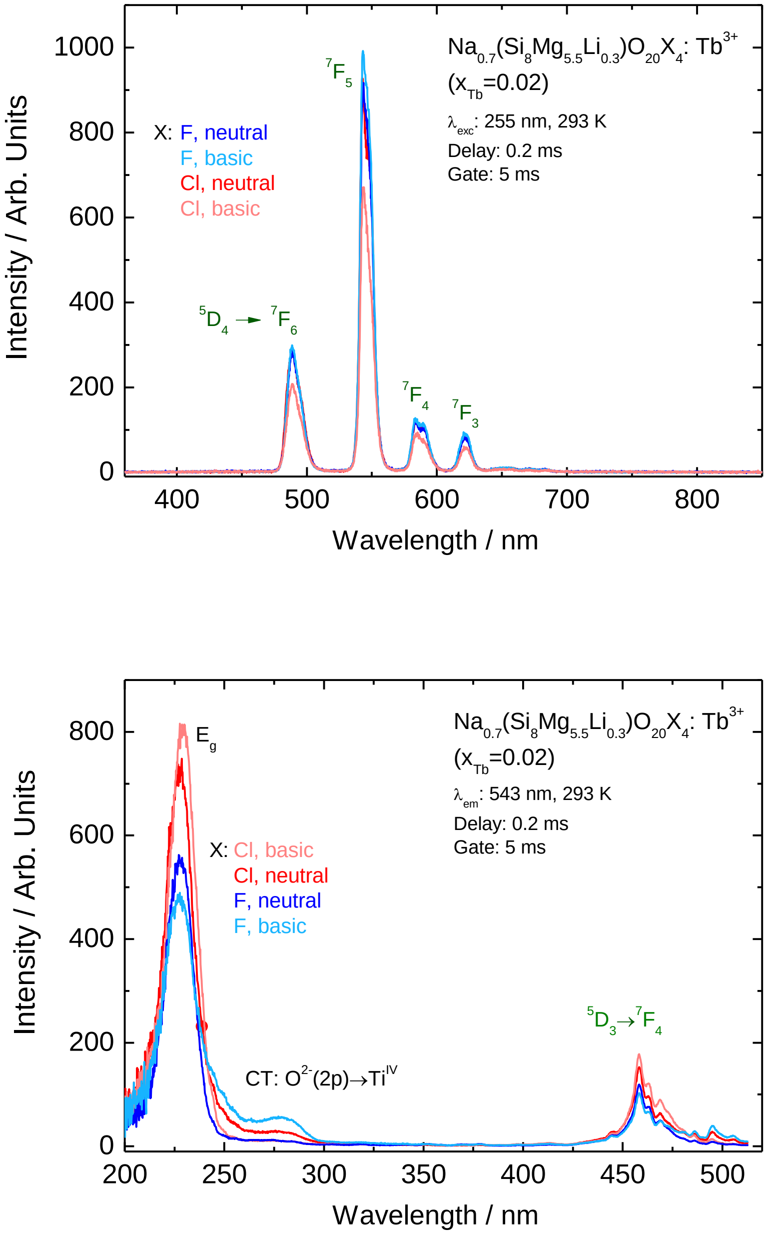

Figure 34. Emission spectra under 255 nm excitation (top) and excitation spectra for the 543 nm emission (bottom) of the F-Hec:Tb^{3+} and Cl-Hec:Tb^{3+} materials [III].

4.6.3. Photoluminescence of X-Hec:Eu^{3+},Tb^{3+} materials

The X-Hec:Eu^{3+},Tb^{3+} (x_{Eu}: 0.02 mol-%, x_{Tb}: 0.02 mol-%) materials have a yellowish-orange emission under UV radiation, showing an intermediary total emission between the X-Hec:Eu^{3+} and X-Hec:Tb^{3+} materials as it can be seen in the color coordinate diagram (Figure 9 [III]). However, the Cl-Hec:Eu^{3+},Tb^{3+} materials have their total emission closer to the Tb^{3+}-doped materials, while the F-Hec:Eu^{3+},Tb^{3+} materials present the total emission closer to the Eu^{3+}-doped materials. In Eu^{3+}/Tb^{3+} co-doped materials, it is more common to observe energy transfer from Tb^{3+} to Eu^{3+} than vice versa. On the other hand, if there was Eu^{2+} present, it could transfer energy to Tb^{3+} [130]. Since the europium was doped into the X-Hec lattices as a trivalent ion, they present only the emission bands corresponding to Eu^{3+}. Thus, if an energy transfer process would occur, it would be most probably observed from the energy levels of Tb^{3+} to Eu^{3+}. However, such energy transfer processes were not observed for the X-Hec:Eu^{3+},Tb^{3+} materials [III].

The emission spectra (λ_{exc}: 255 nm) of the Cl-Hec:Eu^{3+},Tb^{3+} materials (Figure 35) indicate the predominance of the Tb^{3+} emission for these materials. The four bands centered at 489, 543, 586 and 622 nm are associated to the $^5D_4 \rightarrow {}^7F_J$ (J = 6,5,4,3) transitions of Tb^{3+}. However the band centered at 622 nm may have a small contribution from the $^5D_0 \rightarrow {}^7F_2$ transition of Eu^{3+} and, the last band centered at 700 nm is clearly due to the $^5D_0 \rightarrow {}^7F_4$ transition of Eu^{3+} [130,131]. Thus, the excitation of the Cl-Hec host sensitizes Tb^{3+} more efficiently than Eu^{3+}. Moreover, these results indicate that the $Tb^{3+} \rightarrow Eu^{3+}$ energy transfer process in this host is not efficient [III].

The F-Hec:Eu^{3+},Tb^{3+} materials show mostly Eu^{3+} electronic transitions in their respective emission spectra with excitation at 255 nm (Figure 35). The transitions centered at 580, 592, 613, 653 and 700 nm, are due to the $^5D_0 \rightarrow {}^7F_J$

(J=0,1,2,3,4) transitions of Eu^{3+}ions [131,132]. Moreover, there are two bands associated to Tb^{3+} electronic transitions: the bands centered at 489 and 543 nm which are due to the $^5D_4\rightarrow{}^7F_J$ (J=6 and 5, respectively) transitions of Tb^{3+} [131]. Therefore, these results indicate that the excitation of the F-Hec lattices sensitizes better Eu^{3+} or that the Tb$^{3+}\rightarrow$Eu^{3+} energy transfer process is more efficient in the F-Hec lattice than in the Cl-Hec lattice. It has been reported that in some cases this energy transfer is phonon assisted [132], which could be an explanation to the more efficient Tb$^{3+}\rightarrow$Eu^{3+} energy transfer in the LS(F) host than the LS(Cl) one [III].

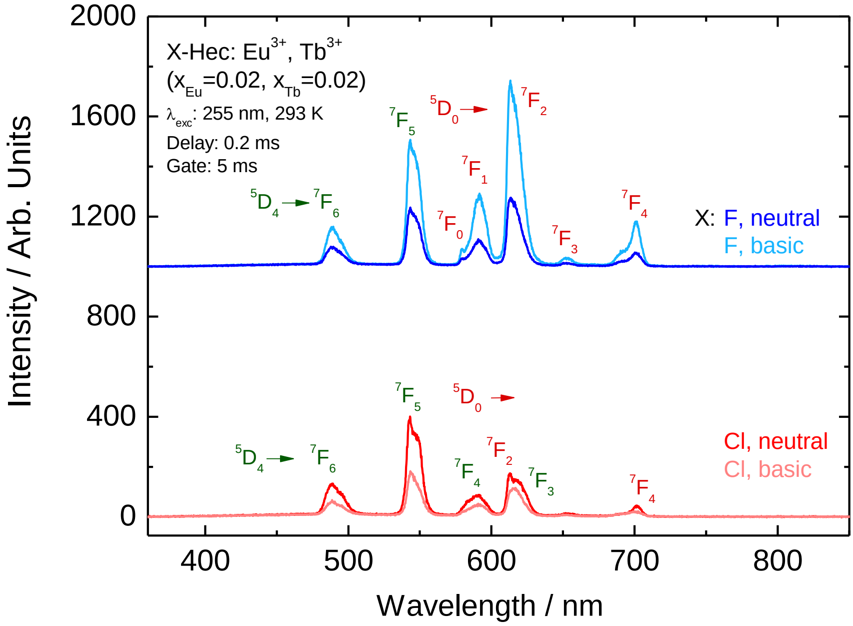

Figure 35. Emission spectra (λ_{exc}: 255 nm) of the F-Hec:Eu^{3+},Tb^{3+} and Cl-Hec:Eu^{3+},Tb^{3+} materials [III].

The excitation spectra of the X-Hec:Eu^{3+},Tb^{3+} materials (Figure 36) confirms the preference of the Tb^{3+} center to its emission in the Cl-Hec materials, and the Eu^{3+} as preferential emitter center in the F-Hec materials. When the emission spectra of the X-Hec:Eu^{3+},Tb^{3+} materials are recorded at 543 nm of emission (Figure 36, top), two main broad bands are observed at ca. 260 and 285 nm. They are related to the band gap energy [119] and the $(O^{2-}(2p))\rightarrow Ti^{IV}$ LMCT, respectively. These bands have higher intensity for the Eu^{3+},Tb^{3+}-doped Cl-Hec materials, in agreement with the observations in the emission spectra, confirming the trivalent terbium as main the emission center in these lattices.

The excitation spectra (λ_{em}: 612 nm) of the X-Hec:Eu^{3+},Tb^{3+} materials (Figure 36, bottom) show all bands in much higher intensity for the F-Hec doped materials. The peaks related to the Eu^{3+} electronic transitions are seen from 390 to 540 nm. They are assigned to the $^7F_{0,1}\rightarrow {}^5D_J$ (J=3, 2, 1) electronic transitions of Eu^{3+} [127]. The broad band at ca. 280 nm is related to the $(O^{2-}(2p))\rightarrow Eu^{3+}$ LMCT and it may be overlapped with the $(O^{2-}(2p))\rightarrow Ti^{IV}$ LMCT, and the band associated to the band gap energy at ca. 260 nm [119]. Since all bands have higher intensity for the F-Hec:Eu^{3+},Tb^{3+} materials, these results are coherent with the respective emission spectra, indicating Eu^{3+} as main luminescence center in the F-Hec materials [III].

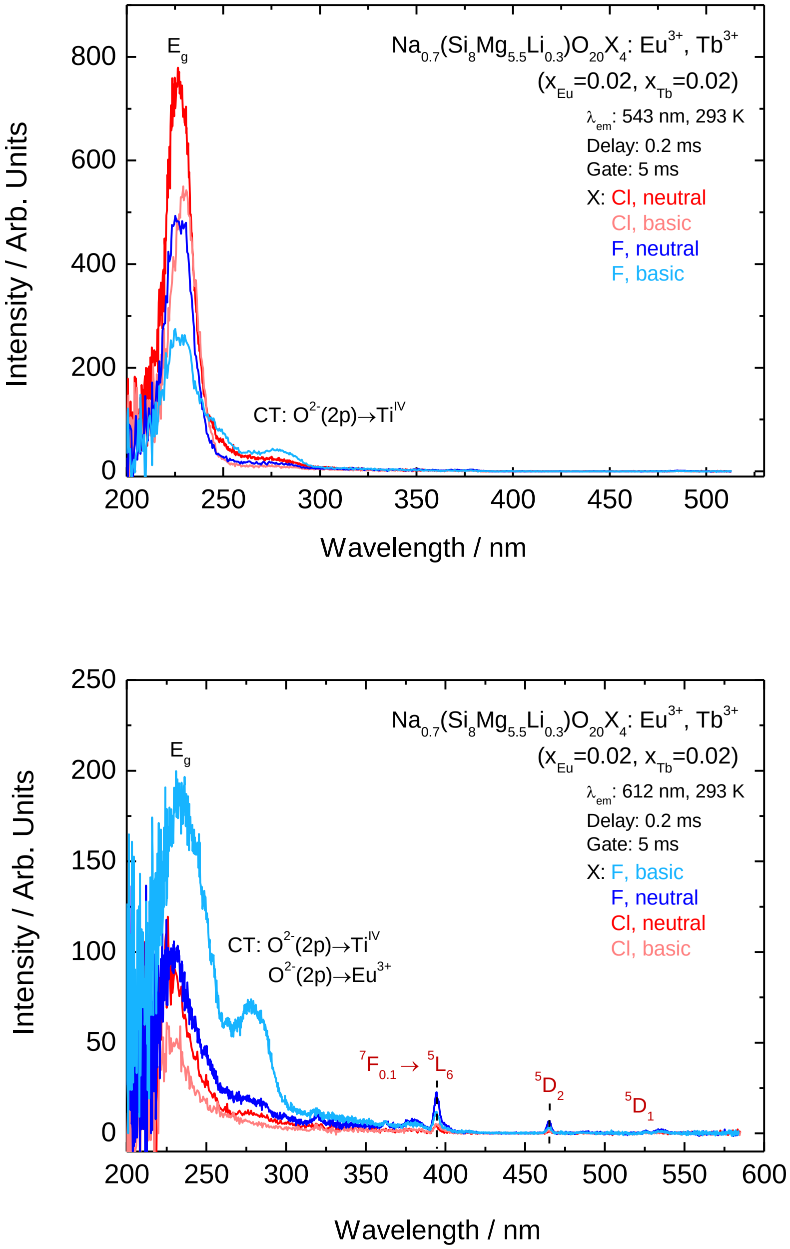

Figure 36. Excitation spectra (λ_{em}: 543 nm (top) and λ_{em}: 612 nm (bottom)) of the F-Hec:Eu^{3+},Tb^{3+} and Cl-Hec:Eu^{3+},Tb^{3+} materials [III].

5. Conclusions

The halogen-hectorites (X-Hec) have been successfully synthesized and the chlorohectorite, bromohectorite and iodohectorite materials are reported for the first time in this doctoral work. According to the XPD patterns, all X-Hec materials have similar hexagonal crystal structure to the nanocrystalline fluorohectorite, without formation of impurity phases. The X-Hec materials are nanosized along the 001 direction (3 nm), presenting a d_{001} spacing of 14.30 Å, which is suitable for intercalating two monolayers of water at RT. The STEM images of the X-Hec materials further confirm their plate-like structure. The XRF spectra confirmed the expected chemical composition of the X-Hec materials, and show an additional presence of Ti as impurity for all X-Hec [I-IV].

The FTIR spectra of the X-Hec materials do not present the signals associated to the hydroxyl groups in the octahedral layers of hectorites, indicating the total replacement of the hydroxyl groups of hectorite by the respective halogens. The ^{29}Si NMR spectra of all X-Hec materials show the Q^3 and Q^2 signals predicted for the tetrahedral layers of hectorites, indicating the formation of analogous chemical environment. The nitrogen sorption isotherms of the X-Hec materials show that all of them are mesoporous materials with high specific surface area (ranging from 249 to 514 m^2g^{-1}), which make them potential candidates for application as gas sensors or in electrochemical devices for charge storage. Moreover, all X-Hec materials show good thermal stability up to 750 – 800 °C, where the highest tolerable temperature varies according to the X-Hec type [I-IV]. The X-Hec materials have shown good chemical stability under atmospheric air, because there have been no signs of differences in their properties during two years of exposure to air. However, further studies would be necessary in order to define the chemical stability of the X-Hec materials, evaluating if their features could be affected e.g. under basic/acidic medium, and for how long the X-Hec materials can keep their stability when exposed to atmospheric air.

The X-Hec materials present a blue-green emission under UV-radiation, which is attributed to titanium impurities acting as the luminescent center in these materials. This main emission presents a red shift with the increase of the π-donor strength of the ligands, which decreases the energy difference between the e_g and t_{2g} levels thus red shifting the emission. The barycenter of the main emission varies with the excitation wavelength, indication that the titanium centers occupy multiple sites in the host lattice. The excitation spectra further confirms Ti^{3+} as luminescent center showing the bands related with the electronic transitions from the t_{2g} to e_g energy levels of Ti^{3+} and $e^-(O^{2-}(2p)) \rightarrow Ti^{IV}$ CT. Moreover, all X-Hec show a short persistent luminescence of ca. 5 s indicating the existence of electron traps which can store excitation energy for a short time. The TL glow curves indicate that these traps are very shallow at RT for all X-Hec materials, which explains their respective short persistent luminescence [I-IV]. However, the luminescence properties of the X-Hec materials may present changes if measured at moderate to high temperatures (from 300 to 600 °C): it is expected that the loss of the hydrated water would improve the luminescence efficiency of the X-Hec materials by eliminating (totally) the multiphonon de-excitation effect of the OH^- ions. Due to time limitation, such investigation was not realized in the current work, but it is a perspective for follow-up research with the X-Hec materials.

The X-Hec materials also demonstrated a high potential to act as host lattice for RE^{3+} ions, without the addition of organic molecules as “antennas” in their structure. The F-Hec and Cl-Hec materials doped with Eu^{3+} and/or Tb^{3+} show the respective emission and excitation bands of these RE^{3+} ions. However, when the materials were co-doped with Eu^{3+} and Tb^{3+}, the Eu^{3+} emission was predominant in the F-Hec materials, whereas Tb^{3+} dominated the emission in the Cl-Hec materials [I-IV].

Several future applications can be proposed based on the versatility of the X-Hec materials presented in this thesis. One promising application is the usage of X-Hec materials for producing supercapacitor materials by obtaining nanocomposites of X-Hec and graphene, since preliminary studies have demonstrated a moderate supercapacitor behavior for the X-Hec materials. Another possible easy application of the X-Hec materials is as a heterogeneous catalyst in polymeric reactions: the easy modification of the X-Hec structure together with their nanosize are promising features to generate a functionalized modifier of the polymer structure, thus enhancing the physical properties of the final product. Also, the production of p-n type of solar cells having the X-Hec materials as the n-type element can be studied, because of the X-Hec materials' abundance in negative free-carriers in their negative layers. Regarding to the Eu^{3+} and/or Tb^{3+}-doped X-Hec materials, they could be used in quantitative determination of bio-molecules, and bio-imaging *in vitro*, due to the high bio-compatibility of clay minerals. Moreover, up-convertor materials may be obtained through the co-doping of X-Hec materials with RE^{3+} ions, e.g., $Er^{3+}/Tm^{3+}/Yb^{3+}$, Yb^{3+}/Tm^{3+}, Tm^{3+}/Er^{3+} etc. Such up-converting materials could be used as light-converting elements, enhancing the efficiency of commercially available solar cell devices.

6. References

[1] E.N. Harvey, A History of Luminescence From the Earliest Times Until 1900, 1st ed., The American Philosophical Society, Baltimore, USA, 1957.

[2] A. Kitai, Luminescent Materials and Applications, 1st ed., John Wiley & Sons Ltd., Chichester, United Kingdom, 2008.

[3] R.C. Ropp, Luminescence and the Solid State, 2nd ed., Elsevier B.V., Amsterdam, NL, 2004.

[4] M. Gaft, R. Reisfeld, G. Panczer, Modern Luminescence Spectroscopy of Minerals and Materials, 1st ed., Springer-Verlag, Berlin/Heidelberg, Germany, 2005.

[5] B.C. Blasse, G., Grabmaier, Luminescent Materials, 1st ed., Springer-Verlag, Berlin, 1994.

[6] S.-J. Ryu, A. Kim, M.D. Kim, S.W. Hong, S.S. Min, J.-H. Lee, J.-K. Lee, H. Jung, Photoluminescent europium(III) complex intercalated in natural and synthetic clay minerals for enhanced latent fingerprint detection, Appl. Clay Sci. 101 (2014) 52–59.

[7] L. Valdés, D. Hernández, L.C. de Ménorval, I. Pérez, E. Altshuler, J.O. Fossum, A. Rivera, Incorporation of tramadol drug into Li-fluorohectorite clay: A preliminary study of a medical nanofluid, Eur. Phys. J. Spec. Top. 225 (2016) 767–771.

[8] J. Tronto, S.J.L. Ribeiro, J.B. Valim, R.R. Gonçalves, Visible and near-infrared luminescent Eu^{3+} or Er^{3+} doped laponite-derived xerogels and thick films: Structural and spectroscopic properties, Mater. Chem. Phys. 113 (2009) 71–77.

[9] J.T. Kloprogge, S. Komarneni, J.E. Amonette, Synthesis of smectite clay minerals: A critical review, Clays Clay Miner. 47 (1999) 529–554.

[10] M. Fox, Optical Properties of Solids, 1st ed., Oxford University Press, Oxford, UK, 2001.

[11] L.C.V. Rodrigues, Preparation and development of the persistent luminescence mechanism of rare earth doped materials, Graduate Program in Chemistry, Instituto de Química, Universidade de São Paulo, São Paulo-SP, Brazil, 2012.

[12] L. Vegard, Die Konstitution der Mischkristalle und die Raumfüllung der Atome, Zeitschrift Für Phys. 5 (1921) 17–26.

[13] K.N. Shinde, S.J. Dhoble, H.C. Swart, K. Park, Phosphate phosphors for solid-state lighting, 1st ed., Springer-Verlag , Berlin / Heidelberg, DE, 2012.

[14] O. Soumonni, An investigation into the luminescence and structural properties of alkali earth metaniobates, Materials Science and Engineering, Georgia Institute of Technology, Atlanta-GA, USA, 2004.

[15] C.R. Ronda, Luminescence from Theory to Applications, 1st ed., Wiley-VCH Verlag, Aachen, Germany, 2008.

[16] S. Shionoya, W.M. Yen, H. Yamamoto, Phosphor Handbook, 2nd ed., CRC Press, Boca Raton-USA, 2007.

[17] P.F. Moulton, Spectroscopic and laser characteristics of Ti:Al_2O_3, J. Opt. Soc. Am. B. 3 (1986) 125–133.

[18] S. García-Revilla, F. Rodríguez, R.

Valiente, M. Pollnau, Optical spectroscopy of Al_2O_3:Ti^{3+} single crystal under hydrostatic pressure. The influence on the Jahn-Teller coupling, J. Phys. Condens. Matter. 14 (2002) 447–459.

[19] G. Blasse, G.J. Dirksen, I. Tanaka, H. Kojima, The luminescence of titanite ($CaTiSiO_5$), Mater. Res. Bull. 23 (1988) 1727–1730.

[20] M. Gaft, L. Nagli, G. Waychunas, D. Weiss, The nature of blue luminescence from natural benitoite $BaTiSi_3O_9$, Phys. Chem. Miner. 31 (2004) 365–373.

[21] M. Maqbool, K. Main, I. Ahmad, Structural Analysis and Infrared Emission from Ti^{+3} Doped AlN Deposited on Si(100) and Si(111) Substrates and Optical Fibers, J. Low Temp. Phys. 179 (2015) 365–374.

[22] V. Kumar, O.M. Ntwaeaborwa, J. Holsa, D.E. Motaung, H.C. Swart, The role of oxygen and titanium related defects on the emission of TiO_2:Tb^{3+} nano-phosphor for blue lighting applications, Opt. Mater. (Amst). 46 (2015) 510–516.

[23] L. V. Maneeshya, V.S. Anitha, P. V. Thomas, K. Joy, Thickness dependence of structural, optical and luminescence properties of $BaTiO_3$ thin films prepared by RF magnetron sputtering, J. Mater. Sci. Mater. Electron. 26 (2015) 2947–2954.

[24] M. Kumar, A. Uniyal, A.P.S. Chauhan, S.P. Singh, Optical absorption and fluorescent behaviour of titanium ions in silicate glasses, Bull. Mater. Sci. 26 (2003) 335–341.

[25] M.-T. Tsai, Y.-S. Chang, Y.-H. Chou, K.-M. Tsai, Photoluminescence of titanium-doped zinc spinel blue-emitting nanophosphors, J. Solid State Chem. 214 (2014) 86–90.

[26] K. Moringa, H. Yoshida, H. Takebe, Compositional Dependence of Absorption Spectra of Ti^{3+} in Silicate, Borate, and Phosphate Glasses, J. Am. Ceram. Soc. 77 (1994) 3113–3118.

[27] J.M. Carvalho, L.C. V. Rodrigues, J. Hölsä, M. Lastusaari, L.A.O. Nunes, M.C.F.C. Felinto, O.L. Malta, H.F. Brito, Influence of titanium and lutetium on the persistent luminescence of ZrO_2, Opt. Mater. Express. 2 (2012) 331–340.

[28] L.H.C. Andrade, S.M. Lima, A. Novatski, P.T. Udo, N.G.C. Astrath, A.N. Medina, A.C. Bento, M.L. Baesso, Y. Guyot, G. Boulon, Long Fluorescence Lifetime of Ti^{3+}-Doped Low Silica Calcium Aluminosilicate Glass, Phys. Rev. Lett. 100 (2008) 027402–027404.

[29] L.H.C. Andrade, S.M. Lima, A. Novatski, A.M. Neto, A.C. Bento, M.L. Baesso, F.C.G. Gandra, Y. Guyot, G. Boulon, Spectroscopic assignments of Ti^{3+} and Ti^{4+} in titanium-doped OH^- free low-silica calcium aluminosilicate glass and role of structural defects on the observed long lifetime and high fluorescence of Ti^{3+} ions, Phys. Rev. B. 78 (2008) 224202–224211.

[30] I. Norrbo, P. Gluchowski, I. Hyppänen, T. Laihinen, P. Laukkanen, J. Mäkelä, F. Mamedov, H.S. Santos, J. Sinkkonen, M. Tuomisto, A. Viinikanoja, M. Lastusaari, Mechanisms of Tenebrescence and Persistent Luminescence in Synthetic Hackmanite

$Na_8Al_6Si_6O_{24}(Cl,S)_2$, ACS Appl. Mater. Interfaces. 8 (2016) 11592-11602.

[31] I. Norrbo, J.M. Carvalho, P. Laukkanen, J. Mäkelä, F. Mamedov, M. Peurla, H. Helminen, S. Pihlasalo, H. Härmä, J. Sinkkonen, M. Lastusaari, Lanthanide and Heavy Metal Free Long White Persistent Luminescence from Ti Doped Li-Hackmanite: A Versatile, Low-Cost Material, Adv. Funct. Mater. 27 (2017) 1606547.

[32] S. Nakayama, M. Sakamoto, Fluorescence property of ZrO_2:Ti phosphor and its enhancement in fluorescent intensity by adding phosphorus, J. Mater. Res. Technol. 5 (2016) 289–292.

[33] Y. Cong, B. Li, B. Lei, W. Li, Long lasting phosphorescent properties of Ti doped ZrO_2, J. Lumin. 126 (2007) 822–826.

[34] G.M. Phatak, K. Gangadharan, H. Pal, J.P. Mittal, Luminescence properties of Ti-doped gem-grade zirconia powders, Bull. Mater. Sci. 17 (1994) 163–169.

[35] L.-H. Lee, Hard-Soft Acid-Base (HSAB) Principle for Solid Adhesion and Surface Interactions, in: L.-H. Lee (Ed.), Fundam. Adhes., 1st ed., Springer US, New York, USA, 1991: pp. 349–362.

[36] P.C. de Sousa Filho, J.F. Lima, O.A. Serra, From Lighting to Photoprotection: Fundamentals and Applications of Rare Earth Materials, J. Braz. Chem. Soc. 26 (2015) 2471–2495.

[37] P.A. Tanner, Some misconceptions concerning the electronic spectra of tri-positive europium and cerium, Chem. Soc. Rev. 42 (2013) 5090.

[38] S.S. Syamchand, G. Sony, Europium enabled luminescent nanoparticles for biomedical applications, J. Lumin. 165 (2015) 190–215.

[39] S.J. Butler, M. Delbianco, L. Lamarque, B.K. McMahon, E.R. Neil, R. Pal, D. Parker, J.W. Walton, J.M. Zwier, EuroTracker® dyes: design, synthesis, structure and photophysical properties of very bright europium complexes and their use in bioassays and cellular optical imaging, Dalt. Trans. 44 (2015) 4791–4803.

[40] Y. Liu, S. Zhou, Z. Zhuo, R. Li, Z. Chen, M. Hong, X. Chen, In vitro upconverting/ downshifting luminescent detection of tumor markers based on Eu^{3+}-activated core–shell–shell lanthanide nanoprobes, Chem. Sci. 7 (2016) 5013–5019.

[41] Y. Xie, W. He, F. Li, T.S.H. Perera, L. Gan, Y. Han, X. Wang, S. Li, H. Dai, Luminescence Enhanced Eu^{3+}/Gd^{3+} Co-Doped Hydroxyapatite Nanocrystals as Imaging Agents In Vitro and In Vivo, ACS Appl. Mater. Interfaces. 8 (2016) 10212–10219.

[42] S.K. Hussain, J.S. Yu, Sol-gel synthesis of Eu^{3+}/Bi^{3+} ions co-doped $BaLa_2WO_7$ phosphors for red-LEDs under NUV excitation and FEDs applications, J. Lumin. 183 (2017) 39–47.

[43] J. Li, Z. Wu, X. Sun, X. Zhang, R. Dai, J. Zuo, Z. Zhao, Controlled hydrothermal synthesis and luminescent properties of $Y2WO_6:Eu^{3+}$ nanophosphors for light-emitting diodes, J. Mater. Sci. 52 (2017) 3110–3123.

[44] C.M. da Silva Jr., L.A. Bueno, A.S. Gouveia-Neto, Er^{3+}/Sm^{3+}- and

Tb^{3+}/Sm^{3+}-doped glass phosphors for application in warm white light-emitting diode, J. Non. Cryst. Solids. 410 (2015) 151–154.

[45] X. Ge, L. Sun, S. Dang, J. Liu, Y. Xu, Z. Wei, L. Shi, H. Zhang, Mesoporous upconversion nanoparticles modified with a Tb(III) complex to display both green upconversion and downconversion luminescence for in vitro bioimaging and sensing of temperature, Microchim. Acta. 182 (2015) 1653–1660.

[46] Q. Bai, Z. Wang, P. Li, S. Xu, T. Li, Z. Yang, Tunable blue-green emitting and energy transfer of a Eu^{2+}/Tb^{3+} codoped $Sr_3La(PO_4)_3$ phosphor for near-UV white LEDs, New J. Chem. 39 (2015) 8933–8939.

[47] A.N. Trukhin, Luminescence of localized states in silicon dioxide glass. A short review, J. Non. Cryst. Solids. 357 (2011) 1931–1940.

[48] Y. Nagayoshi, T. Uchino, Enhanced ultraviolet emission and its irreversible temperature antiquenching behavior of twofold coordinated silicon centers in silica glass, Appl. Phys. Lett. 109 (2016) 181103.

[49] L.N. Skuja, A.R. Silin, A.G. Boganov, On the nature of the 1.9 eV luminescence centers in amorphous SiO_2, J. Non. Cryst. Solids. 63 (1984) 431–436.

[50] A.N. Trukhin, M. Goldberg, J. Jansons, H.-J. Fitting, I.A. Tale, Silicon dioxide thin film luminescence in comparison with bulk silica, J. Non. Cryst. Solids. 223 (1998) 114–122.

[51] L.N. Skuja, A.N. Streletsky, A.B. Pakovich, A new intrinsic defect in amorphous SiO_2: Twofold coordinated silicon, Solid State Commun. 50 (1984) 1069–1072.

[52] A.N. Trukhin, L.N. Skuja, A.G. Boganov, V.S. Rudenko, The correlation of the 7.6 eV optical absorption band in pure fused silicon dioxide with twofold-coordinated silicon, J. Non. Cryst. Solids. 149 (1992) 96–101.

[53] D.L. Griscom, Trapped-electron centers in pure and doped glassy silica: A review and synthesis, J. Non. Cryst. Solids. 357 (2011) 1945–1962.

[54] Y. Zhang, L. Fu, H. Yang, Insights into the physicochemical aspects from natural halloysite to silica nanotubes, Colloids Surfaces A Physicochem. Eng. Asp. 414 (2012) 115–119.

[55] K.A. Carrado, Handbook of Layered Materials, 1st ed., Marcel Dekker, N.Y.-USA, 2004.

[56] A.. Silin, L.. Skuja, A.. Trukhin, Intrinsic defects generation mechanisms in fused silica, J. Non. Cryst. Solids. 38–39 (1980) 195–200.

[57] A. Trukhin, K. Smits, G. Chikvaidze, T. Dyuzheva, L. Lityagina, Luminescence of Silicon Dioxide — Silica Glass, α-Quartz and Stishovite, Open Phys. 9 (2011) 1106–1113.

[58] L. Skuja, Optically active oxygen-deficiency-related centers in amorphous silicon dioxide, J. Non. Cryst. Solids. 239 (1998) 16–48.

[59] F. Bergaya, B.K.G. Theng, G. Legaly, Handbook of Clay Sciences, 1st ed., Elsevier Ltd., Amsterdam/London, 2006.

[60] D. Zhang, C.-H. Zhou, C.-X. Lin,

D.-S. Tong, W.-H. Yu, Synthesis of clay minerals, Appl. Clay Sci. 50 (2010) 1–11.

[61] A. Jordán, Lightening the clay (II), (2014). http://blogs.egu.eu/divisions/sss/2014/09/07/lightening-the-clay-ii/ (accessed August 19, 2017).

[62] L. Bailey, H.N.W. Lekkerkerker, G.C. Maitland, Smectite clay – inorganic nanoparticle mixed suspensions: phase behaviour and rheology, Soft Matter. 11 (2015) 222–236.

[63] J.W. Anthony, R.A. Bideaux, K.W. Bladh, M.C. Nichols, Handbook of Mineralogy, Vol. II, Mineralogical Society of America, Chantilly, VA, USA, 1995.

[64] H. Kalo, W. Milius, J. Breu, Single crystal structure refinement of one- and two-layer hydrates of sodium fluorohectorite, RSC Adv. 2 (2012) 8452–8459.

[65] H. Strese, U. Hofmann, Synthese von Magnesiumsilikat-Gelen mit zweidimensional regelmäßiger struktur, Zeitschrift Für Anorg. Und Allg. Chemie. 247 (1941) 65–95.

[66] I. Vicente, P. Salagre, Y. Cesteros, Preparation of pure hectorite using microwaves, Phys. Procedia. 8 (2010) 88–93.

[67] K.A. Carrado, Preparation of hectorite clays utilizing organic and organometallic complexes during hydrothermal crystallization, Ind. Eng. Chem. Res. 31 (1992) 1654–1659.

[68] B. Ruzicka, E. Zaccarelli, A fresh look at the Laponite phase diagram, Soft Matter. 7 (2011) 1268–1286.

[69] D. Bonn, H. Kellay, H. Tanaka, G. Wegdam, J. Meunier, Laponite: What Is the Difference between a Gel and a Glass?, Langmuir. 15 (1999) 7534–7536.

[70] L. Michels, J.O. Fossum, Z. Rozynek, H. Hemmen, K. Rustenberg, P.A. Sobas, G.N. Kalantzopoulos, K.D. Knudsen, M. Janek, T.S. Plivelic, G.J. da Silva, Intercalation and Retention of Carbon Dioxide in a Smectite Clay promoted by Interlayer Cations, Sci. Rep. 5 (2015) 8775.

[71] B. V. Lotsch, G.A. Ozin, All-Clay Photonic Crystals, J. Am. Chem. Soc. 130 (2008) 15252–15253.

[72] D. Bonn, S. Tanase, B. Abou, H. Tanaka, J. Meunier, Laponite: Aging and Shear Rejuvenation of a Colloidal Glass, Phys. Rev. Lett. 89 (2002) 15701.

[73] Y. Rodríguez-Lazcano, V. Correcher, J. Garcia-Guinea, Thermo- and cathodoluminescence properties of lepidolite, Spectrochim. Acta Part A Mol. Biomol. Spectrosc. 113 (2013) 281–285.

[74] V. Correcher, J. Garcia-Guinea, E. Crespo-Feo, Y. Rodriguez-Lazcano, P. Prado-Herrero, Dose–response of thermoluminescence in natural kaolinite, Thermochim. Acta. 503–504 (2010) 12–15.

[75] J. Garcia Guinea, V. Correcher, F.J. Valle-Fuentes, Thermoluminescence of Kaolinite, Radiat. Prot. Dosimetry. 84 (1999) 507–510.

[76] J. Garcia-Guinea, V. Correcher, Y. Rodriguez-Lazcano, E. Crespo-Feo, P. Prado-Herrero, Light emission bands in the radioluminescence and thermoluminescence spectra of kaolinite, Appl. Clay Sci. 49 (2010)

306–310.

[77] R.K. Hessley, Luminescence in coal and its relation to clay minerals, Clay Miner. 24 (1989) 107–113.

[78] L.M. Coyne, G. Pollack, R. Kloepping, Room-temperature luminescence from kaolin induced by organic amines, Clays Clay Miner. 32 (1984) 58–66.

[79] N. Lahav, L. Coyne, J.G. Lawless, Characterization of dehydration-induced luminescence of kaolinite, Clays Clay Miner. 33 (1985) 207–213.

[80] J. Götze, M. Plötze, T. Götte, R.D. Neuser, D.K. Richter, Cathodoluminescence (CL) and electron paramagnetic resonance (EPR) studies of clay minerals, Mineral. Petrol. 76 (2002) 195–212.

[81] N.A. Kotov, T. Haraszti, L. Turi, G. Zavala, R.E. Geer, I. Dékány, J.H. Fendler, Mechanism of and Defect Formation in the Self-Assembly of Polymeric Polycation−Montmorillonite Ultrathin Films, J. Am. Chem. Soc. 119 (1997) 6821–6832.

[82] K. Somaiah, M. Venkatanarayana, B. Sathyanarayana, Thermally Stimulated Luminescence of Montmorillonite Clay, Cryst. Res. Technol. 26 (1991) 357–362.

[83] V. Correcher, J.M. Gómez-Ros, J. Garcia-Guinea, P.L. Martin, A. Delgado, Thermal stability of the thermoluminescence trap structure of bentonite, Radiat. Prot. Dosimetry. 119 (2006) 176–179.

[84] T. V. Bezrodna, G. V. Klishevich, V.I. Melnyk, V. V. Nesprava, G.A. Puchkovska, I.T. Chashechnikova, Photoluminescence of montmorillonite clay minerals modified by cetyltrimethylammonium bromide, J. Appl. Spectrosc. 77 (2011) 784–789.

[85] D. Yang, J. Wang, H. Li, Photo- and thermo-stable luminescent nanocomposite resulting from hybridization of Eu(III)-β-diketonate complexes with laponite, Dye. Pigment. 118 (2015) 53–57.

[86] H. Li, M. Li, Y. Wang, W. Zhang, Luminescent Hybrid Materials Based on Laponite Clay, Chem. - A Eur. J. 20 (2014) 10392–10396.

[87] A.F. da Silva, D.S. Moura, A.S. Gouveia-Neto, E.A. Silva Jr., L.A. Bueno, E.B. Costa, E.N. Azevedo, Intense red upconversion fluorescence emission in NIR-excited erbium–ytterbium doped laponite-derived phosphor, Opt. Commun. 284 (2011) 4501–4503.

[88] P. Scherrer, Bestimmung der Grösse und der inneren Struktur von Kolloidteilchen mittels Röntgensrahlen, Math. Klasse. 1918 (1918) 98–100.

[89] S. Brunauer, P.H. Emmett, E. Teller, Adsorption of gases in multimolecular layers, J. Am. Chem. Soc. 60 (1938) 309–319.

[90] J. Rouquerol, D. Avnir, C.W. Fairbridge, D.H. Everett, J.M. Haynes, N. Pernicone, J.D.F. Ramsay, K.S.W. Sing, K.K. Unger, Recommendations for the characterization of porous solids (Technical Report), Pure Appl. Chem. 66 (1994) 1739–1758.

[91] R. Chen, V. Pagonis, Thermally and Optically Stimulated Luminescence: a Simulation Approach, 1st ed., John Wiley & Sons, Chichester, UK, 2011.

[92] W.F. Jaynes, S.J. Traina, J.M. Bigham, C.T. Johnston, Preparation

and Characterization of Reduced-Charge Hectorites, Clays Clay Miner. 40 (1992) 397–404.

[93] V.C. Farmer, Differing effects of particle size and shape in the infrared and Raman spectra of kaolinite, Clay Miner. 33 (1998) 601–604.

[94] J. Moon, M.M. Reda Taha, K.S. Youm, J.J. Kim, Investigation of pozzolanic reaction in nanosilica-cement blended pastes based on solid-state kinetic models and ^{29}SI MAS NMR, Materials (Basel). 9 (2016) 99.

[95] A. Peyvandi, I. Harsini, D. Holmes, A.M. Balachandra, P. Soroushian, Characterization of ASR in concrete by ^{29}Si MAS NMR spectroscopy, J. Mater. Civ. Eng. 28 (2016) 4015096.

[96] H. Pálková, J. Madejová, M. Zimowska, E. Bielańska, Z. Olejniczak, L. Lityńska-Dobrzyńska, E.M. Serwicka, Laponite-derived porous clay heterostructures: I. Synthesis and physicochemical characterization, Microporous Mesoporous Mater. 127 (2010) 228–236.

[97] B. Thien, N. Godon, F. Hubert, F. Angéli, S. Gin, A. Ayral, Structural identification of a trioctahedral smectite formed by the aqueous alteration of a nuclear glass, Appl. Clay Sci. 49 (2010) 135–141.

[98] K.A. Carrado, L. Xu, D.M. Gregory, K. Song, S. Seifert, R.E. Botto, Crystallization of a Layered Silicate Clay as Monitored by Small-Angle X-ray Scattering and NMR, Chem. Mater. 12 (2000) 3052–3059.

[99] Y. Wang, P. Zhang, K. Wen, X. Su, J. Zhu, H. He, A new insight into the compositional and structural control of porous clay heterostructures from the perspective of NMR and TEM, Microporous Mesoporous Mater. 224 (2016) 285–293.

[100] K.A. Carrado, R. Csencsits, P. Thiyagarajan, S. Seifert, S.M. Macha, J.S. Harwood, Crystallization and textural porosity of synthetic clay minerals, J. Mater. Chem. 12 (2002) 3228–3237.

[101] K.J.D. Mackenzie, M.E. Smith, Multinuclear Solid-State NMR of Inorganic Materials, 1st ed., Elsevier Science, Oxford, 2002.

[102] A.C. Thompson, J. Kirz, D.T. Attwood, E.M. Gullikson, M.R. Howells, J.B. Kortright, Y. Liu, J.H. Robinson, A.L. Underwood, J.H., Kim, K.-J., Lindau, I., Pianetta, P., Winick, H., Williams, G.P., Scofield, X-Ray Data Booklet, 3rd ed., Lawrence Berkeley National Laboratory, Berkeley-USA, 2009.

[103] Z.A. Alothman, A Review: Fundamental Aspects of Silicate Mesoporous Materials, Materials (Basel). 5 (2012) 2874–2902.

[104] T. Sánchez, P. Salagre, Y. Cesteros, Ultrasounds and microwave-assisted synthesis of mesoporous hectorites, Microporous Mesoporous Mater. 171 (2013) 24–34.

[105] D. Varade, K. Haraguchi, Novel bimetallic core–shell nanocrystal–clay composites with superior catalytic activities, Chem. Commun. 50 (2014) 3014–3017.

[106] M. Ziadeh, B. Chwalka, H. Kalo, M.R. Schütz, J. Breu, A simple approach for producing high aspect ratio fluorohectorite nanoplatelets utilizing a stirred media mill (ball

mill), Clay Miner. 47 (2012) 341–353.

[107] A.U. Dogan, M. Dogan, M. Omal, Y. Sarikaya, A. Aburub, D.E. Wurster, Baseline studies of The Clay Minerals Society source clays: Specific surface area by Brunauer Emmett Teller (BET) method, Clays Clay Miner. 54 (2006) 62–66.

[108] M. Dogan, A. Umran Dogan, F. Irem Yesilyurt, D. Alaygut, I. Buckner, D.E. Wurster, Baseline studies of the Clay Minerals Society Special Clays: Specific surface area by the Brunauer Emmett Teller (BET) method, Clays Clay Miner. 55 (2007) 534–541.

[109] F. Bergaya, The meaning of surface area and porosity measurements of clays and pillared clays, J. Porous Mater. 2 (1995) 91–96.

[110] R.K. Pujala, N. Pawar, H.B. Bohidar, Universal Sol State Behavior and Gelation Kinetics in Mixed Clay Dispersions, Langmuir. 27 (2011) 5193–5203.

[111] M. Al-Mukhtar, Y. Qi, J.F. Alcover, J. Conard, F. Bergaya, Hydromechanical effects: (II) on the water-Na-smectite system, Clay Miner. 35 (2000) 537–544.

[112] L.-B. Xiong, J.-L. Li, B. Yang, Y. Yu, Ti^{3+} in the Surface of Titanium Dioxide: Generation, Properties and Photocatalytic Application, J. Nanomater. 2012 (2012) 1–13.

[113] D.E. Harrison, N.T. Melamed, E.C. Subbarao, A New Family of Self-Activated Phosphors, J. Electrochem. Soc. 110 (1963) 23–28.

[114] N.U. Zhanpeisov, A. Masakazu, Hydrogen Bonding versus Coordination of Adsorbate Molecules on Ti-Silicalites: A Density Functional Theory Study, J. Am. Chem. Soc. 126 (2004) 9439–9444. doi:10.1021/JA0385484.

[115] W.J. James, J.W. Johnson, Standard Potentials in aqueous solution, Marcel Dekker, N.Y.-USA, 1985.

[116] D.F. Shriver, P.W. Atkins, Inorganic Chemistry, 3rd ed., Oxford University Press, Oxford, UK, 1999.

[117] A. Yangui, S. Pillet, A. Lusson, E.-E. Bendeif, S. Triki, Y. Abid, K. Boukheddaden, Control of the white-light emission in the mixed two-dimensional hybrid perovskites $(C_6H_{11}NH_3)_2[PbBr_{4-x}I_x]$, J. Alloys Compd. 699 (2017) 1122–1133.

[118] E.G. Rogers, P. Dorenbos, Vacuum energy referred $Ti^{3+/4+}$ donor/acceptor states in insulating and semiconducting inorganic compounds, J. Lumin. 153 (2014) 40–45.

[119] W. Horwath, Y.L. Liang, Variations of Chemical Composition and Band Gap Energies in Hectorite and Montmorillonite Clay Minerals on Sub-Micron Length Scales, Final Report: 2009008, Kearney Foundation of Soil Science, Davis - CA, USA, 2011.

[120] K. Van den Eeckhout, A.J.J. Bos, D. Poelman, P.F. Smet, Revealing trap depth distributions in persistent phosphors, Phys. Rev. B. 87 (2013) 45126.

[121] J.M. Carvalho, L.C. V. Rodrigues, M.C.F.C. Felinto, L.A.O. Nunes, J. Hölsä, H.F. Brito, Structure–property relationship of luminescent zirconia nanomaterials obtained by sol–gel method, J. Mater. Sci. 50 (2015) 873–881.

[122] T. Felbeck, A. Bonk, G. Kaup, S. Mundinger, T. Grethe, M. Rabe, U.

Vogt, U. Kynast, Porous nanoclay polysulfone composites: A backbone with high pore accessibility for functional modifications, Microporous Mesoporous Mater. 234 (2016) 107–112.

[123] M. Janek, D. Zich, M. Naftaly, Terahertz time-domain spectroscopy response of amines and amino acids intercalated smectites in far-infrared region, Mater. Chem. Phys. 145 (2014) 278–287.

[124] J. Hölsä, P. Porcher, Free ion and crystal field parameters for REOCl:Eu^{3+}, J. Chem. Phys. 75 (1981) 2108.

[125] P. Manasa, C.K. Jayasankar, Luminescence and phonon side band analysis of Eu^{3+}-doped lead fluorosilicate glasses, Opt. Mater. (Amst). 62 (2016) 139–145.

[126] M.R. Cicconi, A. Veber, D. de Ligny, J. Rocherullé, R. Lebullenger, F. Tessier, Chemical tunability of europium emission in phosphate glasses, J. Lumin. 183 (2017) 53–61.

[127] H. Bettentrup, J. Hölsä, T. Laamanen, M. Lastusaari, M. Malkamäki, J. Niittykoski, E. Zych, Effect of Mg^{2+} and Ti^{IV} doping on the luminescence of Y_2O_3:Eu^{3+}, J. Lumin. 129 (2009) 1661–1663.

[128] L.C. V. Rodrigues, H.F. Brito, J. Hölsä, M. Lastusaari, Persistent luminescence behavior of materials doped with Eu^{2+} and Tb^{3+}, Opt. Mater. Express. 2 (2012) 382–390.

[129] V.S. Gorelik, S.N. Ivicheva, L.S. Lepnev, A.O. Litvinova, Tb^{3+} photoluminescence in mesoporous glasses, terbium nitrate and terbium chloride hexahydrates, and coordination compounds, Inorg. Mater. 52 (2016) 828–835.

[130] W. Lü, M. Jiao, J. Huo, B. Shao, L. Zhao, Y. Feng, H. You, Crystal structures, tunable emission and energy transfer of a novel $GdAl_{12}O_{18}N$:$Eu^{2+}Tb^{3+}$ oxynitride phosphor, New J. Chem. 40 (2016) 2637–2643.

[131] U. Caldiño, A. Speghini, S. Berneschi, M. Bettinelli, M. Brenci, E. Pasquini, S. Pelli, G.C. Righini, Optical spectroscopy and optical waveguide fabrication in Eu^{3+} and Eu^{3+}/Tb^{3+} doped zinc–sodium–aluminosilicate glasses, J. Lumin. 147 (2014) 336–340.

[132] M. Bettinelli, C.D. Flint, Non-resonant energy transfer between Tb^{3+} and Eu^{3+} in the cubic hexachloroelpasolite crystals $Cs_2NaTb_{1-x}Eu_xCl_6$ (x=0.01-0.15), J. Phys. Condens. Matter. 2 (1990) 8417–8426.

Annales Universitatis Turkuensis

Turun yliopisto
University of Turku

Painosalama Oy, Turku , Finland 2017

ISBN 978-951-29-7069-8 (PRINT)
ISBN 978-951-29-7070-4 (PDF)
ISSN 0082-7002 (PRINT) | ISSN 2343-3175 (PDF)